AFOSR Scientific Report
AFOSR 67-2047

INVESTIGATION OF A TWO-DIMENSIONAL FULLY STALLED TURBULENT FLOW FIELD

By

G. CHUI and S. J. KLINE

Prepared from work done under
U.S. Air Force Office of Scientific Research
Mechanics Division Contract AF 49(638)-1278

Report MD-19

Thermosciences Division
Department of Mechanical Engineering
Stanford University
Stanford, California

August 1967

INVESTIGATION OF A TWO-DIMENSIONAL FULLY STALLED TURBULENT FLOW FIELD

By

G. Chui and S. J. Kline

Prepared from work done under
U. S. Air Force Office of Scientific Research
Mechanics Division Contract AF 49(638)-1278

Report MD-19

Thermosciences Division
Department of Mechanical Engineering
Stanford University
Stanford, California

August 1967

BLANK PAGE

ACKNOWLEDGMENTS

This research under Contract AF 49(638)1278, Project-Task No. 9781-02 was sponsored by the Air Force Office of Scientific Research, Office of Aerospace Research, United States Air Force.

Technical Supervisor for this program is Major Donald L. Calvert, Project Scientist, Mechanics Division, Directorate of Engineering Sciences, Air Force Office of Scientific Research.

Thanks are due to Professors J. P. Johnston and O. H. Schuck for their constructive comments on the presentation of this report.

Assistance from the following persons are appreciated. Mr. R. Birch constructed major parts of the experimental apparatus and suggested ideas for the design. Mr. E. Hirst calculated some boundary layer results used herein. Mr. F. Hussain drew some of the sketches. Mrs. N. Schulz typed the manuscript.

ABSTRACT

The bistable, steady, turbulent separation phenomenon observed in a two-dimensional fully-stalled diffuser is studied. Detailed mean flow data including pressure, dissipation and velocity (both magnitude and direction) inside the flow field as well as development of boundary layers on both side walls are reported for cases with thin and thick boundary layers at inlet and with and without fairing curves at the throat.

For all cases, most important changes in flow data occur in a region within two inlet widths up and downstream of the throat. Pressure gradients in this region are so large that the boundary layer on the unstalled side changes shape abruptly while the layer on the stalled side separates in the viscinity of the throat.

Streamline patterns are obtained from the velocity distributions. The location of the dividing streamline is different for the different cases. Based on the dividing streamline, a displacement line is defined to extend the concept of displacement thickness to the free shear layer which is developed from the separated boundary layer. This displacement line together with the loci of boundary layer displacement thicknesses on the solid walls form an effective channel. The shape and area ratio of this effective channel explain the different trends of pressure distributions in the main flow.

Based on the data obtained, an iterative calculation procedure is suggested for predicting stable flow configurations in two-dimensional straight diffusers. Part of the calculation procedure is solved to check with the experimental data.

TABLE OF CONTENTS

LIST OF FIGURES

LIST OF TABLES

NOMENCLATURE

A	Effective cross-sectional area
A'	Cross-sectional area for inviscid flow
B	Bernoulli number, $1 - \dfrac{P_{T_{\infty 1}} - P_T(X,Y)}{q_1}$
b	Height of diffuser, see fig. I-1
C_f	Friction factor, $\dfrac{\tau_w}{\rho U_\delta^2/2}$
C_p	Local static pressure recovery coefficient, $\dfrac{p - p_1}{q_1}$
C_{pi}	One-dimensional ideal pressure recovery based on cross-sectional areas of effective channel, $C_{pi} = 1 - (A_1/A)^2$
C'_{pi}	One-dimensional ideal pressure recovery based on areas between solid walls and dividing streamline, $C'_{pi} = 1 - (A'_1/A')^2$
H	Boundary layer shape factor, δ^*/θ
K_1	Two-dimensional blockage factor at inlet, $\left(\dfrac{\delta^*_{un} + \delta^*_{st}}{W} \right)_1$
L	Length of divergent wall, fig. I-1
$\dot{M}$	Flow rate
n	Independent variable normal to local streamline in Euler's equation
P	Static pressure
P_T	Total pressure

q	Dynamic flow head, $\rho U^2/2$
q_1	Mean dynamic heat at inlet, $\rho V_1^2/2$
Re	Reynolds number, $\frac{\rho V_1 W}{\mu}$
RC	Radius of curvature
RC8	Name for flow field with radius of curvature at the throat = 8" (See Chapter IV)
REF	Name for the reference flow field defined in Chapter III
r	Local radius of curvature of streamline in Euler's equation
S	Coordinate measured along channel wall, (see fig. I-1). Origin is at the intersection of side wall with Y-axis
S.P.	Separation point
TKD	Name for flow field with thick boundary layers at inlet
U	Total mean velocity
u	Component of U in X direction
u'	Rms value of fluctuations of u
u_τ	Shear velocity, $\sqrt{\tau_w/\rho}$
u^+	Normalized velocity in boundary layer, U/u_τ
V	Continuity velocity, Eq. II-1
v	Component of U in Y direction
VG	Vortex generator
W	Channel width at inlet, see fig. I-1
X	Axial direction measured from the diffuser throat (fig. I-1); usually measured in inches

Y	Distance normal to X direction to form a set of two-dimensional Cartesian coordinates (fig. I-1)
y	Normal distance from the wall in boundary layers; forms a set of two-dimensional coordinates with S (fig. I-1)
y^+	Normalized distance from the wall in boundary layer, yu_τ/ν

Symbols for loci

δ_{un}	Locus of boundary layer thickness on unstalled wall
δ_{st}	Locus of boundary layer thickness on stalled wall
Y_{ff}	Boundary of free shear layer on free stream side, Eq. III-2
Y_{fr}	Boundary of free shear layer on reverse flow side, Eq. III-3
Y_δ^*	Displacement line; locus of δ_f^* defined by Eq. III-8
Ψ_d	Dividing streamline, Eq. III-6
$Y_{u=0}$	Locus of point where u component = 0
δ_{st}^*	Locus of displacement thickness of boundary layers on stalled wall
δ_{un}^*	Locus of displacement thickness of boundary layer on stalled wall

Greek letters

α	Local flow direction with respect to X- axis
δ	Boundary layer thickness where $B = B_\infty - 0.01$. Page 16

δ^* Displacement thickness, $\int_0^\delta (1 - \frac{U}{U_\delta})\, dy$

δ_f^* Displacement thickness in free shear layer (Eq. III-3)

θ Momentum thickness, $\int_0^\delta \frac{U}{U_\delta} (1 - \frac{U}{U_\delta})\, dy$;

or half angle of the test channel.

λ_x Fraction of one grid size next to boundary in X direction. Page 51

λ_y Fraction of one grid size next to boundary in Y direction. Page 51

μ Fluid viscosity

γ Fluid kinematic viscosity, $\frac{\mu}{\rho}$

ρ Fluid density

ξ Dummy integration variable

τ_w Local wall shear

Ψ Stream function

Subscripts

1 Inlet reference point

2 Location defined as needed

e Exit plane

rev Reverse stream

room Test room

st Stalled side

un Unstalled side

w Wall value stalled or unstalled

$\mathbb{C}$	Center line, Y = 0
δ	Edge of boundary layer
δ_{fm}	Edge of free shear layer on main flow side
∞	Free stream of main flow

Chapter I

INTRODUCTION

Separated flow has long been recognized as one of the very important unsolved problems in fluid mechanics. When separation occurs on an air-foil, lift is reduced and drag increases. Flow separation also limits the performances of many other fluid-mechanical devices such as compressors, turbines, jet engines and diffusers and in many cases can cause undesirable unsteadiness. However, because of the complicated flow structure not only is the problem far from solved, but also little data exist in the literature to show what actually happens in a separated flow field. The primary purpose of the present study is therefore to supply careful, detailed data in a separated flow field as a basis for improved understanding and calculation procedures.

A. Geometry

The geometry chosen for the present investigation is that of a wide-angle diffuser (fig. I-1) which falls in the fully-developed two-dimensional stalled zone on the flow-regime chart as given by Fox and Kline [1962] (fig. I-2). A flow of this type can be qualitatively divided into five zones as shown in the sketch on the following page.

All these zones have different characteristics, but reach a steady interaction by balance of pressure, viscous and dynamic forces. It is clear that an analytical solution cannot be obtained without a large number of approximations and assumptions.

This geometry is chosen for two important reasons. First, it is one of the simplest separated-flow fields known. There is no reattachment point to complicate the separation behavior. The flow is very steady and essentially two-dimensional. The

separated region is so large that meaningful mean flow data can be obtained within the separated zone. Second, there is great practical significance in this flow pattern. Fluidic switches and amplifiers operate in a similar geometry. Understanding of the fluid mechanics of such flow fields should aid further development of fluidic devices. Fully-stalled diffusers are always associated with low performance. When detailed flow data are available, performance may be improved by proper design to correct some undesirable characteristics that occur in the flow field.

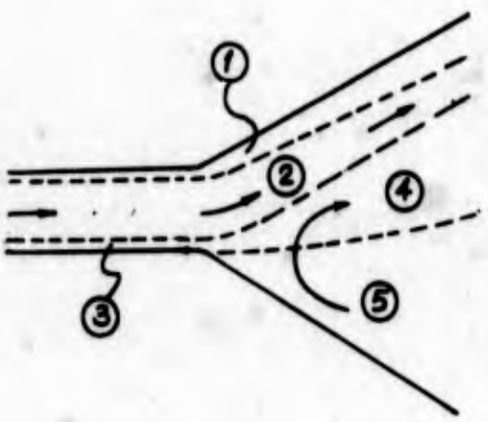

1. Unstalled turbulent boundary layer traversing positive and negative pressure gradients.
2. Potential main stream.
3. Turbulent boundary layer before separation.
4. Free shear layer.
5. Separated-flow region.

B. Literature Review of Fully-Stalled Diffusers

Moore and Kline [1958] first systematically defined the geometries for which fully-stalled flow occurs in a two-dimensional diffuser. Still photos of the flow patterns are given in their report and motion pictures in the films, "Flow Regimes in Subsonic Diffusers," by Kline [1965], and "Flow Vizualization," by Kline [1963].

O. Feil [1962] presented some data on the pressure distributions along the two divergent walls of a fully-stalled diffuser with different angles and different inlet boundary layer thickness. Some of Feil's data which are closely related to the present study are reproduced in fig. I-3.

VanSant and Larson [1965] measured heat transfer and some velocity data far downstream of the separation point in similar geometries, but no pressure measurements were taken in their work. H. Moses, et al [1965] present some data on pressure distributions along the walls of a channel where one side is divergent and the opposite side straight. Neither of these references bear directly on the work presented here, however.

C. The Present Report

The present research is mostly experimental in nature and concentrates on the following.

1. Exploration of the flow field in detail to map out the mean flow data as a means for finding the dominating mechanisms and boundaries of each zone.

2. Determination of the parameters which when varied may cause significant changes from the reference data presented in Chapter IV.

3. Search for matching conditions between the zones in the flow field as a basis for an analytical model which will allow, a priori, a prediction of the equilibrium flow configuration.

Chapter II gives descriptions of the experimental apparatus, instrumentation and data procedures.

Chapter III presents results for the "reference" flow field in which the radius of curvature at the throat is zero and the boundary layer displacement thicknesses at the entrance are thin.

Chapter IV describes some variations from the "reference" flow field obtained by changing radius of curvature, thickening the boundary layers at inlet, adding turbulent mixing devices at the entrance and changing the Reynolds number.

In Chapter V, an analytical model based on facts obtained in previous chapters is proposed. Part of the analytical equations are solved to check the validity of the proposed model.

Chapter VI presents the summary of results and conclusions.

It is to be emphasized that the program described is a basic study. Neither design criteria nor methods of improving device performance are suggested. Hopefully, however, the results obtained will provide a first step toward understanding and explaining separation phenomena in internal passages in a wide range of practical devices involving flowing fluids.

Chapter II

EXPERIMENTAL APPARATUS: INSTRUMENTATION AND DATA PROCEDURES

A. Wind Tunnel

Figure II-1 shows two views of the apparatus designed and constructed for the present experiment. This tunnel shares the same blower and motor drive with the tunnel designed by C. Sagi [1965]. Since most of the tests need about 8100 cfm of clean air, a large filter box (3' x 5') was constructed. An air control gate is placed before the intake to the blower. Air flow speed can be changed by inserting blanking boards with different hole sizes. At the exit of the blower, two gates are built around a T-shaped duct for diverting air into either of the two wind tunnels by relocating a blank-off board.

Before the air passes to the nozzle, the boundary layers on the plenum walls are sucked off through slots. Since the nozzle is only convergent in one direction, thin boundary layers at the exit of the nozzle cannot be obtained without suction. The converging walls of the nozzle have the shape of a cosine curve with a continuous second derivative. An aspect ratio of 8 and width of 3" at the exit of the nozzle are fixed.

Between the nozzle and the test section there are 36 pressure taps, and 20 probe holes at various positions in a rectangular plexiglas section. Traverses of both static and total pressure taken at this section show variations of no more than two percent of the mean dynamic head. Hence, the flow entering the test section can be taken as essentially two-dimensional.

B. Test Section

The geometry of the test section has been specified in fig. I-1. Figure II-2 shows photos from two views. The

side-walls (1) are made of plywood, sanded and varnished to smooth flat surfaces. They rest on a surface board made of laminated sugar-pine (14) fig. II-1. The throat sections of the side-walls are so that curvature can be changed by inserting new fairing pieces, (5) fig. II-2.

On each side wall there are three rows of pressure taps so that pressure distributions along the walls can be measured at three different level planes 6", 10" and 18" from the base respectively (see fig. II-2). The maximum variation in the pressure readings of these three rows is less than 2% of q_1. Thus the flow can be treated as two-dimensional in the section between these levels.

To make a pressure tap, a 1/8" O.D. brass tube about 3" long was soldered shut and then faced on one end. A No. 57 hole was drilled and counter-sunk in the soldered end. Each brass tubing was then press-fitted into an accurately located 1/8" hole in the plywood side wall.

Besides these pressure taps, probe holes are made along the center level on each side wall for insertion of boundary layer probes. The center line of each hole is normal to the test surface. Aluminum plugs are individually fitted to these holes, and the surface lapped after insertion.

The top plate is made of four separate pieces of plexiglas joined by metal bars. The two middle pieces serve as sliders to carry a three-hole probe for flow field traverses. Insertion holes are machined on lines which are perpendicular to the center line of the test section and at fixed distances from the throat. Plexiglas plugs are fitted to these holes individually. These sliders are manually movable along one axis, and are clamped down by specially designed clamps when data are being taken.

To thicken the inlet boundary layer, a six-foot long straight channel was added between the nozzle and the test section. This channel gives ample entrance length for the

boundary layers to grow naturally forming an almost fully-developed channel flow before the test section.

For another test, vortex generators were added 12" up stream of the throat. These vortex generators are made of small air foils glued on thin strips of plexiglas which were then attached on the side walls. The dimensions and arrangement of the vortex generators follow the recommendations of H. D. Taylor [1948] (see section C.1, Chapter IV).

C. Qualitative Observation Methods

Two banks of manometers were used to show qualitatively the pressure distributions along the two walls as well as around the exit of the nozzle. Such pictures serve as a quick check on the flow conditions. Whenever data were being taken for the same flow map, a check was made that pressure distributions were the same as previously obtained.

For each flow map, as a preliminary, tufts were attached on the walls to aid in determining the flow pattern and in locating the separation point. These tufts were made of wool yarn with fine loops of thin threads at one end forming a universal joint as suggested in the note by A. Shapiro [1962]. In addition, a single tuft carried by a rod was inserted through the probe holes in the sliders to establish roughly the boundaries of the different zones in the flow field before detailed measurements were taken. Another independent method was also used to determine the location of the separation point. A coat of machine oil was applied on the stalled side of the test section, and talcum powder was then shaken out of a can in the separated region. Since the air flows upstream in the stalled area, it carries the powder and deposits it on the coat of oil. The powder does not pass the separation point, and hence the line of separation is made visible as the farthest upstream location of powder on the wall.

D. Quantitative Mean Flow Measurement

The flow pattern is bi-stable. Each time the blower is turned on stable stall occurs arbitrarily on one or the other side wall. Switching can be done within half a second by holding a stick at the throat on the unstalled wall. A preliminary check was made to assure that within experimental uncertainty, flow data depend on the flow pattern and not on which side wall the fluid is stalled. However, for consistency and for ease of description, all data were taken with the stall on the right wall. (See fig. I-1.)

Except for the wall pressure distributions, all data were taken on a traverse plane which is equidistant from the top and bottom planes, i.e., 12" from the base board. The coordinate system used for presenting data has been indicated in fig. I-1. Inlet reference is taken to be at $X = -6"$, that is, 2W upstream of the throat on the traverse plane. At this reference position the velocity in the free stream is uniform, and the boundary layer profile and pressure on both side walls are normally the same.

D.1. Pressure Transducers

Two pressure transducers (manufactured by Statham Instruments, Inc.) were used to sense pressure differences. Model No. PM 5, with a range up to 6" H_2O, was for main flow and boundary layer measurements, while Model No. PM 97, a more sensitive unit ($\pm$ 1.4" H_2O), was used for measuring the stalled flow and for nulling flow direction. Output from the transducer circuits was taken from a Millivolt potentiometer (Model 401, United Systems Corp.).

D.2. Inlet Dynamic Head, q_1

At an early stage of experiments velocity traverses were taken across the exit of the nozzle on a few different

level planes by pitot tube. Continuity velocity

$$V \triangleq \frac{1}{W} \int_{-\frac{W}{2}}^{\frac{W}{2}} U \, dY \qquad \text{(II-1)}$$

was calculated for each of these traverses and compared with the one obtained at the inlet reference position on the traverse plane. Their values checked within 2% and hence neglecting the effects of the top and bottom walls, the continuity velocity was thereafter calculated by a two-dimensional model at the inlet reference as follows.

$$V_1 = U_{\infty_1}(1 - K_1) \quad \text{where} \quad K_1 \triangleq \left(\frac{\delta^*_{un} + \delta^*_{st}}{W} \right)_1$$

$$\text{and} \quad q_1 \triangleq \frac{1}{2} \rho V_1^2 = \frac{1}{2} \rho (1 - K_1)^2 U_{\infty_1}^2$$

$$= (1 - K_1)^2 (P_T - P)_{\infty_1}$$

Since the boundary layer thicknesses for each flow map did not change, only a measurement of $(P_T - P)_{\infty_1}$ was needed to obtain q_1 for each run.

D.3. Boundary Layer Profiles

Because of the divergence of the test channel, probes had to be traversed outward from the same surface on which the boundary layer was to be measured. For this purpose, probes were made with 22 gage hypodermic needles bent to a right angle and soldered on 1/8" brass tubings. Tips of these probes were flattened to about .020" outside to allow measurement

close to the wall, and at the same time maintain a fast response time. Noses of the probes are 1/2" long, which is more than 20 times the diameter so that the disturbance at the point of measurement is small.

The static pressure at the wall was used as the static pressure throughout the boundary layer in most cases. Near the throat where there is a large normal pressure gradient, linear extrapolation from the pressure field was used to get local pressure in the boundary layer. Since the extrapolation distance is short, and the linear extension of pressure data in flow field agrees with the wall pressure to less than the estimated uncertainty, the method appears quite valid. (See fig. III-4.) Hence

$$\frac{U}{U_\delta} = \left(\frac{P_T - P_w}{P_{T_\delta} - P_w}\right)^{\frac{1}{2}}$$

No normal pressure gradient

P_w = static pressure at wall

$$\frac{U}{U_\delta} = \left[\frac{P_T - [P_w + (P_\delta - P_w)\, y/\delta]}{P_{T_\delta} - P_\delta}\right]^{\frac{1}{2}}$$

With normal pressure gradient

y = distance from the wall

δ = boundary layer thickness

In addition, since the velocity never approaches a constant outside the boundary in the throat region, U_δ is defined as the velocity of the point where P_T first becomes $(P_T - 1\%\ q_1)$, and this definition is used for all stations. δ is defined as the value of y at the points where $U = U_\delta$.

For the separated profile at $X = +0.5"$ on the stalled side, two traverses were made for each profile, one with the probe inserted at $X = 0"$ and its tip facing the exit while the other from $X = 1"$ with the tip facing upstream. These two traverses were matched at the point of zero velocity.

D.4. Pressure Along Side Walls

Most pressure readings along the two side-walls were taken from the row of pressure taps 10" from the bottom. Around the throat where the pressure changes most rapidly, more taps were needed and some were placed 2" above the traverse plane. Since the flow is two-dimensional, these readings can be assumed to be the values on the traverse plane.

D.5. Flow Field Data

A three hole probe made by United Sensor and Control Corp. (Model YC-1200) was used to measure the flow field data. This probe was calibrated against a Kiel probe and a pitot tube in the test channel at several locations and Reynolds numbers. Correction factors were obtained and stored in the computer program for data reduction. Arrangement of the instruments is shown in fig. II-3. At each data point in the flow field, measurements for coordinates, static pressure, direction and magnitude of velocity were needed.

As each probe hole on the sliders was machined on a traverse line of fixed distance from the throat, the X-coordinate was determined by the hole in which the probe was placed. The normal procedure was to place the probe at a desired Y- coordinate on the traverse line and move the slider until the brass contact rod touched the vernier caliper which had been pre-set at a reading that indicated the desired relative distance of the probe from the center line. Electric wires were connected to the vernier caliper and the contact rod so that a small electric light would glow when they came into contact. A special precaution was taken when the probe was moved close to the wall. To be sure that the probe did not alter the boundary layer and thus disturb the flow pattern, data taking for that particular traverse was terminated as soon as disturbance was observed in the manometer readings of the pressure along the walls.

After sliding the probe to a desired position, the slider was clamped down. Then the probe was rotated about its axis by turning the protractor until the two side holes sensed equal pressure as shown by zero reading on the galvanometer which was connected to the output of the transducer PM97. Pressure sensed by the center hole was the total pressure of the fluid and one of the side holes yielded the static pressure through the calibration correction. Direction of flow was obtained from the setting of the protractor relative to a mark on the vernier scale fixed at the outside casing. This mark had been aligned on the traverse line by dowel pins on the probe holder and dowel holes on the slider.

In the shear layers, the pressures sensed by the transducers fluctuate about a mean value. Direction was read when the fluctuation of the needle in the galvanometer showed equal amplitude on each side of the null point. Correction to the direction owing to velocity gradient was made as described in Appendix A. For the total pressure and static pressure measurements, the uncertainty interval of each reading was taken as one third of the total fluctuation amplitude about the mean. Propagation of uncertainty into the final data at each point was carried out in the computer program for data reduction.

Several traverses were repeated at the beginning of the experiment; duplication of data was well within estimated uncertainties. Estimates of uncertainty are presented in Chapter III together with the data for the reference flow field.

Difficulties in determining the flow direction also arose near the line where the reverse flow turns around sharply. In this zone, the magnitude of the velocity fluctuations can be as high as the mean value, and thus pressure sensed by the two side holes can be obtained with two opposite orientations of the probe at one location. The flow angle was then taken to be the one that showed higher mean total pressure as sensed by the center hole.

D.6. Hot Wire Measurement

A Thermo-system 1040A Hot Wire Anemometer was used to estimate the free stream turbulence intensity at the inlet position. More comprehensive turbulence measurements are being made in later research.

Chapter III

THE REFERENCE FLOW FIELD

A. Definition of the Reference Flow Field

All the results of this chapter are for one flow field called the "reference" flow field and denoted by REF field. The data for this flow field were obtained under the following conditions:

1. Geometry is the shape of a wide angle diffuser with $L/W = 8$, $2\theta = 50^{\circ}$, aspect ratio of 8 and $W = 3"$ at inlet (fig. I-1). Exit is to the test room with no tail pipe (fig. II-1). The inlet reference point is taken as 6" upstream of the throat, i.e., $X = -6"$ or $X/W = -2$.

2. Radius of curvature at the throat = 0" . That means there is no fairing curve on each side wall at the joint between the divergent and parallel inlet sections.

3. The inlet velocity profile is shown in fig. III-1. Boundary layer profiles at the inlet are almost identical on the two side walls.

	Stalled Side	Unstalled Side
δ^*	0.039"	0.040"
H	1.33	1.33

4. Reynolds no. at inlet

$$R_e = \frac{\rho V_1 W}{\mu}^{\dagger} \approx 2.5 \times 10^5$$

5. There is no forced mixing in the boundary layers. Free stream turbulence at inlet, $\frac{U'}{U} \approx 0.01$.

---

† For the test condition $\mu \approx 1.18 \times 10^{-5} \frac{lb}{ft\ sec}$, $\rho \approx .0753 \frac{lb}{ft^3}$.

B. Dissipation

B.1. Definition of Bernoulli Number, B .

To study the local dissipation in the flow field, the term Bernoulli Number B is defined

$$B(X, Y) \triangleq 1 - D(X, Y) \quad \text{where} \quad D(X, Y) = \frac{P_{T_{\infty_1}} - P_T(X, Y)}{q_1} \tag{III-1}$$

From the above definition, the following properties of B can be deduced.

a. In the whole flow field the highest total pressure is in the free stream of the inlet reference. Therefore, at any other location $D \geq 0$ and $B \leq 1$.

b. $B = 1$ in the main stream if there is no dissipation.

c. The reversed stream comes from the test room. And since $P_{T_{room}} < P_{T_{\infty_1}}$, P_T in the reversed stream is always less than $P_{T_{\infty_1}}$. Hence, B_{rev} never equals 1 and if $B_{rev} = B_{room}$, there is no dissipation.

d. B can become negative when the local total pressure is lower than $P_{T_{\infty_1}}$ by an amount larger than q_1 . This occurs in parts of the boundary layers and also in the stalled region for the case with thick boundary layers (Chapter IV).

B.2. Boundaries of Shear Layers

For mixing of a fast uniform stream U_1 and a slower uniform stream U_2 , the boundaries of the free shear layer are generally defined as the lines joining positions where $U = 0.99\ U_1$ on the high-speed side and $U = 1.01\ U_2$ on the low-speed side. These definitions cannot be adopted for the present study because, near the throat, the free stream velocities are not uniform.

However, at each X location the value of P_T in the main and reversed streams are almost constant. Based on this fact a similar definition can be made as follows:

On main stream side the boundary of the free shear layer, denoted by Y_{ff}, is the points where

$$P_T = P_{T_\infty}(X) - 1\% \, q_1 \qquad \text{(III-2)}$$

On the reversed stream, the boundary, denoted by Y_{fr} is where

$$P_T = P_{T_{rev}}(X) + 1\% \, q_1 \qquad \text{(III-3)}$$

The above equations can be expressed in terms of Bernoulli Number B .

Then Eq. (III-2) becomes

$$B = B_\infty - 0.01 \qquad \text{(III-2a)}$$

and Eq. (III-2) becomes

$$B = B_{rev} + 0.01 \qquad \text{(III-3a)}$$

Boundary layer thickness is defined similarly by equation (III-2) except that the direction of traverse is normal to the wall. Hence, for each boundary layer profile the boundary layer thickness, δ, is the point where P_T first reaches $P_T - 1\% \, q_1$.

B.3. Distribution of B

Local values of B inside the reference flow field are presented in fig. III-2. In this plot a base line is

drawn at an X location where the traverse was made. The distance between a data point and the base line measures the value of B . Negative values are laid out to the left of the base line and positive to the right.

Boundaries of the free-shear layer and the boundary layers are also shown in the same figure. As is the case with the conventional definition of boundary layer thickness, the boundaries defined by the present method cannot be measured exactly. They are drawn with the best possible judgment on the experimental data obtained. Uncertainty can be as high as $\pm$ 0.1" .

As shown in fig. III-2, the boundary layer thickness on the stalled wall increases quite smoothly to join the boundary of the free shear layer on the main stream side. The separation point for this case is at the throat.

Since $B \approx 1$ in the main stream, the main stream is nearly inviscid. Values of B vary markedly in the boundary layers and in the free shear layer indicating large amounts of dissipation, as must be expected.

However, B in the stalled region is almost constant, and is approximately equal to that of the room. This shows that the stalled flow is in this case quite non-dissipative. New fluid continuously flows into the stalled region from the test room, and is dragged out by the main stream. The flow loop for this stall is an open one and should have different characteristics from those of stall with a reattachment which forms a closed "bubble".

C. Pressure Distribution

C.1. Definition of Pressure Recovery Coefficient, C_p

All pressure measurements are expressed in terms of a pressure recovery coefficient defined by

$$C_p(X, Y) \triangleq \frac{P(X, Y) - P_1}{q_1}$$

In the diffuser, C_p is a measure of the amount of momentum flux per unit area entering the channel that is converted to static pressure rise up to section X. This definition of C_p is convenient because by normalizing with inlet dynamic head, consistent values can be obtained even if there is slight variation of inlet flow rate on different days; also results expressed in this form are easily compared with other available diffuser data.

C.2. C_p Along Walls

For the reference flow field, C_p along the two side walls is shown in fig. III-3. Uncertainties for the data in this figure are estimated to be as follows

Within 1" downstream of throat unstalled side	$\pm$ 8%	(20 to 1 odd)
All others	$\pm$ 3%	

These curves have the same trends as those obtained by Feil [1962], fig. I-3.

On the unstalled side, $C_p(X)$ drops rapidly to a suction peak just upstream of the throat, and then recovers rapidly to its final value. If one looks at the sketch in Chapter I (p. 2), it can be seen that sharp bending of the main flow is necessary for such a flow pattern, and may account for the great differences in $C_p(X)$ on the two walls.

Comparing figs. III-3 and I-3, one finds that the final pressure recovery 0.22 of the present flow field falls below that of the smaller angle ($2\theta = 40^\circ$) case of Feil's results with almost the same inlet blockage $\frac{\delta^*_{un} + \delta^*_{st}}{W}$.

It will be shown in Chapter IV that a slight change in curvature at the throat causes recovery consistent with Feil's data.

C.3. C_p in the Flow Field

Distribution of C_p inside the flow field is plotted in fig. III-4. Just as in the dissipation plot, base lines are drawn at traverse locations. Distance from the base line measures the magnitude of C_p with negative values on the left and positive on the right. Values shown at the walls are from fig. III-3, while others are measured by a three-hole probe inserted in the flow field.

Fig. III-4 shows that all major changes in C_p occur within $\pm$ 2W around the throat. The effect of the corner is first sensed at X = -4.25" on the unstalled and at -2.25" on the stalled side.

A large pressure gradient normal to the wall exists around the corner on the unstalled side. This trend is due to the streamline curvatures of the turning flow as would be expected from Euler's n-equation for inviscid flow.

$$\frac{\partial P}{\partial n} = \frac{\rho U^2}{r} \qquad \text{(III-4)}$$

Such normal pressure gradient casts some doubt on the validity of applying the accepted boundary layer equations in Cartesian coordinates for predicting the growth of the boundary layer on this side.

It is normally expected that the pressure across the free shear layer should be constant; however, fig. III-4 shows appreciable pressure changes across the free shear layer near the throat. The variations in pressure decrease to zero as the flow straightens out downstream. Similar trends were observed in the work of Nice, et al [1966] and Chang [1966]. Possible explanations for such behavior are:

a. The value sensed by the probe is actually

$$P = \overline{p} + \frac{1}{2}\rho\overline{U'^2}$$

P is the actual mean static pressure. Hence the variation might be due to the difference of the turbulent normal stress $\frac{1}{2}\rho\overline{U'^2}$ in the free shear layer. Since no turbulence measurements were taken, this possibility cannot be confirmed or denied.

b. The reversed flow being dragged downstream by the main flow turns almost 180 degrees. Streamlines with very small radius of curvature are formed (see fig. III-13). Hence according to Euler's Equation a considerable pressure gradient must exist.

C_p in the stalled region is essentially constant. This means that pressure variation in the reversed flow is small compared to the dynamic head of the main stream. This fact is used as the basis for theoretical arguments in Chapter V on the shape of the displacement line, Y_δ^* , defined in section E.2., p. 29.

It should be noted that pressure output signals from the transducers (Chapter II) are surprisingly steady. Even in the free shear layer, the uncertainty is estimated as only 5 to 8% (20 to 1 odds).

D. Velocity Distribution

D.1. Local Mean Velocity

The conventional method of showing a velocity profile by a plot of magnitude versus location alone causes loss of important information in this case. Consequently, in fig. III-5, local mean velocities are plotted in vector form; the lengths give magnitude and the orientations give

direction. Locations are indicated by intersection of the tails of arrows with the base lines. Since it is difficult to read out numerical values from this graph, Table 1 tabulates all the important quantitative results.

Fig. III-5 shows that fluid coming from the inlet has uniform velocity in the free stream and far upstream is parallel to the center line. The flow starts to turn at about $X = -2.5$. Then acceleration takes place near the unstalled side and deceleration occurs near the stalled wall to give an oblique velocity profile. This behavior becomes more pronounced in the region of the throat as the arrows diverge. Farther downstream the flow smooths out in the free stream (at about $X = 8"$); at this section full pressure recovery is already obtained (see fig. III-4).

The boundary layer separates essentially at the throat on the stalled wall. A free shear layer then develops. This shear layer differs from the type found between two parallel streams; for example, that investigated by Sabin [1964], in the following respects. First, it is initiated from non-uniform flow profiles. Second, at the onset the whole layer does not grow along a straight line. Third, the mixing is between two counter-flowing streams.

The magnitude of U in the reversed flow near the free shear layer is about 7% of V_1. Had the inlet velocity been much less than 100 fps, it would have been difficult to measure U in the reversed flow with the three-hole probe.

When the reversed flow turns around, its velocity does not go to zero. This fact would have been suppressed if the conventional magnitude plot were used instead of the vector form.

A secondary vortex was observed on the stalled wall about 12" downstream of the throat. Obstacles like rods and plates were used to disturb this vortex. These obstacles had no measurable influence on the main flow. In fact, once stall

has been established, a large disturbance at the exit on the stalled area does not change the result in the area where data are taken. Hence, it is concluded that the pattern of reversed flow really does not have a large effect on flow in the area of interest.

Uncertainties (20 to 1 odds) of the results in this section are estimated to be as follows:†

Magnitude:	Free Stream	less than 3%
	Free shear layer and Stalled region	about 8%
Direction:	Free stream	± 1 degree
	Free shear layer	± 3 degrees after correction, see Appendix A
	Reverse flow	± 10 degrees near turning point and where $U/V_1 < 0.03$
		± 5 degrees elsewhere

D.2. Boundary Layer Profiles

As shown in fig. III-1, the boundary layers at the inlet reference point are almost identical on the two side walls and have the typical shape of a turbulent boundary layer on a flat plate. The shape factor H is about 1.33, and the displacement thickness δ^* about .039" on both sides. However, these two boundary layers traverse quite different pressure distributions downstream (fig. III-3), and consequently, their changes in the flow direction are quite different.

a. Unstalled Wall

Fig. III-6 shows the boundary layer profiles on the unstalled wall. The ordinate is normalized on the

† Based on method in Kline and McClintock [1953].

thickness, δ . This figure shows that the profiles are not similar in the physical coordinate, i.e., $\frac{U}{U_\infty} \neq f(\frac{y}{\delta})$.

Around the throat, where the pressure change is most severe, dramatic changes occur in the profile shape. The negative pressure gradient ahead of the throat tends to flatten the profile. Just beyond the throat, the strong adverse pressure gradient almost makes the boundary layer separate as indicated by the profile with inflection point at $S = .55"$. At $S = 1.66"$, the effect of the adverse pressure gradient is still clearly evident in the outer section of the profile, but, at the same time, shear effects near the wall diffuse out. By station $S \approx 7"$, the pressure gradient on the wall has dropped to a low value, but the profile does not return to anything like a flat plate condition until $S = 16"$, just before the boundary layer merges with the free shear layer.

Although the pressure rise that appears just beyond the throat on the unstalled wall is sharper than on the stalled wall (fig. III-3), separation of boundary layer on this side does not occur. A possible explanation is that C_p drops a large amount just upstream of the throat on the same side. The accelerating flow accompanying the pressure drop before the throat has added so much momentum to the boundary layer that it can stand a higher pressure rise than the boundary layer on the stalled wall with an equally steep gradient. If the angle of the channel is increased gradually to the jet region in fig. I-2, the pressure rise beyond the throat would also be increased. Eventually, a point will be reached where the boundary layer cannot stand the pressure gradient without separation. At that condition and for wider angles, separation would occur on both walls; redistribution of

pressure would result, and the jet flow regime is established (see again fig. I-2).†

Figs. III-7a and b show changes of usual boundary layer parameters, δ^* , θ , H and δ along the unstalled wall. Notice the small drop in δ^* , θ ahead of the throat and the sudden increase of all three quantities just after the throat. H finally decreases back to the inlet value at S = 14" .

A cross plot procedure, based on Clauser's [1954] coefficients for the logarithmic law is used to find the wall shear velocity, $u_\tau \triangleq \sqrt{\frac{\tau_w}{\rho}}$, for each of the boundary layer profiles on the unstalled wall (see Schraub and Kline [1965] for discussion of method). With the shear velocities thus

---

† The sketch on the right shows a comparison of Feil's [1962] results of pressure on the side walls of a diffuser in the jet flow regime and one in the two-dimensional fully-stalled regime. Observe that the pressure on the unstalled side of the fully stalled diffuser decreases at the throat to a value much lower than that on either side of the jet flow diffuser; thus the boundary layer on the unstalled wall would gain more momentum than the boundary layer on either of the side walls of the jet flow diffuser at the throat before it traverses the strong positive pressure gradient. This probably explains why the boundary layer remains unstalled when the angle of the diffuser is increased to form a geometry in the hysteresis zone while stalls still occur on both side walls if the same geometry in the hysteresis zone is reached by decreasing the angle from a geometry in the jet flow regime.

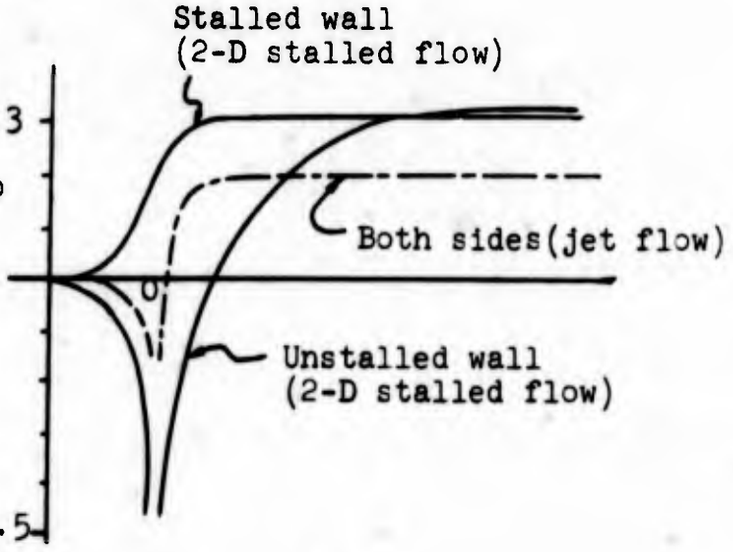

obtained, the usual logarithmic plots of u^+ vs y^+ (i.e., $\frac{U}{u_\tau}$ vs $\frac{yu_\tau}{\nu}$) are obtained for a few profiles and shown in fig. III-8. As can be seen in this figure, most of the boundary layer profiles do have a logarithmic region, and fall close to Clauser's equation. The logarithmic region is more extensive for profiles under negative pressure gradient, and is shortest for the profile with strongest local adverse pressure gradient.

The friction factor C_f, is related to the shear velocity and the velocity at the edge of the boundary layer by the expression

$$C_f = 2\left(\frac{u_\tau}{U_\delta}\right)^2 = 2\,\frac{1}{u_\delta^+}$$

C_f data obtained by this equation for the unstalled boundary layers are presented in fig. III-9. Since some of the profiles do not fall exactly on Clauser's equation, and since there are not very many points in the logarithmic region to give a good average, uncertainties in the numerical values can be as high as $\pm$ 20%. Consequently, this figure can only compare trends on the two walls.

b. Stalled Wall

Measurements on the boundary layer profiles along the stalled wall were carried out only up to slightly beyond the separation point. In the reversed flow region, the boundary layers are very small and magnitudes of velocity in them are too small to be determined with acceptable accuracy. Fortunately, as discussed in section D.1. on local mean velocity, they should not have any appreciable effect on the whole pattern. Ignoring their shape will not affect the main results in the present study.

The separation point is found to be at the throat in this flow field. Several profiles of the boundary layers on the stalled wall are shown in fig. III-10. The profiles between $X = -6"$ and $X = -1.5"$ are almost identical to the inlet profile. At $X = -1.5"$ the boundary layer starts to thicken a little and quickly separates at the throat. Reversed flow is seen in the profile just downstream of the separation point at $X = 0.5"$. The inflection point that generally exists in a separated profile can be observed here. Since this separated profile is obtained by matching two traverses, uncertainty around the matching point is quite high. By graphical integration the location of the dividing streamline is found to be 0.3" away from the wall; this checks quite well with the streamline pattern in fig. III-13.

Fig. III-11 shows δ^*, θ, H for boundary layers on the stalled side. The jump in values after the throat is so huge that instead of treating as a boundary layer profile, one should actually consider points at $X = 0.5"$ as a combination of the free shear layer and reversed flow.

A cross-plot method, similar to that used for the profiles on unstalled wall, was applied to the profiles before separation (fig. III-12). They were found to follow Clauser's correlation very closely. However, such a logarithmic plot does not apply to the separated profile at $X = 0.5"$. Fig. III-9 shows a decrease in C_f on the stalled side before separation. This trend is expected due to adverse pressure gradient shown in fig. III-3.

Separation criteria by previous authors will be used in Chapter V, p. 55, to compare with all the boundary layer measurements in the present study.

E. Stream Line Pattern

E.1. Definition of Stream Function, $\Psi(X, Y)$

u , v , components of velocity can be obtained by decomposing the vectors in the X and Y directions. From a complete plot of u in the field, graphical integration yields the streamline pattern shown in fig. III-13. The local value of the stream function $\Psi(X, Y)$ is obtained by

$$\Psi(X, Y) \triangleq \frac{1}{W} \int_{Y_{st}}^{Y} \frac{u(X, \xi)}{V_1} \, d\xi \; ; \text{ at fixed } X \qquad \text{(III-5)}$$

From the above definition it is obvious that $\Psi = 0$ on the stalled wall. That $\Psi = 1$ on the unstalled wall can be shown by applying Eq. (III-5) at the inlet, ($X = -6"$), where $Y_{st} = -\frac{W}{2}$, and by combining with the definition of V_1 ,

$$V_1 = \frac{1}{W} \int_{-\frac{W}{2}}^{\frac{W}{2}} u(-6" \, , \, \xi) \, d\xi$$

E.2. Dividing Streamline, $\Psi_d(X)$

Since $\Psi(X, Y)$ is a continuous function of both X and Y , between the negative values of Ψ in the reverse flow region and the positive values in mainstream at fixed X , a point Ψ_d must exist where Ψ equals 0 . Ψ_d is thus defined by

$$0 = \frac{1}{W} \int_{Y_{st}}^{\Psi_d(X)} \frac{u(X, \xi)}{V_1} \, d\xi$$

The locus of $\Psi_d(X)$ is also a streamline; it is often called the dividing streamline of the separated flow field.

Physically the dividing streamline is the boundary between the fluid flowing from the inlet side and that from the exit in the reverse stream. This fact can be shown by applying the continuity equation to the control volume below:

Continuity:

$$\dot{M}_1 = \dot{M}_2$$

where

$$\dot{M}_1 = \rho b \int_{Y_{st}(X_1)}^{Y_{un}(X_1)} u(X_1 , \xi)\, d\xi$$

$$\dot{M}_2 = \rho b \int_{Y_{st}(X_2)}^{Y_{un}(X_2)} u(X_2 , \xi)\, d\xi$$

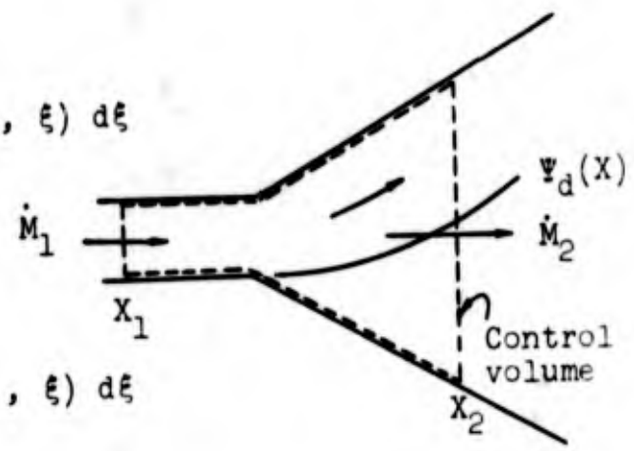

$$= \rho b \int_{Y_{st}(X_2)}^{\Psi_d(X_2)} u(X_2 , \xi)\, d\xi + \rho b \int_{\Psi_d(X_2)}^{Y_{un}(X_2)} u(X_2 , \xi)\, d\xi$$

First term on the right side of last equation = 0 by definition of Ψ_d. So

$$\int_{Y_{st}(X_1)}^{Y_{un}(X_1)} u(X_1 , \xi)\, d\xi = \int_{\Psi_d(X_2)}^{Y_{un}(X_2)} u(X_2 , \xi)\, d\xi \qquad \text{(III-7)}$$

Eq. (III-7) was also used to check on the accuracy of integration and consistency of data. The maximum difference obtained was $\pm$ 0.1" . Since considerable interpolation from boundary layer measurements was needed to complete the u component plot to the unstalled wall, it is believed the result obtained by integration from the stalled side using Eq. (III-5) is more dependable.

The dividing streamline also serves two other purposes. First, it is used to check the position of the separation point. The dividing streamline originates from the separation point on the stalled wall. Extrapolating its shape upstream by a smooth curve to intersect with the stalled wall is one method of locating the separation point.

Second, based on the dividing streamline another line can be defined to extend the concept of the locus of the displacement thickness of the boundary layer to the free shear layer. The following expression defines the displacement on the main stream by the free shear layer.

$$\delta_f^*(X) \triangleq \int_{Y_d(X)}^{\delta_{fm}(X)} \left[1 - \frac{u(X\ ,\ \xi)}{u_{\delta_{fm}}} \right] d\xi \qquad \text{(III-8)}$$

The locus of δ_f^* is then called the <u>displacement line</u> denoted by Y_δ^* . This line is plotted in fig. III-14 and is shown to merge smoothly with the locus of the displacement thickness of the boundary layer before separation.

E.3. <u>Effective Channel for Main Stream</u>

In fig. III-14 a curve joining displacement thicknesses of the boundary layers on the unstalled side is also shown. Beyond X = 8" this curve is almost parallel to the Y_δ^* (X) line. Ideally the area between these two

curves is the effective passage area for diffusing the main flow in a manner analogous to application of the concept used in predicting the performance of an unstalled diffuser and is, therefore, called the effective channel. Applying 1-D inviscid theory to this channel, the C_{pi} at section 2 is evaluated by

$$C_{pi_2} = 1 - \frac{1}{AR^2} \qquad AR = \frac{A_2}{A_1} \tag{III-9}$$

It is found to be approximately 0.25 which is higher than the experimental result 0.22 . But keeping A_1 = constant, the uncertainty in this calculation can be estimated by

$$\Delta C_{p2} = \left(\frac{1}{1 - C_{p2}}\right) \frac{dA_2}{A_2}$$

Since A2 can be accurate only to $\pm$ 0.1" , $\Delta C_{p2} \sim \pm 0.04$; so the check is just within the uncertainty in the result.

If the free streamline concept of Helmholtz-Kirchoff is applied to the present situation and the effects of displacement by boundary layers and the free shear layer neglected, then the pressure distribution in the main flow would be expected to be governed by a channel bounded by the solid walls before separation and by the dividing streamline beyond the separation point. However, applying one-dimensional estimation to this free streamline channel in fig. III-14, one would obtain

$$C'_{pi_2} = 1 - \left(\frac{A'_1}{A'_2}\right)^2 = 0.41$$

which is almost two times the value measured.

Thus, it is believed that effects of displacements are important and that pressure distribution depends on the effective channel defined at the beginning of this section, rather than on a channel with free streamline and solid wall as boundaries. This result is entirely consistent with prediction procedures for unstalled channels as shown by Reneau et al [1964] and Sovran and Klomp [1967].

F. Final Remarks

In fig. III-15, some of the quantities discussed above are plotted together for several positions. This figure shows more clearly the local relative magnitudes of those quantities and provides an integrated picture. Observe, for example, that the directions of velocities agree well with the slopes of the streamlines and that C_p is uniform where the velocity is in the reverse direction.

Chapter IV

EFFECTS OF CHANGE OF GEOMETRIC AND FLOW PARAMETERS

A. Curvature at the Throat

Effects due to change of curvature at the throat are discussed below. Data in this section were obtained under the same conditions specified on page 14 for the reference flow field except that the radius of curvature at the throat section was changed from 0" to 8" . This flow field is called the RC8 field while the original one is called REF field.

A.1. Separation Point

By changing the radius of curvature to 8", the channel width at the throat is enlarged from 3" to 3.3" . Separation point is moved from (X, Y) = (0" , -1.5") in the reference field to (X, Y) = (0.25" , -1.76") in this new field. A new effective channel is formed. The pressure and velocity distributions also change by appreciable amounts.

A.2. Distribution of Bernoulli Number, B

Fig. IV-1 shows the distribution of B in the RC8 field. Boundaries of the different zones defined on page 16 are obtained from this distribution, and compared with the loci for reference field. Downstream of the throat on the unstalled side, the boundary layer is much thinner than in the reference field although they are almost identical before the throat. On the stalled side, however, δ increases appreciably before separation, unlike the REF case. The free shear layer thus developed after separation in the RC8 field spreads much faster than in the REF case. The reversed flow region in the RC8 case is again essentially non-dissipative, but is smaller in size because of the thicker free shear layer. The inviscid region in the main stream remains almost the same size, but appears to have been shifted closer to the unstalled wall.

A.3. Pressure Distribution

Pressure distribution along the two walls are shown in fig. IV-2. Quantitative differences between these results and those of REF field are appreciable. First, the final C_p rises from 0.22 to 0.34. Second, C_p on the stalled wall rises more sharply while on the unstalled side the change is more gradual than before.

Similarities also exist between the two cases. Full recovery occurs on the stalled side at $X = 0.5"$. The value of C_p on the unstalled side increases to that on the stalled wall at about $X = 7.5"$; there is no apparent change in C_p beyond $X = 9.5"$.

Fig. IV-3 shows the distribution of C_p in the flow field. Values of the reference field are represented by dash lines for comparison. Although the values are quite different for the two cases, the profile shapes are almost identical at most X stations. Normal pressure gradients exist at the unstalled wall around the throat, but are not as sharp as in the reference field. Pressure bumps also occur in the free shear layer, and pressure profiles become flat beyond 2W down stream of the throat.

The final recovery value of 0.34 in the new field agrees well with the data of Feil [1962], fig. I-3.

A.4. Boundary Layers

Boundary layer profiles on the unstalled wall are shown in fig. IV-4 and the boundary layer parameters in fig. IV-5. Just as in the reference flow field (fig. III-6), the profile flattens and then thickens at the throat. However, in spite of the higher final pressure recovery in this flow field, pressure gradient around the throat is actually milder than before. Consequently the change in profile shape is more gradual (e.g., change in profile from $X = -0.5"$ to $X = 0.5"$ is much less severe than in the reference field (fig. III-6)).

Referring to fig. IV-5a, one finds that value of δ far downstream only rises to about half that of the reference case. In fig. IV-5b, both δ^*, θ are thinner than in the REF case, and they also change more gradually. However, H has a higher value before the boundary layer merges with the free shear layer at about X = 16".

Values of C_f along the two side-walls are shown in fig. IV-6. On the unstalled side, response of C_f to the change of C_p around the throat is also slower in this case than before. On the stalled side, C_f at $X \approx -0.5$" for the RC8 case has a lower value than that of the REF case at the same position.†

Fig. IV-7 compares the boundary layer profiles near separation. At S = -0.5" the position is about 3/4" away from the separation point in the RC8 field, but the boundary layer is thicker than the corresponding one for the REF field which is only 1/2" from the separation position. In addition inflection begins to appear at the inner part of the profile at this point for the RC8 case but not for the REF case. This is consistent with the lower measured value of C_f at the same position.

Fig. IV-8 shows the boundary layer parameters before separation. The jumps in δ^* and H are smaller than in

---

† If the values of C_f for both cases are extrapolated to the separation points, it seems that at separation C_f would reduce to zero for the RC8 case but not for the REF case. Probably the separation phenomena are different for the two cases. In the reference field, separation may be like that on a backward facing step where the boundary layer leaves the wall because of the discontinuity in slope of the wall. In the RC8 field the boundary layer loses momentum, thickens, and then separates at a point where the wall shear stress has reduced to zero.

the reference field because the boundary layer changes shape more rapidly before separation in this case.

All boundary layer parameters are tabulated in table 4.

A.5. Velocity Field

Local velocity data for this RC8 field are tabulated in table 2. Fig. IV-9a compares velocity distribution at $X = 1.75"$ for the REF field and the RC8 field. Near the unstalled wall, velocity vectors of the two cases have quite different orientations because of the different wall shapes at the throat. In the main stream, where flow is inviscid, the RC8 field has lower velocity than the REF field. This is consistent with the higher measured values of C_p.

The velocity profile in the free shear layer for the RC8 case is flatter than for the REF case. Since the separation point is at a lower Y coordinate, the point where reversed flow turns around also occurs at a lower Y.

Fig. IV-9b shows similar plots at $X = 5.75"$. The same remarks as for the last figure apply. In addition, at this section the reversed flow has higher velocity for the RC8 case. Since the velocity in the main stream is lower than the REF field, one cannot assume that a higher main stream velocity would cause a faster reversed flow.

A.6. Streamline Pattern

Comparison of streamline patterns is shown in fig. IV-10. The two fields have same streamlines near the inlet, $X = -6"$. Around the throat, except for $Y = 0.4$, deviations are quite appreciable. As is to be expected, after rounding the throat section, the streamlines for the RC8 case tend to bend more gradually. Downstream, where final pressure recovery has been reached the new streamlines are more widely spaced due to lower velocity than in the REF

field. $\Psi = 0.8$ is also closer to the unstalled wall because of thinner boundary layers.

The dividing streamline, Ψ_d , in this field originates at a different location, and is thus quite different from the REF one. It also leaves the stalled wall at a steeper slope and then becomes parallel to the REF one at about $X = 10"$.

A.7. Effective Channel

The effective flow channel of the RC8 case is compared with that for the REF case in fig. IV-11. One dimensional ideal pressure recovery coefficient is calculated at station 2 for the RC8 case. The result is

$$C_{pi_2} = 1 - (A_1/A_2)^2 = 0.33 \quad \text{(uncertainty 0.04, 20 to 1)}$$

This agrees very well with the experimental recovery value, 0.34 . As in the REF case this estimate is much better than that obtained by free streamline method neglecting the effects of displacements:

$$C'_{pi_2} = 1 - (A'_1/A'_2)^2 = 0.46$$

Just before $X = 0"$ the displacement line, Y_{δ^*} , of the RC8 field is still almost flat, and then it bends more sharply than the REF one. This would explain why along the stalled wall, C_p starts increasing at a position nearer the throat and also at a higher rate (fig. IV-2).

The boundary of the channel is smoother on the unstalled wall than the reference one. This is the reason for the more gradual change of C_p on the unstalled wall (fig. IV-2).

From the above facts, it may be concluded that the pressure distribution in the flow field is very possibly governed by the shape of the effective channel. Smoothing the throat increases the final width of the effective channel and better diffusion is thereby obtained.

The work of Copp [1951] shows that the curvature at the throat does not affect pressure recovery in an unstalled diffuser. In unstalled channels, recovery is chiefly governed by the overall area ratio of the channel. This is not true for the fully stalled flows where pressure recovery is governed by the effective channel. In a sense, the flow "makes its own area ratio." Radius of curvature at the throat affects the effective channel shape sufficiently to make significant changes in the pressure distribution.

In fig. IV-11, the line of zero u-component for the two fields are also compared. The REF zero u line lies above the RC8 one possibly because the free shear layer is thinner in the reference flow field.

B. Inlet Boundary Layer Thicknesses

Another flow field study was done with the boundary layers thickened to form an almost fully developed channel flow at the inlet reference point, X = -6". The profile for this flow is compared with the reference one in fig. IV-12. The shape factor, H , is almost the same as before on both side walls although the displacement thickness, δ^* , is increased from 0.039" to 0.152" on the unstalled side and from 0.040" to 0.142" on the stalled side.

The radius of curvature is kept at 0" as in the reference field, and Reynolds No, $\frac{\rho V_1 W}{\mu}$, at inlet still equals approximately 2.5×10^5 . Since the boundary layers have been thickened to occupy almost the whole inlet section, turbulence intensity in the free stream increases from about 1% to about 8%. The flow field defined by these new inlet conditions is denoted "TKD field."

B.1. Separation Point

The separation point for the TKD field occurs at $X = 0.25"$ on the stalled wall. This position is farther downstream than the one separation point in the reference field.

B.2. Distribution of B

Fig. IV-13 shows the distribution of B in the TKD field. Since the inlet boundary layers are much thicker than those in the reference field, both the unstalled boundary layer zone and the free shear layer are much larger than before. They also merge together very quickly leaving a very small free stream region where dissipation is less than 1% of q_1. In the reversed flow region B has negative values. As explained on page 15, this is because P_T of the test room is less than $P_{T\infty_1}$ by an amount more than q_1.. As the B value is almost constant, there is still very little dissipation in this region.

B.3. Pressure Distribution

C_p along the walls and in the flow field for the TKD case are shown in figs. IV-14 and IV-15 respectively. The final pressure recovery coefficient is 0.20 as compared to 0.22 in the reference field. Pressure change around the throat is slightly more gradual. Aside from these two points the main features, including the locations of full recovery and profile shapes on the distribution of C_p, remain the same as before.

B.4. Boundary Layers

The boundary layer on the unstalled side undergoes changes in profile shape as in the reference field. Fig. IV-16 shows the profiles at several locations. Inflection points

again exist in profiles just downstream of the throat. At $X = 10"$, where the unstalled boundary layer has already merged with the free shear layer, an inflection is still clearly evident, and the profile is still quite different from that of a turbulent boundary layer along a flat plate.

Since $\delta_{TKD} < \delta_{REF}$ at inlet, δ_{TKD} is thicker along the wall, but its growth rate is much slower as shown in fig. IV-17a. δ^*, θ are plotted in fig. IV-17b. In spite of the difference in magnitudes, changes in both δ^* and θ have the same trends as in the reference field. These values are also tabulated in table 4.

Fig. IV-18 shows the change of H for all three flow fields along the unstalled wall. The response of H to pressure change around the throat for the TKD case is between the REF and RC8 case. A possible explanation is that the thicker boundary layer, in effect, "smooths out" the sharp corner slightly. Hence, the flow senses an effective throat shape with radius of curvature between 0" and 8".

C_f is shown in fig. IV-19. Values of C_f on both sides are lower than the reference values but similar trends can be observed. Uncertainties of numerical values of C_f can be as high as 20% for the REF case. Because of more fluctuation in boundary layer measurements uncertainties of C_f for the TKD case would be even higher.

Boundary layer profiles around the separation point are shown in fig. IV-20. As in the REF flow, the profile at $S = -0.5"$ for this case does not differ very much from that at $X = -6"$.

B.5. Velocity Field

Velocity distribution in the TKD field is tabulated in table 3. Fig. IV-21 shows the profile at $X = 1.75"$. As expected, the profile is quite different from that for the REF case since it develops from a different inlet velocity

profile. In the thick free shear layer velocity change is more gradual. To keep V_1 the same as the reference, U/V_1 in the free stream has a higher value.

B.6. Effective Channel

Referring to fig. IV-21, one can observe the following comparison of the important loci between the TKD and the REF field.

Thicker boundary layers at the inlet reduce the size of the effective channel. Differences between the boundary layer displacements are more distinct than between the displacement lines. Boundaries of the effective channel in TKD field are smoother around the throat than in the REF case. This may explain the slightly more gradual change in C_p as shown in fig. IV-13.

Ideal final pressure recovery at location (2)

$$C_{pi_2} = 1 - \left(\frac{A_1}{A_2}\right)^2$$

is estimated to be 0.26. The difference between this and the experimental value, 0.20, is a little higher than the estimated uncertainty of 0.04, from error in graphical integration to obtain the displacement line. Viscous dissipation probably causes this decrease in measured value.

If displacement due to boundary layers and the free shear layer is neglected, then ideal pressure recovery at location 2 is

$$C_{pi_2} = 1 - (A_1'/A_2')^2 = 0.43$$

which gives a much worse estimate than by using the effective

channel. This again emphasizes the importance of boundary layer displacement effects in internal flow.

The dividing streamline in the TKD field leaves the wall at X = 0.25" as compared to 0" for the REF field. An explanation may be based on two grounds. First, the thicker boundary layer in effect, senses a smoother throat than the sharp edge. Second, more turbulence in the channel may have added energy to the boundary layer so it can move farther downstream before it separates. The effect of forced turbulent mixing on C_p along the walls will be discussed in the following section.

C. Turbulent Mixing in the Boundary Layers at Inlet

Effects due to two types of boundary layer mixing devices, vortex generators and wedges attached at walls upstream of the inlet reference section were studied briefly.

C.1. Vortex Generators

Vortex generators were attached at X = -12" on both side walls. A sketch of the arrangement is shown on the following page; more detailed dimensions can be found in fig. IV-23. With the vortex generators in place, the boundary layers at inlet, X = -6" are thinned but shape factors H remain almost unchanged as shown in fig. IV-24. The separation point was found to have moved to X = 0.25". Fig. IV-25 shows C_p along the walls. Although there are differences near the throat, the final C_p remains the same as in the REF case. It is believed that the thinner boundary layers have changed the effective channel shape by widening both sections at inlet and far downstream, but at the same time keeping the ratio A_1/A_2 constant.

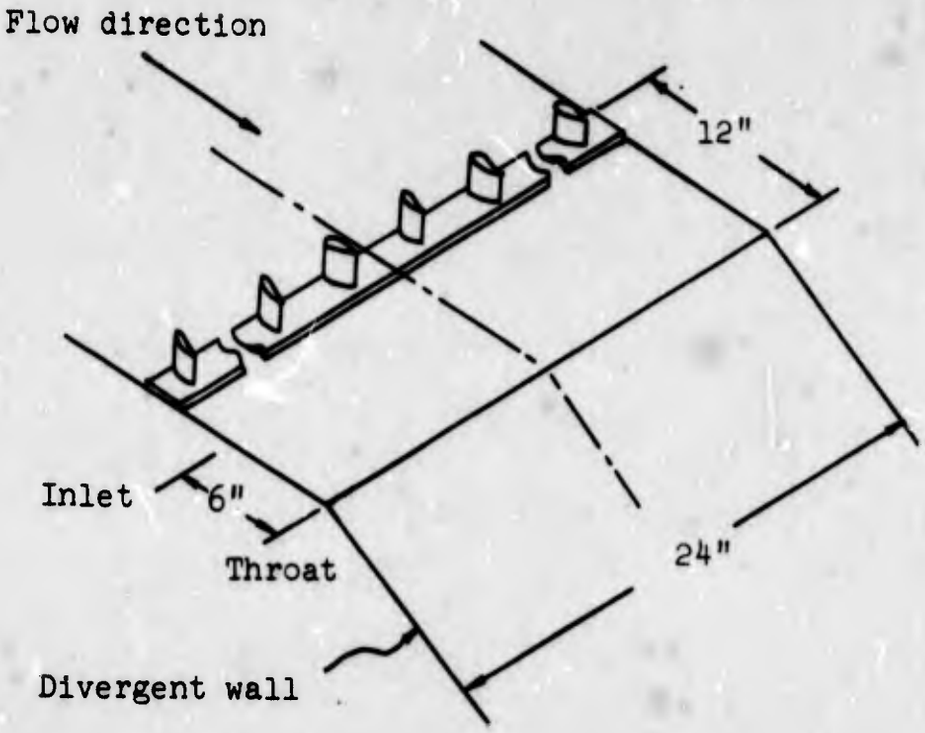

Location of vortex generator on side wall

C.2. Wedge at X = -15"

Another brief study was made with a wedge strip attached at X = -15" on each side wall. The arrangement is shown on the following page. Since the wedges cause strong local separation of the boundary layers, they have to be attached farther upstream than the vortex generators to avoid too much distortion of the profile at inlet.

Velocity profiles at the inlet are also plotted in fig. IV-24 and C_p in IV-25. In this case, the separation point was moved to about X = 0.5". Final pressure recovery increases from 0.22 to 0.25. Separation being farther downstream has widened the effective flow channel by diverting the displacement line but, on the other hand, the thicker unstalled boundary layer also decreases the channel size both at inlet and at the location of full recovery.

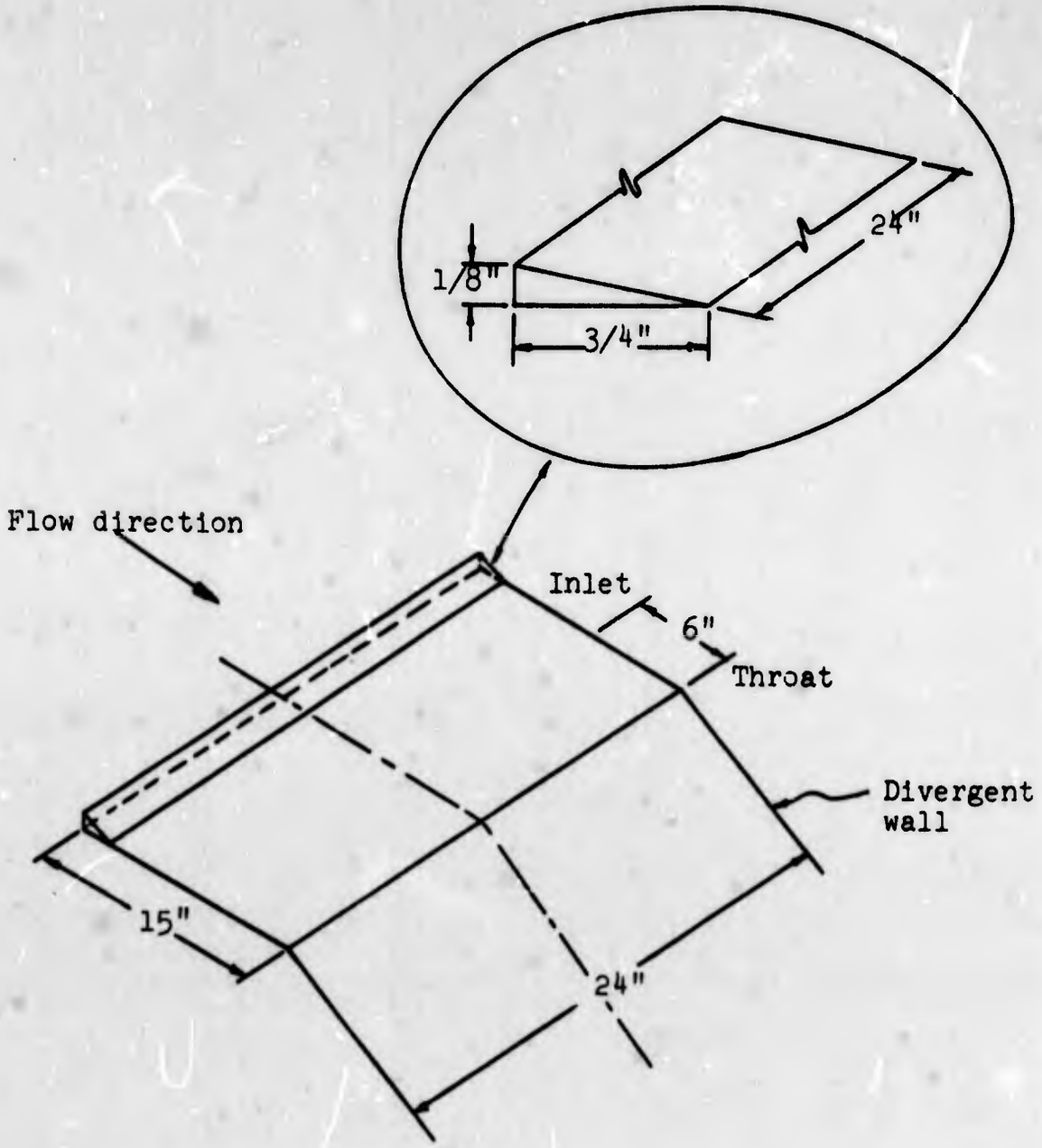

The exact effects of turbulence mixing cannot be concluded here. However, it is found that mixing can shift the separation point and change inlet velocity profile which, in turn, can change the shape of the effective channel and the pressure distribution. To obtain correlations and understand further what happens in the flow field, more systematic studies with different wedge sizes and shapes and more detailed turbulence measurements would be needed.

D. Reynolds Number

A test was performed with the Reynolds Number at the inlet reduced to 1.4×10^5 . Boundary layer shapes and parameters at inlet remain almost the same. C_p along the two walls also does not change. Thus it is concluded that change in Reynolds Number between 1.4×10^5 and 2.5×10^5 has no effect on the results in the reference field as long as the data are normalized to the inlet condition as before.

E. Remarks on Base Pressure

Chapman [1951] showed that the base pressure at the end of a finite cone cylinder for axisymmetric supersonic flow is independent of the Reynolds number when the boundary layer is turbulent. This finding is consistent with the result presented in the last paragraph about the effect of Reynolds number on the final pressure recovery coefficient. The same report shows that the base pressure can be correlated with the boundary layer thickness just before separation. For the present study correlation of final pressure recovery coefficients with boundary thicknesses on the stalled side does not seem possible. Pressure distribution in the present flow channel is mainly governed by the shape and size of the effective channel. The boundary layer on the stalled side alone does not define the effective channel. Consideration has to be given to the development of boundary layers on both side walls as well as the free shear layer.

Chapter V

ANALYTICAL MODEL

A. Problem Proposal

A primary purpose of any analytical solution to an engineering problem is to eliminate further unnecessary experiments by solving mathematical equations formulated from available physical understandings of the situation.

For the present study a most useful analytical tool would be one that could be used to predict mathematically all the detailed flow data presented in the last two chapters. However, since exact solutions for viscous flow are possible only in a limited number of situations, and since calculation of turbulent flow fields is still not well developed, a detailed solution to such a complicated problem is not to be anticipated in the near future.

A simpler task would be to predict the steady-state equilibrium flow configuration when the geometry and inlet conditions are specified; a calculation method is proposed below for this purpose. As will be discussed, even this simplified problem calculation cannot be handled easily. Indeed, a solution to this simplified problem is not given herein, owing to time limitations on the current program. However, its feasibility is considered, and suggestions are put forward for further theoretical studies.

B. Formulation of Calculation Method

A central conclusion from the experimental data is that the effective channel governs the pressure distribution in the flow field. The effective channel is the area between the loci of the displacement thickness of boundary layers added on to the solid walls, δ^*_{un} and δ^*_{st}, and the displacement line, $Y_\delta{}^*$, after the boundary layer separates. To determine

the effective channel shape, one must be able to calculate the displacement thicknesses on both sides of the effective passage whether they be defined by a solid wall or by a free shear layer.

However, displacement thicknesses of boundary layers are strongly affected by pressure gradients. Hence, there is a non-negligible interaction between the boundary layer calculations and the inviscid calculation in the effective channel. To predict the equilibrium flow configuration some iterative procedure must be employed.

For a wholly inviscid flow field, the velocity at the inlet of the effective channel could be assumed as uniform, and the entire flow would be irrotational. Two-dimensional inviscid irrotational flow is governed by LaPlace's equation

$$\frac{\partial^2 \Psi}{\partial X^2} + \frac{\partial^2 \Psi}{\partial Y^2} = 0 \qquad \text{(V-1)}$$

This equation is of the elliptic type. Solution is possible if and only if either Ψ or $\partial\Psi/\partial n$ is specified for each point on the boundary.

Therefore, even though the boundary layer equations are parabolic, step by step parabolic type iteration from the initial point cannot be used. Each iteration step must involve the whole field. Convergence is then sought through the matching of the effective channel shape.

The proposed calculation procedure consists of the following steps:

1. Assume an effective channel shape.

2. Calculate the flow in the channel assumed in step 1 using wholly inviscid flow theory.

   a. Solve LaPlace's equation for Ψ in the channel.

b. Calculate C_p along the boundaries of the effective channel from Y distribution obtained in 2a.

3. Perform a boundary layer calculation using the C_p values obtained in 2b. Use an appropriate boundary layer calculation method to calculate the growth of δ^*, θ and H. Calculation terminates when separation is approached.

4. Check matching conditions for convergence, that is, for agreement of assumed and calculated effective channel shape. Adjust channel shape and repeat 2 to 4 until conditions are fulfilled.

Each of the above steps will be discussed in the following sections. Data in the RC8 field will be used for checking the validity of part of the calculation prodedures.

C. Shape of the Effective Channel

From the data presented in Chapters III and IV, it can be seen that once separation occurs, C_p in the stalled region is essentially constant.† This is necessarily so because the reversed flow is dragged into forward motion by the main flow (see Appendix B). Its velocity is less than one-tenth that in the mainstream, and thus any pressure variation in the stalled flow will be less than one-hundredth of the mainstream dynamic head.

The displacement line, Y_δ^*, is near the boundary of the stalled region. As C_p is a continuous function in space, it is expected that C_p along this line beyond the separation point should also be almost constant. Fig. V-I shows C_p along this line for the REF and the RC8 fields. Aside from

---

† At least to the order that $\dfrac{(\Delta C_p)_{\text{stall zone}}}{C_{p_{\text{overall}}}} \ll 1$

the slight deviations near the throat, which are probably due to turbulent stress in the free shear layer, the constancy of C_p is well confirmed.

Hence, if the flow is stalled, the conclusion in the above paragraph that C_p = constant along the boundary is a condition that the shape of the effective channel must satisfy. To satisfy this condition downstream, where effects of the throat on turning of the main stream line have diminished, the effective channel must be straight and of constant or nearly constant area. Two flow patterns are known that satisfy this condition.

1. If separation occurs on one side wall only, such as in this study, the displacement line must eventually be parallel to the locus formed by adding the displacement thickness of the unstalled boundary layer to the unstalled wall shape. See sketch (a) below. This is the case in the present data.

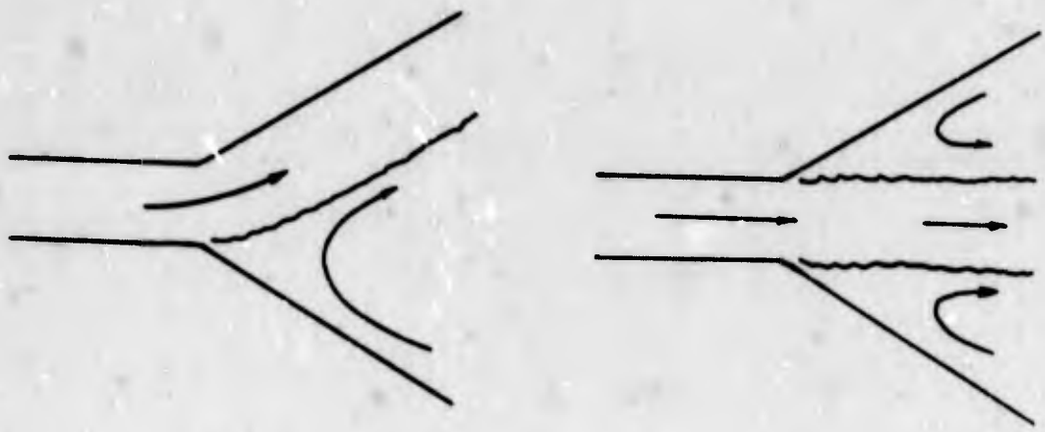

(a) (b)

2. If separation occurs on both side walls, displacement lines on both sides must be parallel to the center line of the flow channel (see fig. b above).

A configuration like fig. c is impossible because in subsonic flow the static pressure of the fluid must match

the pressure in the test room at exit, and so the constant value of C_p along both displacement lines, must equal $C_{p_{(room)}}$. Hence, beyond the separation points, C_p should be identical on the two displacement lines. Bending of streamlines in fig. (c) implies that there is a pressure gradient across the channel contradicting the conclusion just obtained.

(c)

Therefore, for flow in a diffuser without a tail-pipe only three different <u>stable</u> flow configurations exist -- the unstalled regime, two-dimensional fully stalled regime, and the jet flow regime (see fig. I-2).

Around the throat the shape of the displacement line depends on the geometry of the smoothing curve between the parallel and the divergent section. It should bend in such a way that the turning effects of the mainstream lines be compensated to give constant C_p. To construct its shape, standard procedures for free streamline theory (see for example Valentine [1961]) would help. But it must be kept in mind that in this case the displacement line, Y_δ^*, is to be treated as the free streamline and not the actual dividing streamline that originates from the solid wall. Otherwise as pointed out in experimental results, if displacement

thicknesses are neglected, the final pressure recovery coefficient would be almost two times that measured in experiment.

D. Inviscid Calculation

D.1. Potential Solution for $\Psi(X, Y)$

The stream function in potential flow is governed by Eq. (V-1). In mathematics this equation, with the boundary conditions Ψ = constant on the boundaries, is called the Dirichlet's problem. For engineering applications there are many practical calculation methods to obtain exact or approximate solutions, for example, conformal mapping, finite difference and electric analog methods. Each has its advantages and disadvantages. Robertson [1965] gives a very good discussion of most of the methods.

For the present problem, a numerical solution is preferable for two reasons. First, the boundary of the effective channel in general cannot be represented by algebraic equations. Thus exact analytical methods, such as integral equations and conformal mapping, do not seem appropriate. Second, adjustment on the channel shape is needed for each step of iteration. With finite difference methods, a solution can be obtained by a computer program which takes discrete points representing the boundaries as inputs. Then each of the individual discrete boundary points can be perturbed to give a new solution when adjustment is needed in the next step of iteration.

There are many references to numerical solutions of the Dirichlet problem, for example, Fox [1962]. A common method is to divide the channel into small grids by equally spaced vertical and horizontal grid lines. At each grid point, Eq. (V-1) is approximated by either of the following finite difference equations. If grid point is near boundary, see sketch (d) on the following page.

$$\left(\frac{2}{\lambda_x} + \frac{2}{\lambda_y}\right)\Psi(m,n) - \frac{2}{(1+\lambda_y)}\Psi(m,n-1) - \frac{2}{(1+\lambda_x)}\Psi(m-1,n) \quad \text{(V-2a)}$$

$$= \frac{2}{\lambda_x(1+\lambda_x)}\Psi_1(m+\lambda_x,n) + \frac{2}{\lambda_y(1+\lambda_y)}\Psi_2(m,n+\lambda_y) \quad \text{(V-2b)}$$

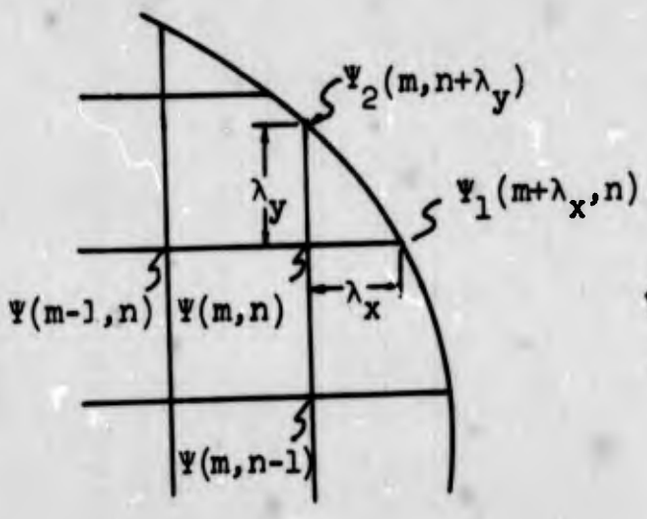

(d)

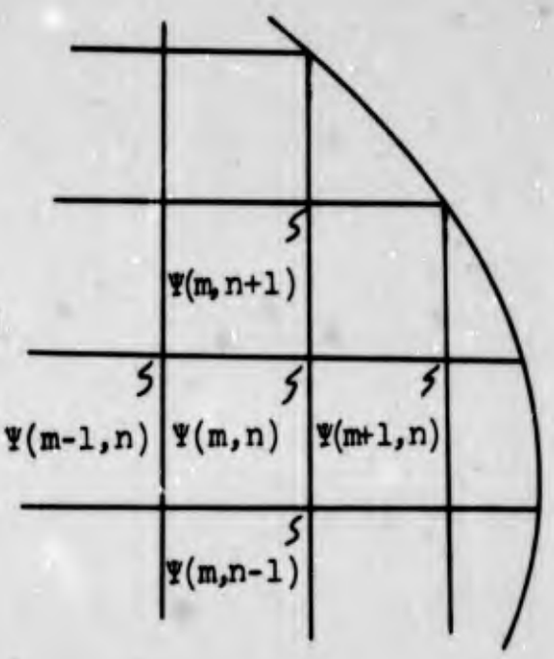

(e)

If all adjacent grid points are inside channel, see sketch (e).

$$4\Psi(m,n) - \Psi(m-1,n) - \Psi(m+1,n) - \Psi(m,n+1) - \Psi(m,n-1) = 0$$

To check the validity of the proposed model, such a method is applied to the effective channel of the RC8 case shown in fig. IV-11 with the following inputs.

Inlet	:	X = -6"
Exit	:	X = 8.0"
Grid size	:	1/2"

Ψ on δ^*_{un} on unstalled side = 1

Ψ on δ^*_{st} and $Y_\delta{}^*$ on stalled side = 0

Uniform velocity at inlet and exit, i.e., distribution of Ψ on boundaries X = -6" and X = 8" is linear. (See sketch (f) below.)

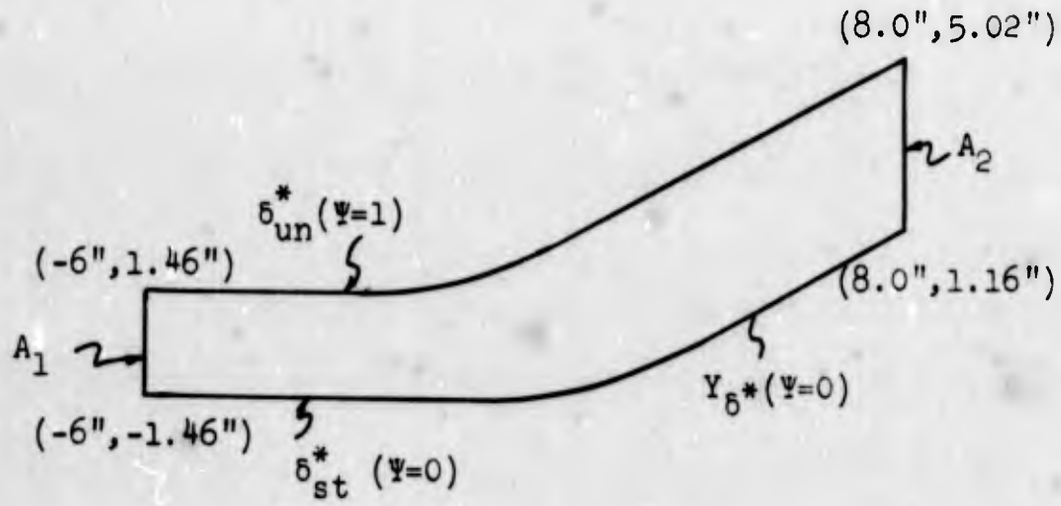

On A_1 : $\Psi = (Y" + 1.46")/2.92"$

On A_2 : $\Psi = (Y" - 1.16")/3.86"$

(f)

A computer program in Algol was written to find the coefficients of the equations defined in Eqs.(V-2a,b). With the 1/2" grid size, a system of 155 equations was obtained and solved by the direct Gauss method. The bivariate interpolation formula was used to obtain locations for the analytical streamlines shown in fig. V-2.

Even though the grid size chosen is quite large for the effective channel, the numerical calculation results check quite well with the experimental values. This indicates that the streamline pattern is defined by the shape of the effective channel if δ^*_{un} and Y_{δ^*}, δ^*_{st} are treated as streamlines in analysis.

D.2. Pressure Distribution by Inviscid Calculation

After obtaining the ideal solution for stream function, C_p can be obtained from the Bernoulli equation as

$$C_p = 1 - \left[\left(\frac{\partial \Psi}{\partial \bar{X}}\right)^2 + \left(\frac{\partial \Psi}{\partial \bar{Y}}\right)^2\right] \qquad \text{(V-3)}$$

$$\text{where } \bar{X} = \frac{X}{A_1} \qquad \bar{Y} = \frac{Y}{A_1}$$

Eq. (V-3) can be easily derived from Bernoulli's Equation

$$\frac{1}{2}\rho V_1^2 + P_1 = \frac{1}{2}\rho U^2 + P$$

and the definition of Ψ (Eq. (III-5)).

However, as will be shown below, numerical differentiation is a quite inaccurate process. Errors involved in numerical evaluation of C_p by Eq. (V-3) can be quite large. Thus, unless very fine grid size is used to obtain Ψ, accuracy to within the experimental uncertainty, i.e., about 0.01, cannot be obtained.

Calculation error in C_p can be estimated by the following expression

$$G = 2\left[\frac{\partial \Psi}{\partial \bar{X}} g_1 + \frac{\partial \Psi}{\partial \bar{Y}} g_2\right] \qquad \text{(V-4)}$$

G = absolute error of C_p

g_1 = absolute error $\frac{\partial \Psi}{\partial \bar{X}}$

g_2 = absolute error $\frac{\partial \Psi}{\partial \bar{Y}}$

Magnitudes of g_1 and g_2 depend on the formula used to evaluate the derivatives. For the central difference formula

$$\frac{\partial \Psi}{\partial X} = \frac{\Psi_{m+1,n} - \Psi_{m-1,n}}{2h} \qquad \text{(V-5)}$$

the error is $O(h/A_1)$ where h is the grid size. For forward or backward difference formula

$$\frac{\partial \Psi}{\partial \bar{X}} = \frac{\Psi_{m+1,n} - \Psi_{m,n}}{h} \quad \text{(forward)}$$

$$\frac{\partial \Psi}{\partial \bar{Y}} = \frac{\Psi_{m,n} - \Psi_{m,n-1}}{h} \quad \text{(backward)} \qquad \text{(V-6)}$$

the error is $O((h/A)^2)$.

To check the error that may occur if the numerical calculation of Ψ on page 52 is used to evaluate C_p , apply Eq. (V-4) at a point near the throat, for example (0.75", 0.64"). $\frac{\partial \Psi}{\partial \bar{Y}}$, $\frac{\partial \Psi}{\partial \bar{X}}$ are expected to be close to the experimental values .96 and .20 of u/V_1 and v/V_1 respectively. For the grid size of 1/2" in that example $h/A_1 \approx .352$. Hence if central difference formula Eq. (V-5) is used, g_1 and g_2 are of the order of $O(0.12)$; whence G evaluated by Eq. (V-4) would be of the order of $O(0.28)$, which is unacceptable.

To obtain a predicted value of C_p with uncertainty approximately equal to the experimental uncertainty of 0.01, grid size $h = 0.05"$ would probably be needed. But with this grid size, numerical calculation would involve approximately 15,500 equations derived from Eq. (V-2)!!

Moreover, since the values of Ψ outside the inviscid channel are unknown, to calculate C_p along the channel wall, Eq. (V-6) instead of Eq. (V-5) must be used to obtain derivatives. This would increase the size of error, and hence an even smaller grid size would be needed!

Therefore, to evaluate C_p to within acceptable accuracy by this procedure, not only quick calculation methods for solving a large linear system of equations of type Eq. (V-2) but also large and very high speed computers are needed.

E. Boundary Layer Calculation

The prediction of the growth of a turbulent boundary layer in adverse pressure gradient is, by itself, an interesting and complicated problem. Many calculation methods have been proposed by different investigators. Excellent up-to-date reviews in this subject can be found in Rotta [1962, 1965].

A few methods were applied to calculate the development of the boundary layer parameters on both side walls of the RC8 case with the experimental pressure distributions as input. Results will be discussed after the next section.

At separation, the boundary layer assumptions are not satisfied, and thus none of the existing methods work well beyond the separation point. Hence a criterion is needed to indicate where separation is expected.

E.1. Separation Criteria

To find a separation criterion is one of the basic difficulties in a separated flow study. A single universal one that is valid for all types of separated flow is still unavailable.

Extensive summaries of different criteria suggested by many investigators can be found in Reneau, et al [1965] and McDonald [1962]. Among them only the one suggested by Sandborn [1959]

$$H = 1 + \frac{1}{1 - \frac{\delta^*}{\delta}}$$

and those defined by a constant value of H are applicable to the present study.

Sandborn's criterion was applied to the profiles around the separation point and to the unstalled profile with highest shape factor, H, for all three flow field data presented in Chapters III and IV. As shown in fig. V-3, all these profiles satisfy this criterion. Moreover, Sandborn and Kline [1961] check this criterion against many other known turbulent boundary layer data around separation. It appears that at present this is the most generally successful one. The main difficulty in this criterion is that accurate values of all δ, δ^* and H are needed. In most cases, measurements or calculation of these quantities, especially δ, cannot be made with great accuracy.

Different constant H values were suggested by previous investigators as the criterion for turbulent boundary layer at separation (e.g., $1.8 \leq H \leq 2.4$ by Von Doenhoff and Tetervin [1943]; see Chapter 6, Reneau [1964] for others). Such values are tailored to their particular boundary layer calculation methods or experimental data.

In the proposed analytical model, it is not necessary to predict the <u>exact</u> location of the separation point. If a simple criterion can be found which guarantees separation to occur within a small interval, then the matching conditions of step 4 can be checked. Such simple criterion can be deduced as follows.

The table below repeats some boundary layer data tabulated in table 4.

		REF	RC8	TKD
Stalled Side	H at X=-0.5"	1.39	1.79	1.36
	H at X=0.5"	5.9	3.96	2.95
	Location of Separation Point	X=0"	X=0.25"	X=0.25"
Unstalled Side	Highest H value	2.0	1.99	1.93
	Corresponding Location	X=1.5"	X=4.53"	X=2.72"

From the above table, one can observe that a shape factor of 2.7 is higher than all the H of unstalled boundary layers measured in this experiment. Interpolating values of H in the table shows that H = 2.7 occurs within a small interval bounded by X = 0" and X = 0.5". Inside this interval separation in every case also takes place.

Hence if by a suitable boundary layer calculation method an H value of 2.7 is obtained at a location S^*, separation in all the present cases should be in the vicinity of S^*. H = 2.7 may then be taken as a computing criterion to terminate boundary layer calculations and begin to check matching conditions of step 4.

It must be emphasized that this shape factor H = 2.7 is <u>not</u> a separation criterion because it does not locate the exact separation position, and may not work well for flows going slowly to separation. It does, however, give the vicinity of separation when H rises sharply at separation as in these cases, and hence it is adequate as a "program stop."

This criterion is also valid for the breakaway type separation in the present channel since H jumps to 2.7 in a very short distance although its value may be under 2.0 at the breakaway separation point.

E.2. Several Turbulent Boundary Layer Prediction Methods[†]

Pressure distribution along the walls of the RC8 case (fig. IV-2) are applied to several turbulent boundary layer prediction methods supposedly valid for arbitrary pressure gradients to calculate the growth of δ^* and H along the two side walls. Initial conditions are taken to be the same as experimental data at the inlet point (X = -6", table 4-b). Results of four methods that represent different approaches are presented in fig. V-4 and V-5. The table below summarizes the methods. Complete equations can be found in Appendix D.

VD&T	Method by Von Doenhoff and Tetervin [1943] combining Von Karman's momentum equation and two empirical equations.
MIN4[‡]	Method combining Von Karman's momentum equation, energy integral equation with Clauser's eddy viscosity and asymptotic matching of the law of the wall and law of the wake.
MIN6[‡]	Method combining Von Karman's momentum equation, energy integral equation with Truckenbrodt's dissipation integral and asymptotic matching of the law of the wall and the law of the wake.
M2N1[‡]	Method combining Von Karman's momentum equation, entrainment equation, turbulent kinetic energy model equation and asymptotic matching of the law of the wall and the law of the wake.

---

† Calculations in this section are due to Mr. E. Hirst.

‡ These methods are proposed and will be reported subsequently by E. Hirst and W. C. Reynolds, Stanford University.

As shown in figs. V-4 and V-5, the trends of change in δ^* and H can be predicted for both the stalled and unstalled wall. Calculated values also match with experimental results fairly well when the flow is accelerating and the pressure gradient is mild. But around the throat section where the change in free stream velocity is sharp, deviations are observed. In addition, none of the prediction methods can pass an H value of higher than 1.5 under such sharp pressure changes. Solutions become unstable and oscillate at S = 2" on the unstalled wall and S = -3/4" on the stalled wall. At these locations measured H also shows sharp increase in values (see table 4-b).

Since these four methods represent most of the common approaches to turbulent boundary layer prediction, it may be concluded that the growth of δ^* and H cannot be calculated accurately with existing two-dimensional boundary layer equations in Cartesian coordinates when the pressure gradient is as sharp as those measured in the present study. Pressure gradient normal to the wall exists in measurements on the unstalled side. This may cause the failure of the prediction methods on this side. On the stalled side, the rise in pressure is so sudden that boundary layer assumptions break down before the separation point is approached.

Hence to complete the iteration cycle in the present proposed method for establishing the stable separation phenomenon, more work has to be done to improve boundary layer calculations for use when high pressure gradients occur.

F. Matching Conditions

Two conditions must be satisfied when the boundary layer calculations and the inviscid calculations converge.

1. At all positions where the calculated $H \leq 2.7$, δ^* must match the local boundary of the assumed effective channel to within a specified small allowance.

2. If separation is approached in boundary layer calculation, i.e., δ^* exists where $H = 2.7$, then at any $S \geq S^*$ on the same side of the channel.

$$\left| \frac{C_p(S) - C_p(S'')}{C_p(S)} \right| \leq 5\%$$

The first condition is simply from the definition of the effective channel. The second condition comes from the conclusion that along the displacement line Y_{δ}^*, variation of C_p should be very small (see page 47).

If at any iterative step either of the above conditions is not satisfied, a new effective channel can be formed by lines which cut the gaps between previous channel and previously calculated displacement thickness. Then all steps must be repeated for the next iteration.

G. Initializing the Computation

To start the iterative scheme, the complete physical channel should be taken as the effective channel. Qualitative C_p distribution on the two side walls would be like that shown in sketch (g). With this C_p distribution, boundary layer computation can be done. If no separation is predicted, the channel is unstalled. Results of calculations for unstalled diffusers can be found in Cocanower, et al [1965], Reneau et al [1964], Sovran and Klomp [1967].

If separation is predicted on either side, say at S', then assume that the next pattern is the two-dimensional fully-stalled configuration. In this configuration separation point must be very near the throat. Otherwise, a strong stagnation point will occur changing the pressure curves to those shown in sketch (h). The stronger pressure rise at the stagnation point will then move separation point further upstream.

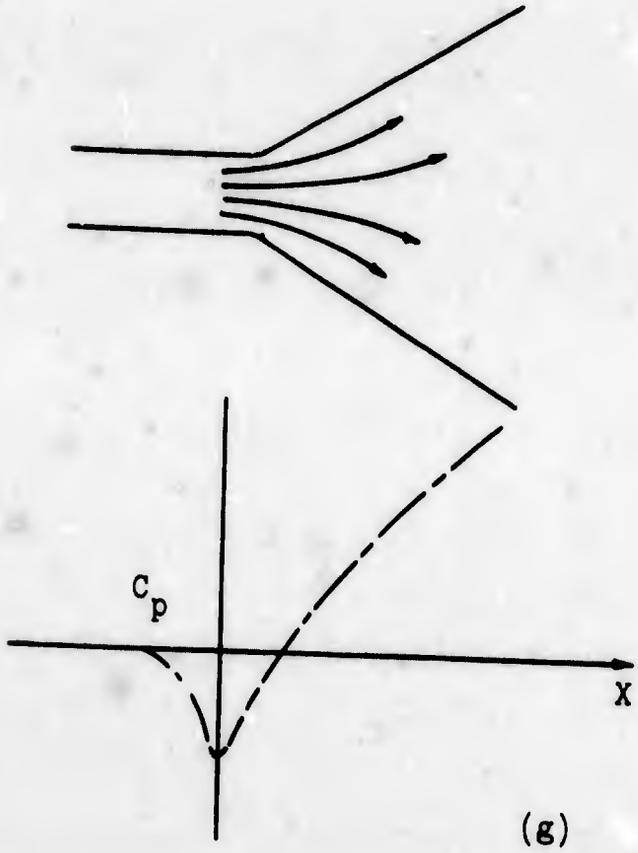

(g)

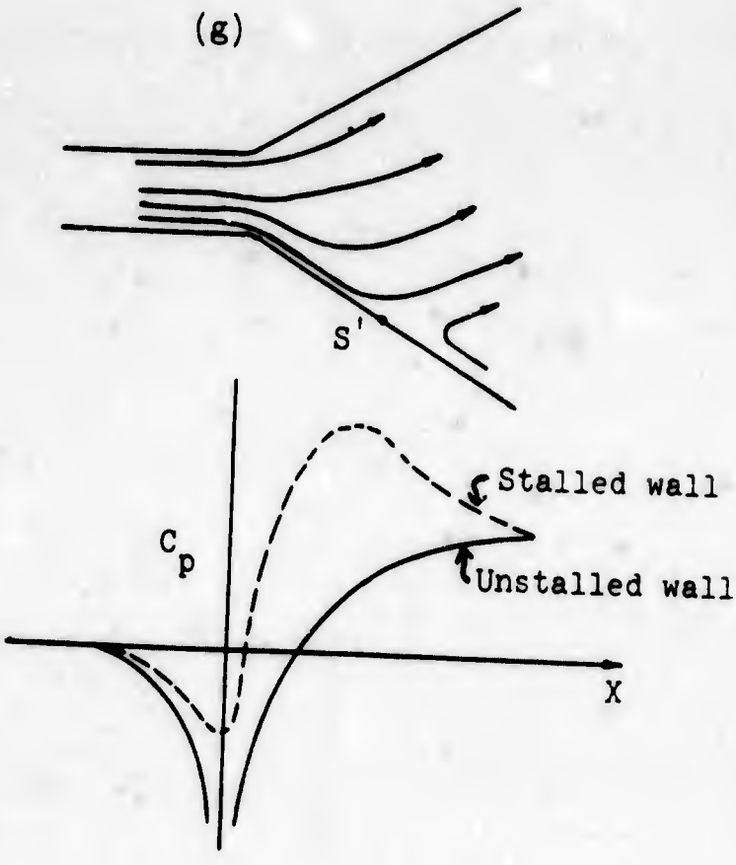

(h)

In the two-dimensional fully stalled configuration, the displacement line Y_δ^* must eventually become a straight segment parallel to the unstalled wall. If this straight segment is extended backward, it must intersect the stalled wall at a point downstream of the throat in order to have a positive C_p at the exit. The limiting position of this line is restricted by the condition that the final area, A_2, must be bigger than inlet area, A_1.

If the two-dimensional stalled pattern is assumed in a channel with too large a divergent angle θ, pressure rise after the throat will be so sharp on the unstalled wall that separation could also be predicted on this side wall by boundary layer calculation. Then the jet flow pattern should be expected. Separation points in the jet flow configuration would also be near the throat for the same reason mentioned two paragraphs above.

Chapter VI

SUMMARY AND CONCLUSION

1. The fully stalled flow in the present study is established by the stable balance of the shape of the effective channel, the vastly altered pressure field associated with the effective channel, and the growth of the boundary layers on the two side walls. Interactions among these elements occur as follows:

Since the locus of the displacement thickness of the boundary layer on the unstalled wall forms one boundary of the effective channel, growth of the unstalled boundary layer defines the effective channel shape on the unstalled side. The boundary layer on the stalled side affects the shape of the effective channel in two ways. First, the locus of the displacement thickness before separation is the boundary of the effective channel up to the separation point. Second, beyond the separation point, the channel is bounded by the displacement line, which in turn is affected by the location of the separation point and the boundary layer profile just before separation.

For all cases investigated, the shape of the effective channel defines the shapes of the streamlines in the main flow. Qualitatively, pressure distribution both inside the channel and along the side walls can be explained by applying Euler's equations to the streamline pattern in the effective channel. Quantitatively, one-dimensional ideal calculation applied to this channel gives a good estimate for the final pressure recovery coefficient. The blockage effects of boundary layers and the free shear layer are important in this estimate; if these effects are neglected, and estimates of C_p based on an inviscid channel bounded by the solid walls and the dividing streamline, calculated overall recoveries differ from experimental values almost by a factor of two.

The following tables summarize these estimates.

Case	C_{pe} via Effective Channel	Uncertainty in Estimation	Exper. C_{pe}	Experimental Uncertainty	C_{pe} via Dividing Streamline Neglecting δ^* Effects
REF	0.25	0.04	0.22	0.01	0.41
RC8	0.33	0.04	0.34	0.01	0.46
TKD	0.26	0.04	0.20	0.01	0.43

The development of the boundary layers on the side walls is strongly affected by the pressure distribution along the walls. On the stalled side, separation occurs just after an abrupt pressure rise ahead of the throat. On the unstalled side, an equally steep positive pressure gradient does not cause separation, probably because momentum is added to the boundary layer by the strong negative pressure gradient in front of the throat. Nevertheless, downstream of the throat, the shape factor, H , of the unstalled boundary layer can become as high as 2.0 and the profile shows a distinct inflection.

2. All major changes in recovery occur within a region bounded by 2W up and downstream of the throat in the main stream. Downstream of the separation point, in the stalled flow region and along the displacement line, C_p is almost constant.

From the ratios of the magnitudes of velocities in the stalled flow to those in the main flow it is concluded that $C_p \approx$ constant is a necessary condition which the displacement line in any separated flow should satisfy. This conclusion also leads to an explanation why only three stable flow fully stalled configurations have been observed in diffusers without a tail pipe.

3. In all cases, the separation point occurs within half an inch downstream of the throat.

Case	Location of Separation Point X"	Y"
REF	0.0	- 1.50
RC8	0.25	- 1.76
TKD	0.25	- 1.62

All the boundary layer profiles measured obey the Sandborn [1959] separation criterion: $H = 1 + \frac{1}{1 - \frac{\delta^*}{\delta}}$. Moreover, interpolation of experimental H values lead to the conclusion that separation is so sharp that a simple criterion, $H = 2.7$, would define the actual separation point to within $\pm$ 1/4" from the actual separation point in all the cases observed. Thus, $H = 2.7$ is proposed as a simple criterion for terminating boundary layer calculations in this type of flow.

4. Based on the above conclusions, an analytical model has been proposed that would predict not only the stable two-dimensional fully stalled configuration but also the unstalled and jet flow configurations in diffusers. Owing to lack of time in the present program, this problem is not solved, but suggestions are made for follow-up studies. As a check on the validity of part of the calculation procedures, a potential flow solution has been obtained for the experimental effective channel in the RC8 field. The calculated streamline pattern checks well with the experimental one. Boundary layer calculations by methods of other investigators and based on experimental pressure distributions show the same trends for the growth of δ^* and H as the measured values, but the methods are inaccurate in the throat region where very rapid changes in pressure gradient occur.

5. When the parameters are changed from the REF case to RC8 and TKD cases, the flow data show some sensitivity, but most of the flow features alter only slightly. However, change of curvature at the throat affects pressure recovery coefficient in the flow field appreciably. This differs from the flow in unstalled diffuser as reported by Copp [1951]. In a fully stalled flow, each flow field "creates its own effective channel." The area ratio of the effective channel in the RC8 case is larger than both the REF and the TKD cases so that better final pressure recovery is obtained.

Other brief experimental results include effects of turbulent mixing on the pressure distributions along the walls of REF field. Some changes are observed, but more systematic studies including turbulence measurements will be needed to obtain final conclusions. Variation in Reynolds number from 2.5×10^5 to 1.4×10^5, based on inlet width and continuity velocity, does not affect the pressure coefficient along the side walls.

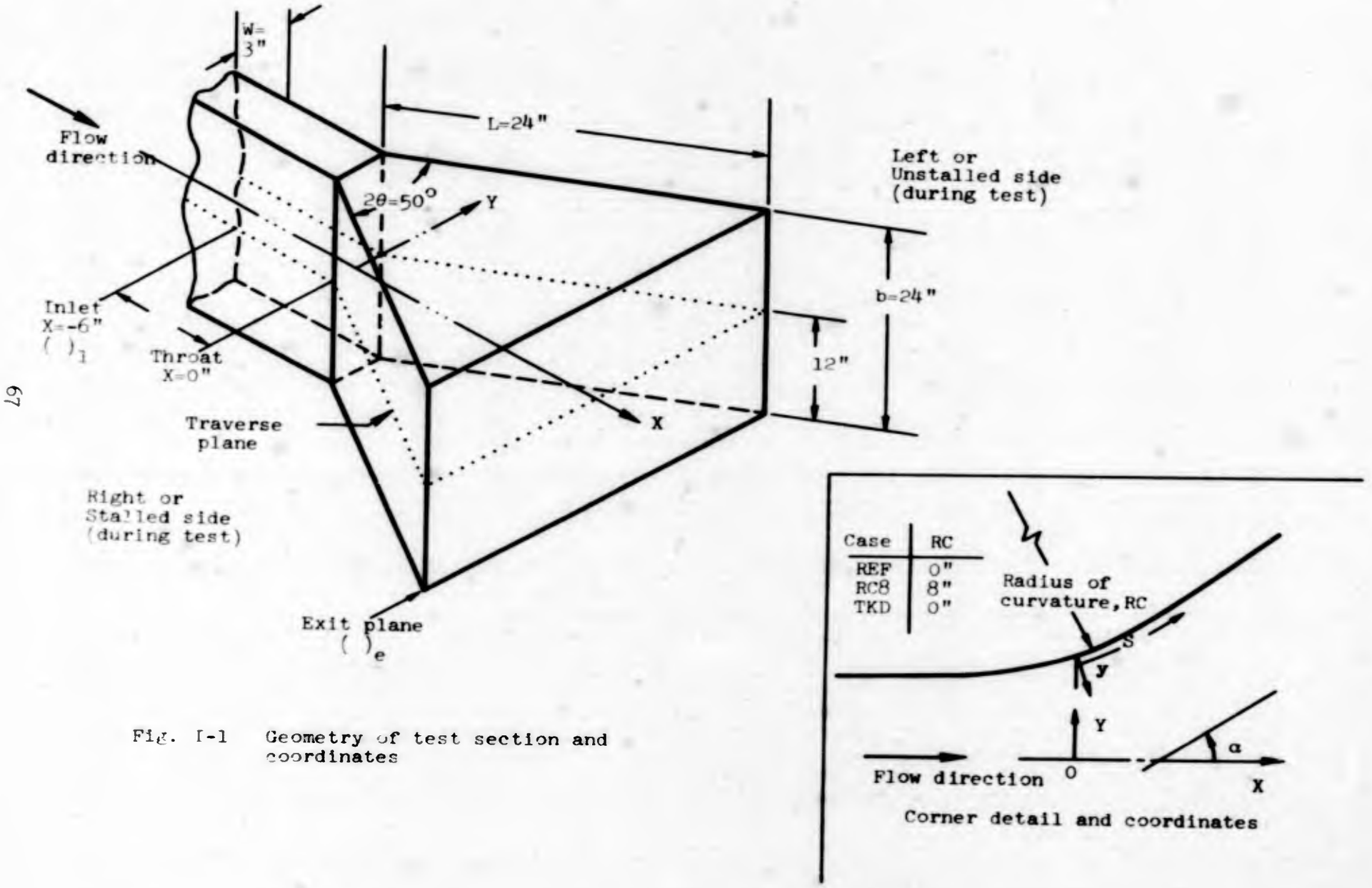

Fig. I-1 Geometry of test section and coordinates

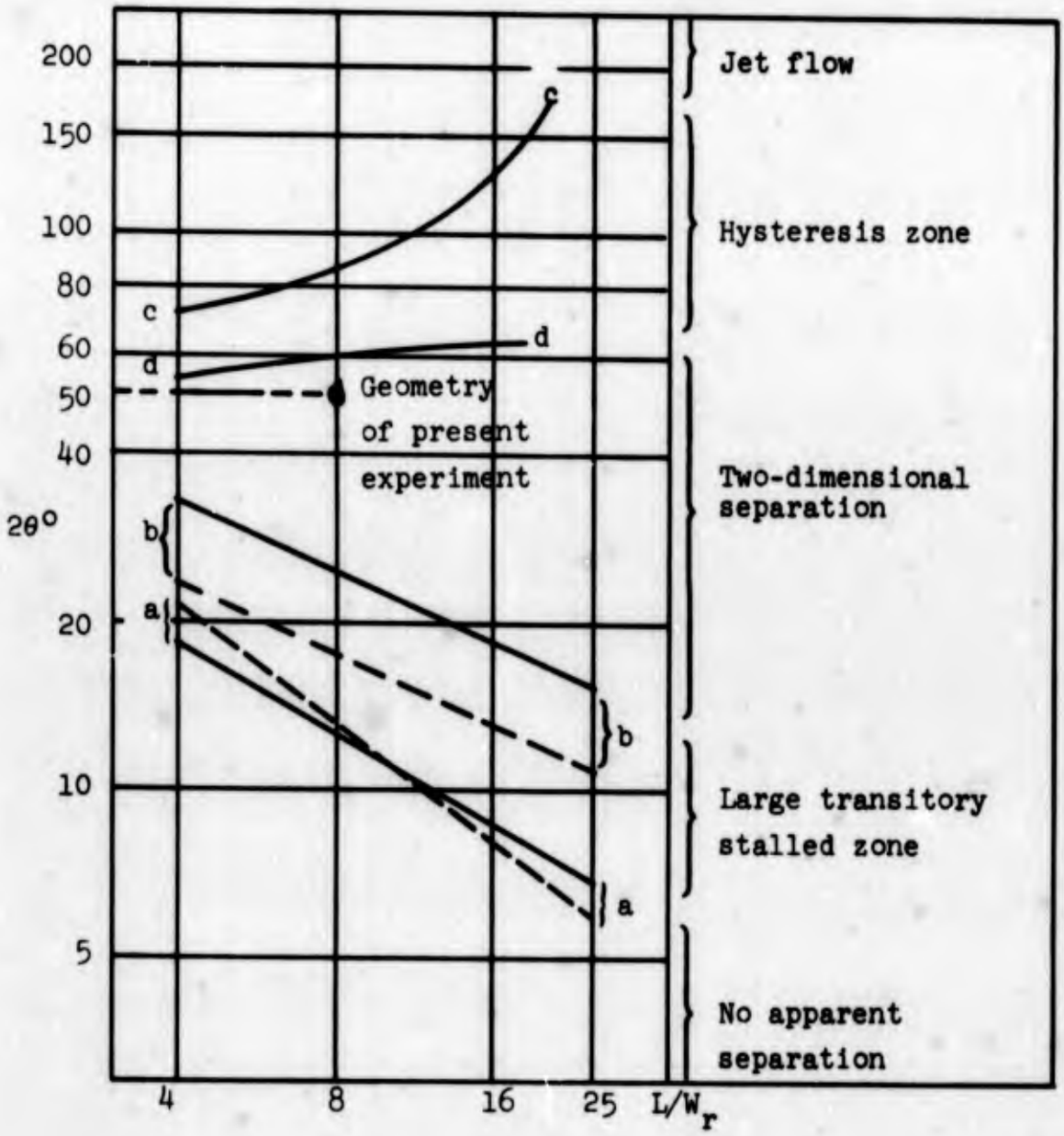

Fig. I-2 Flow regimes in diffusers

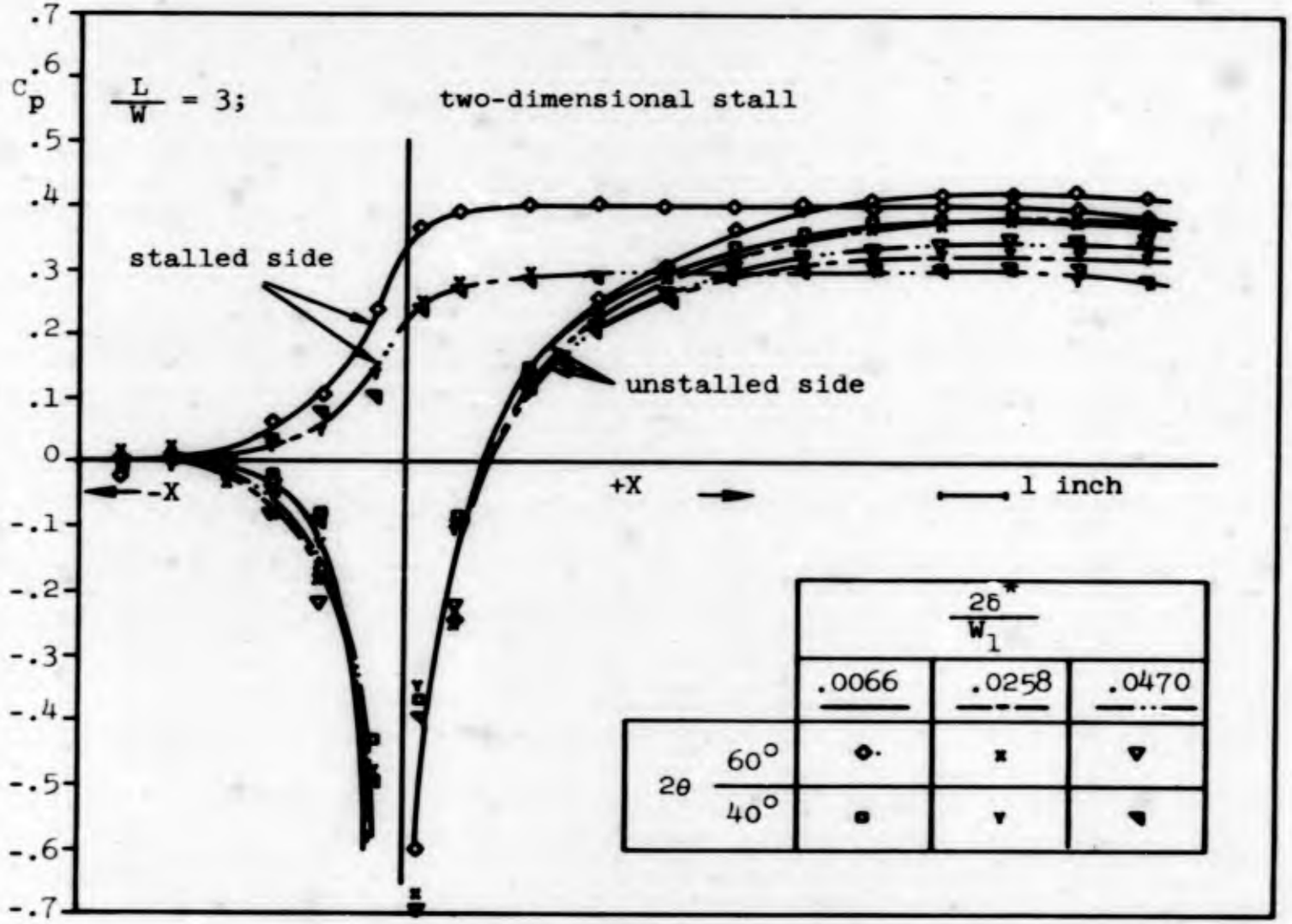

Fig. I-3 Pressure distribution for vaneless diffusers, two-dimensional stall. Feil [1962]

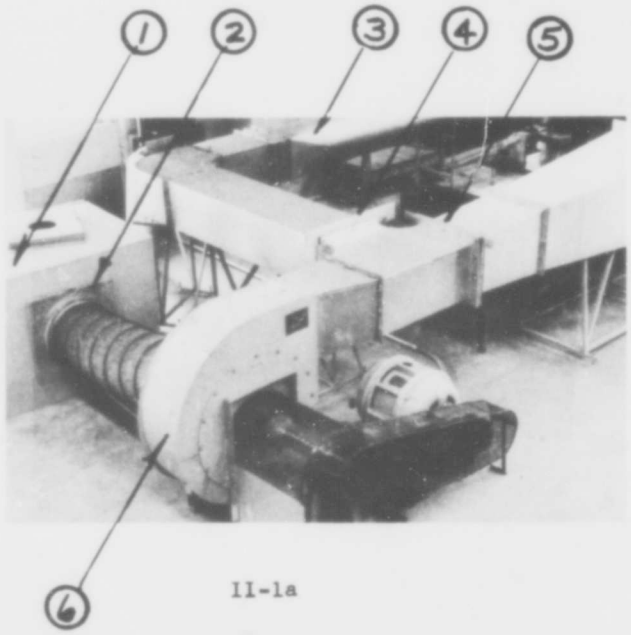

II-1a

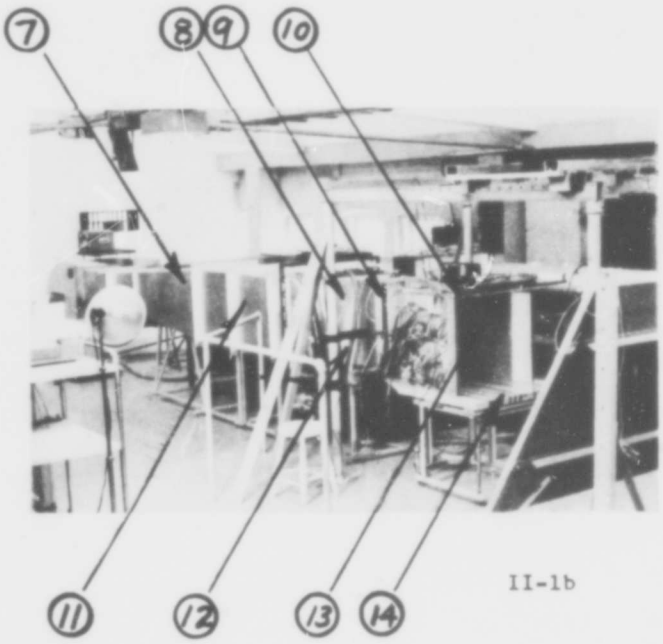

II-1b

1) Filter box 3' X 5' (Scott foam dust filters).

2) Speed control gate.

3) Second wind tunnel (Sagi 1965).

4) Blank off board.

5) Gate.

6) Blower (variable speed drive).

7) 2 way divergent duct.

8) Nozzle.

9) Plexiglas section.

10) Test section.

11) Flow straightener section.

12) Suction ducts.

13) Side wall

14) Sugar pine base board

Fig. II-1 Wind Tunnel

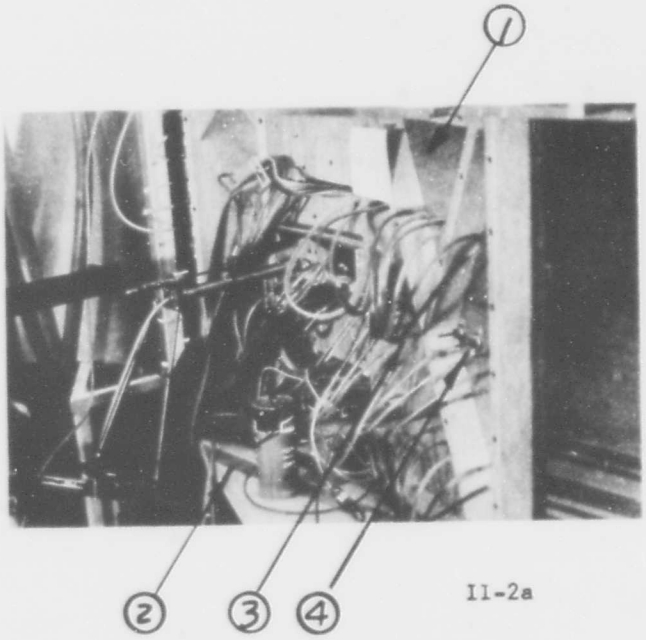

1) Side wall.

2) Surface board.

3) Wall pressure taps.

4) Wall probe holes.

5) Interchangable throat section.

6) Sliders

7) Clamps.

II-2a

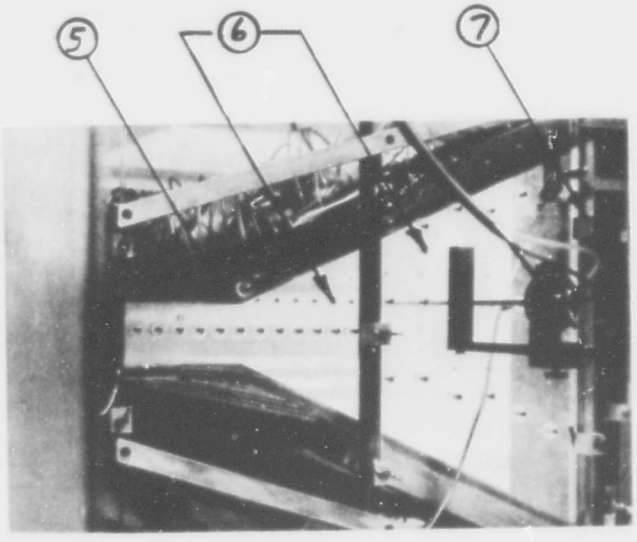

II-2b

Fig. II-2 Test Section

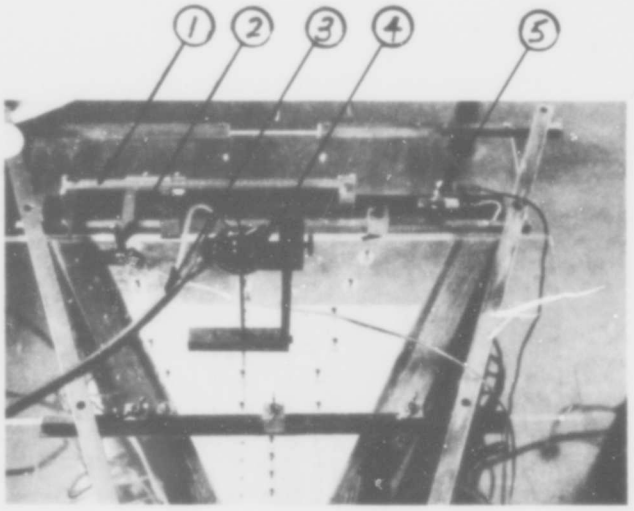

II-3a

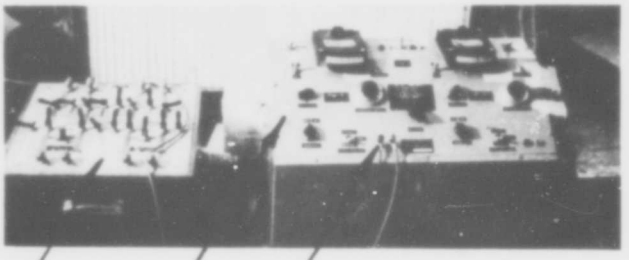

II-3b

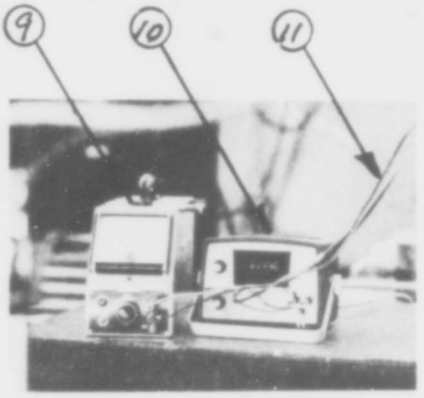

II-3c

1) Micro vernier caliper.

2) Contact rod.

3) Tubes leading to pressure transducers.

4) Probe holder with protractor.

5) Contact light.

6) Pressure transducer box.

7) Transducer circuit box.

8) Output of transducer.

9) Galvanometer.

10) Potentiometer (digitec).

11) From output of transducer.

Fig. II-3 Instruments

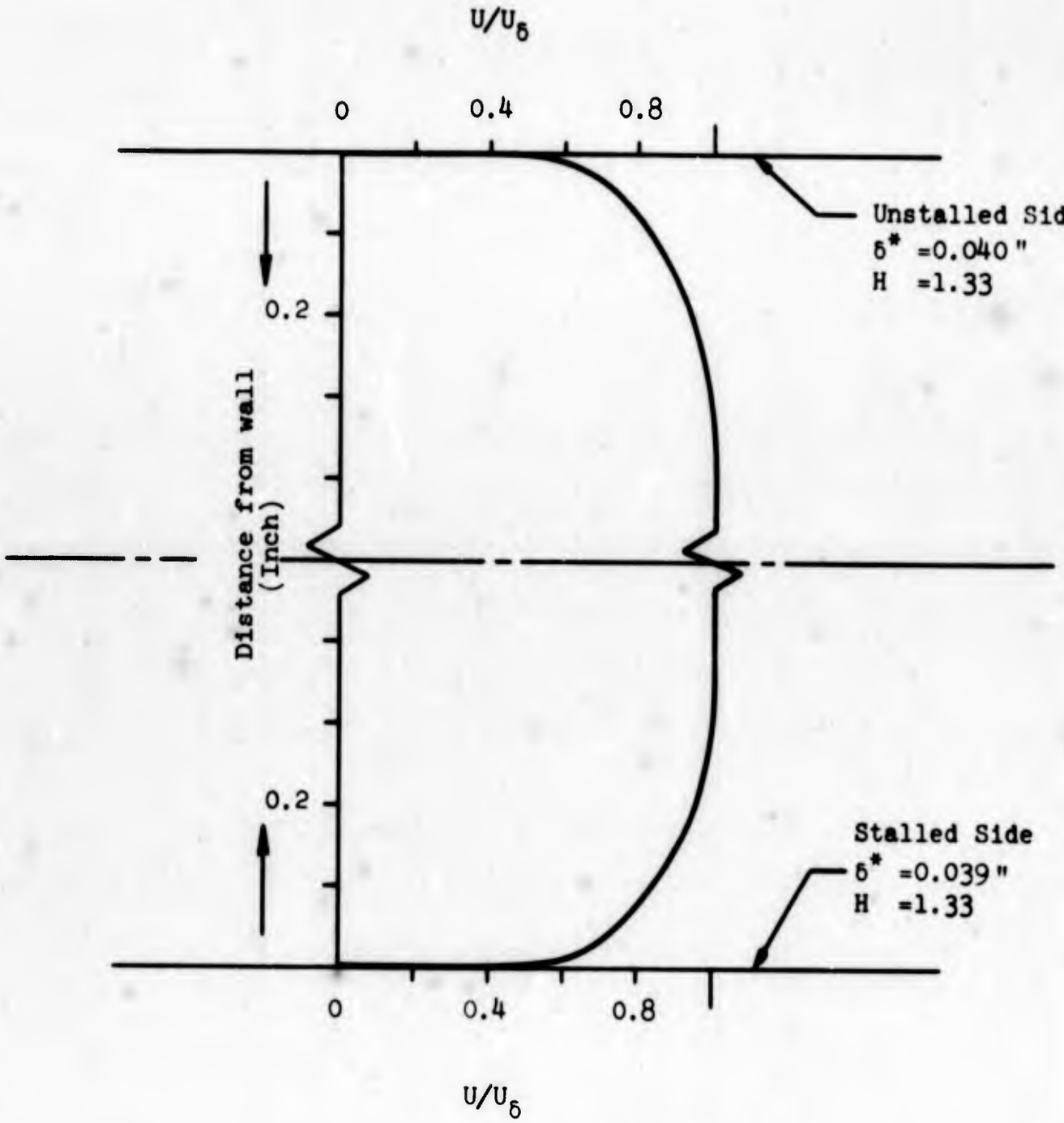

Fig. III-1 Velocity profile at inlet, X=-6" for REF and RC8 fields

1. $B = 1 - \dfrac{P_{T\infty_1} - P_T(X,Y)}{q_1}$

2. ● referenced to solid base line

   o referenced to dashed base line

3. Positive B on right and negative B on left of respective base line

4. B values laid out normal to base lines at all points

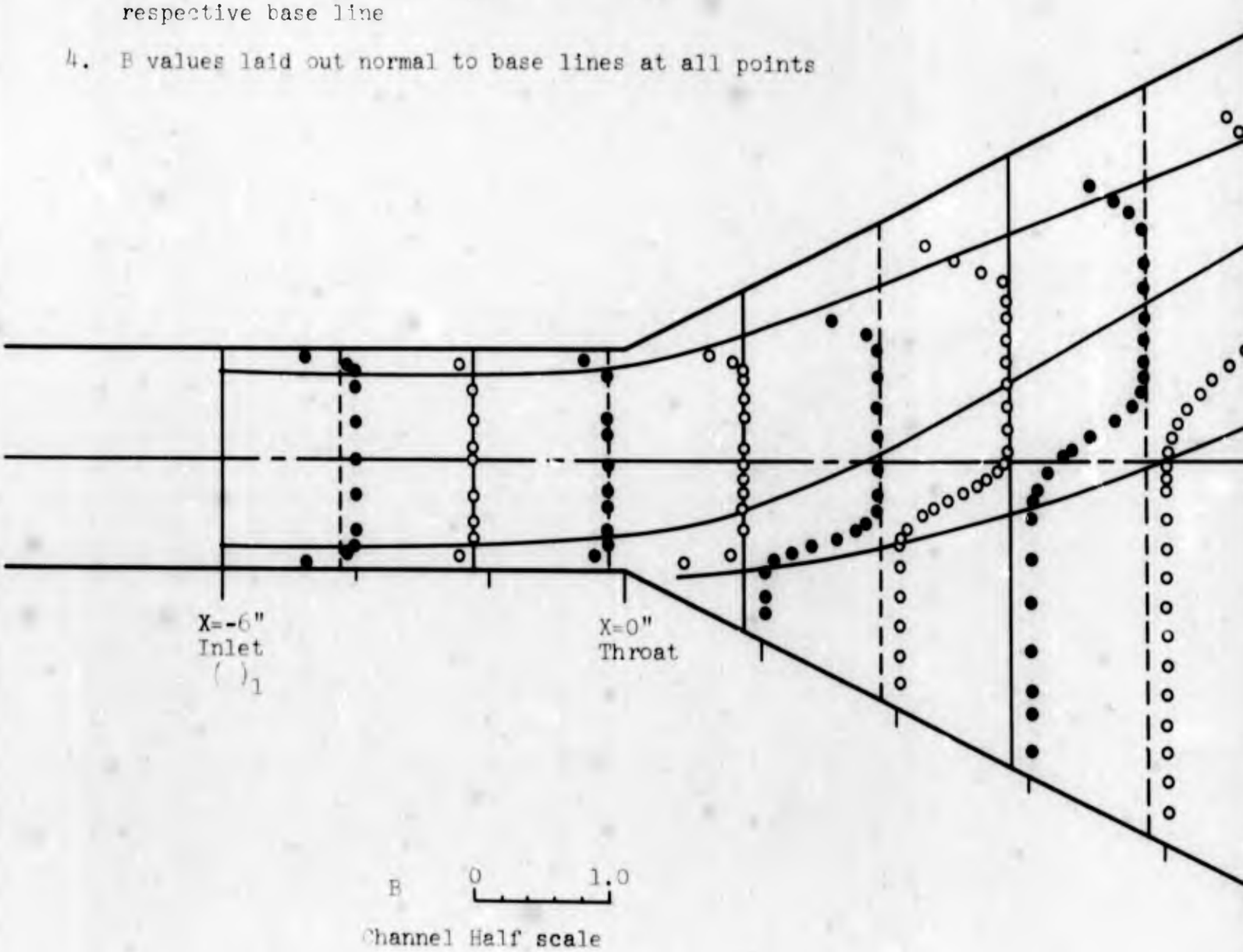

Fig. III-2 Local Bernoulli number, B, for reference flow f

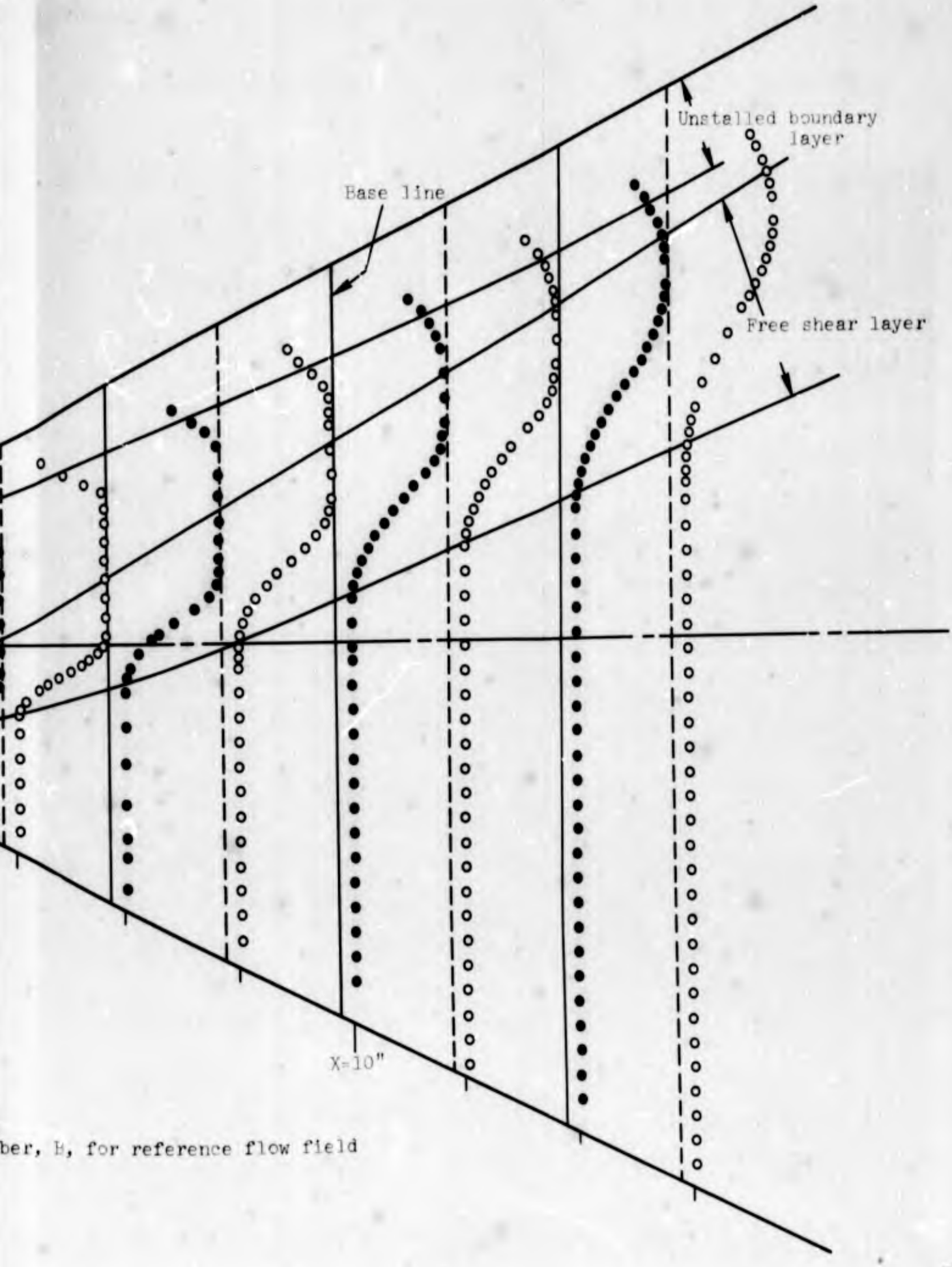

ber, E, for reference flow field

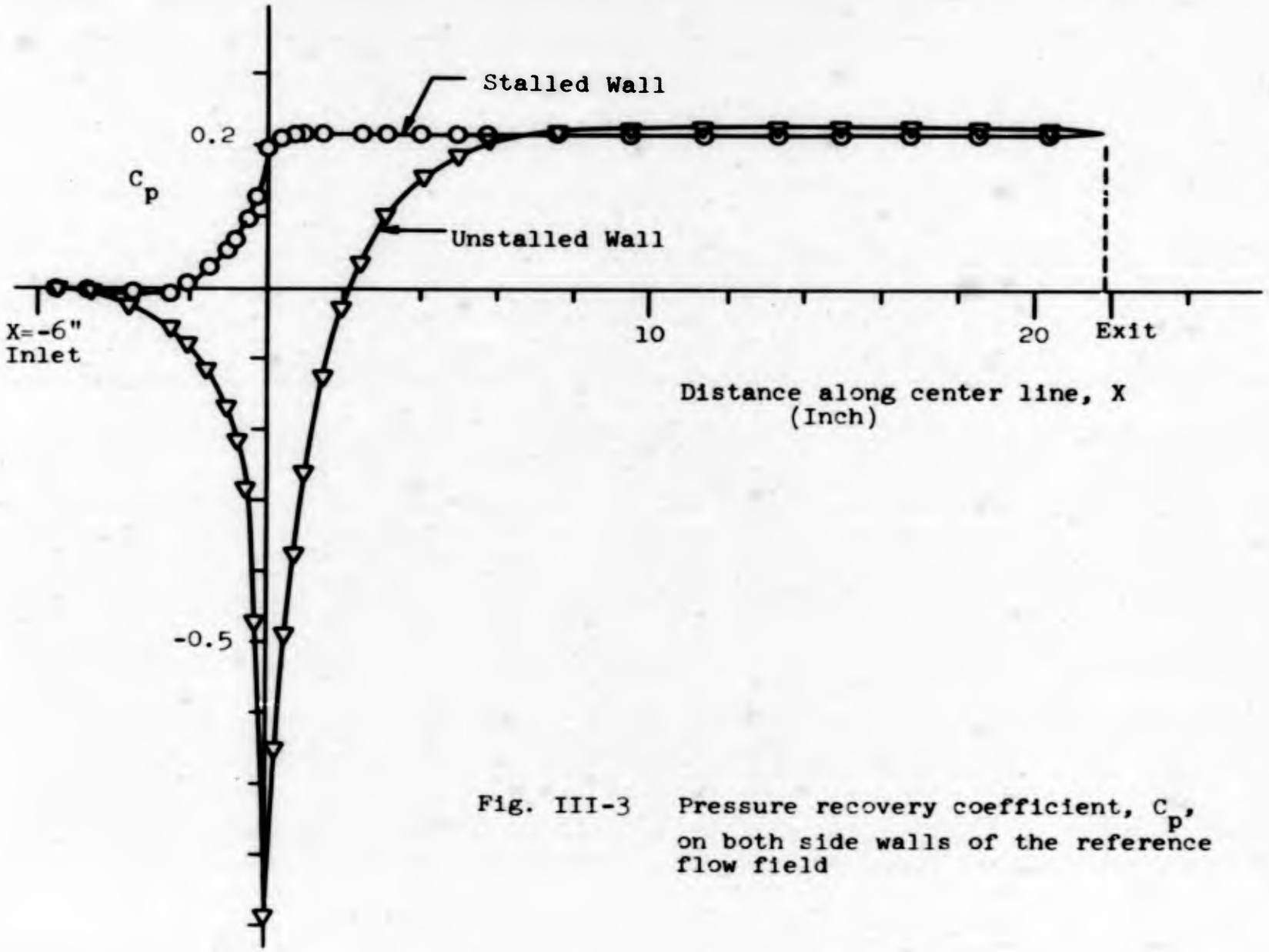

Fig. III-3 Pressure recovery coefficient, C_p, on both side walls of the reference flow field

BLANK PAGE

Note:

1. $C_p = \dfrac{P(X,Y) - P_1}{q_1}$

2. Solid symbols are referenced to solid base lines.
   Open symbols are referenced to dashed base lines.

3. Positive C_p on right and negative C_p on left of respective base line.

4. C_p values laid out normal to base line at all points.

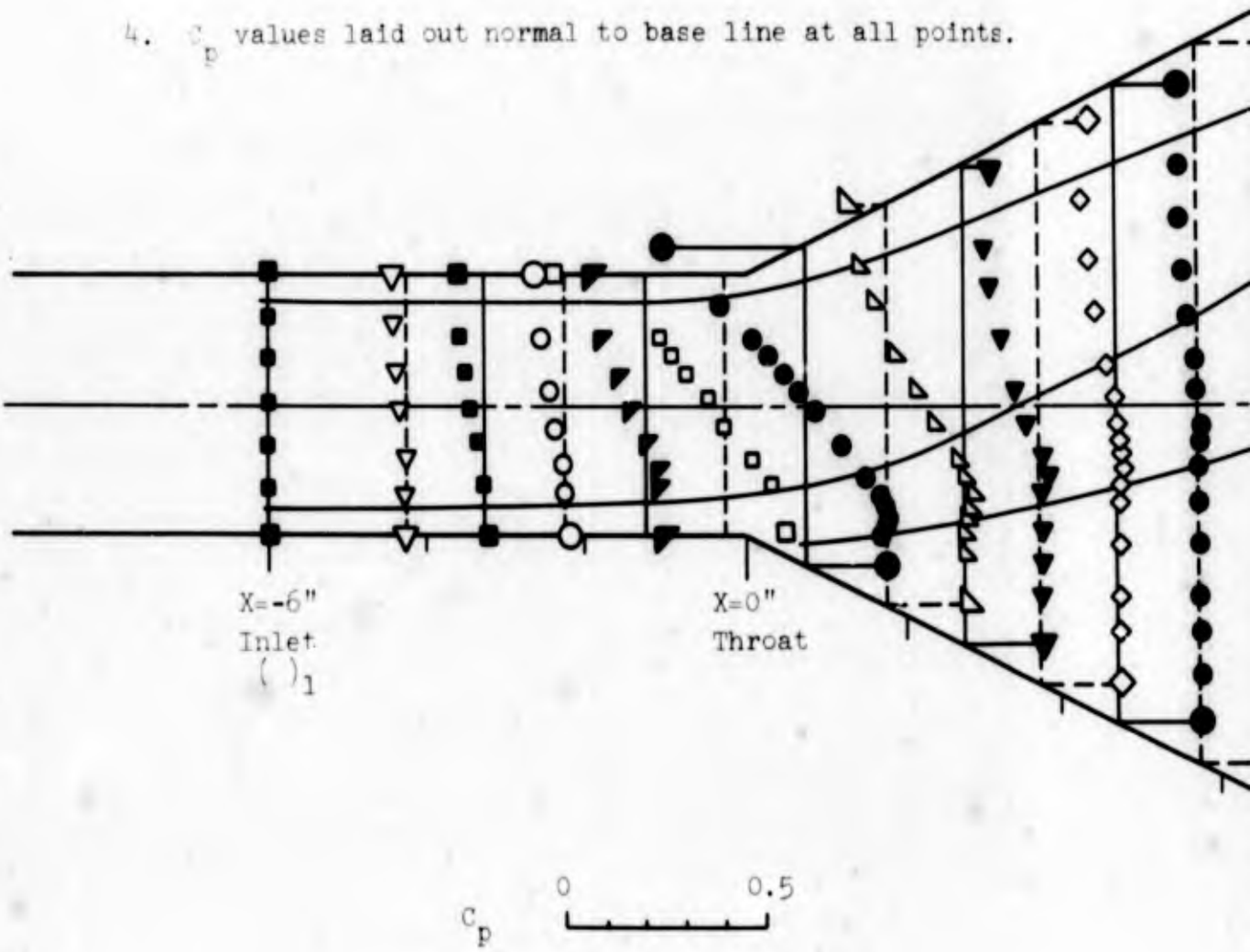

Channel Half scale

Fig. III-4 Local pressure coefficient, C_p, for reference

ints.

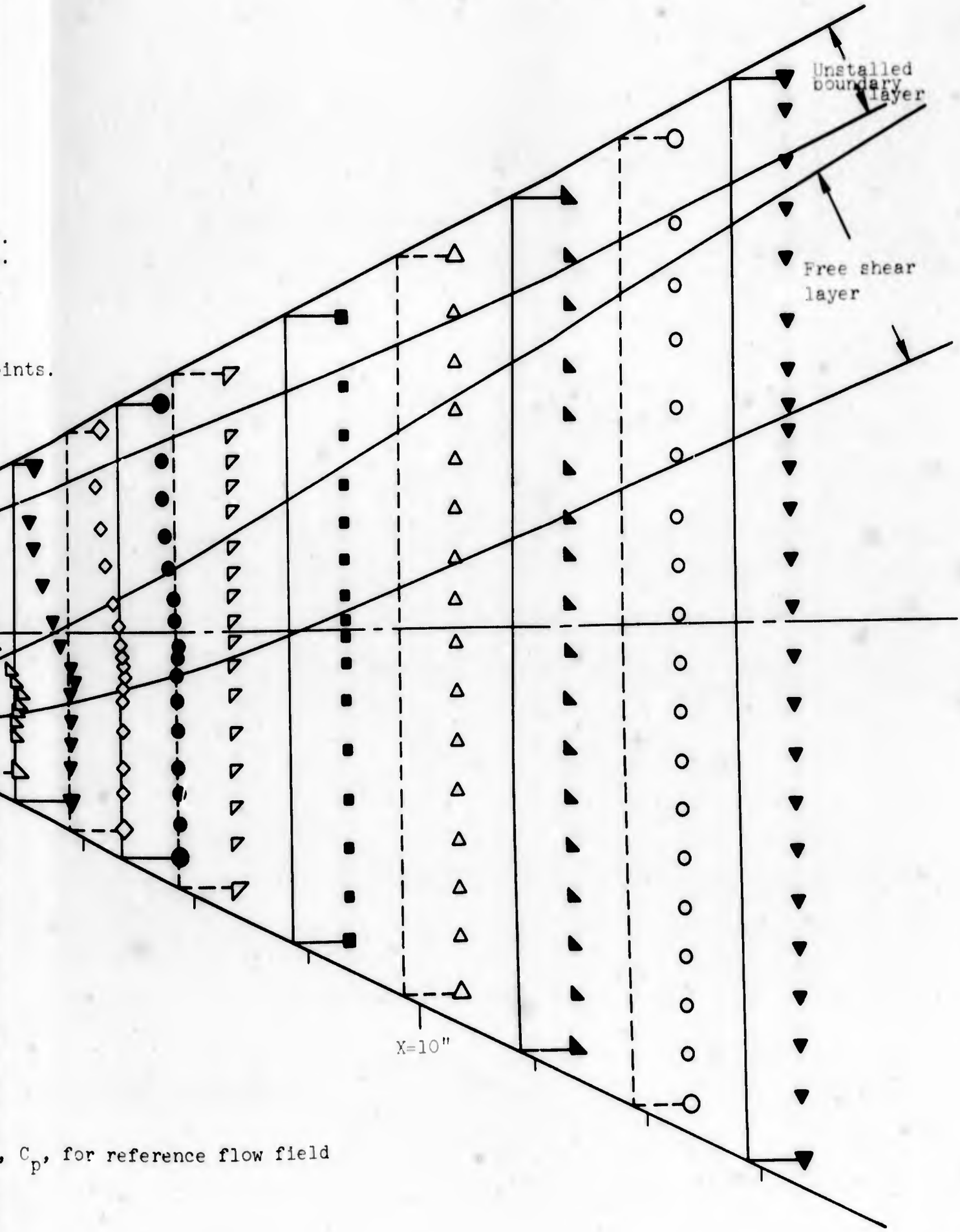

, C_p, for reference flow field

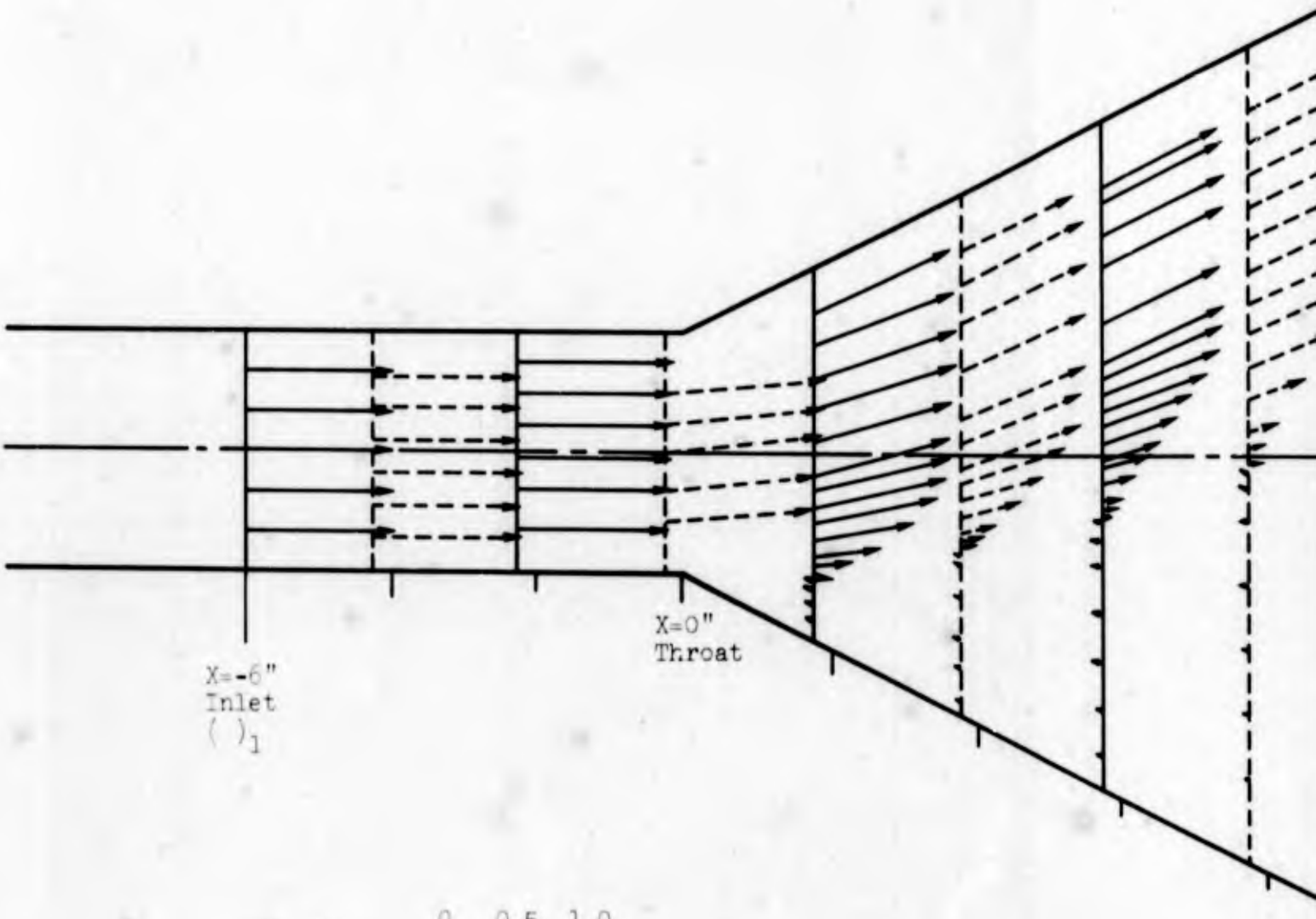

Fig. III-5 Distribution of local velocity/inlet ave
U/V_1 in the reference flow field

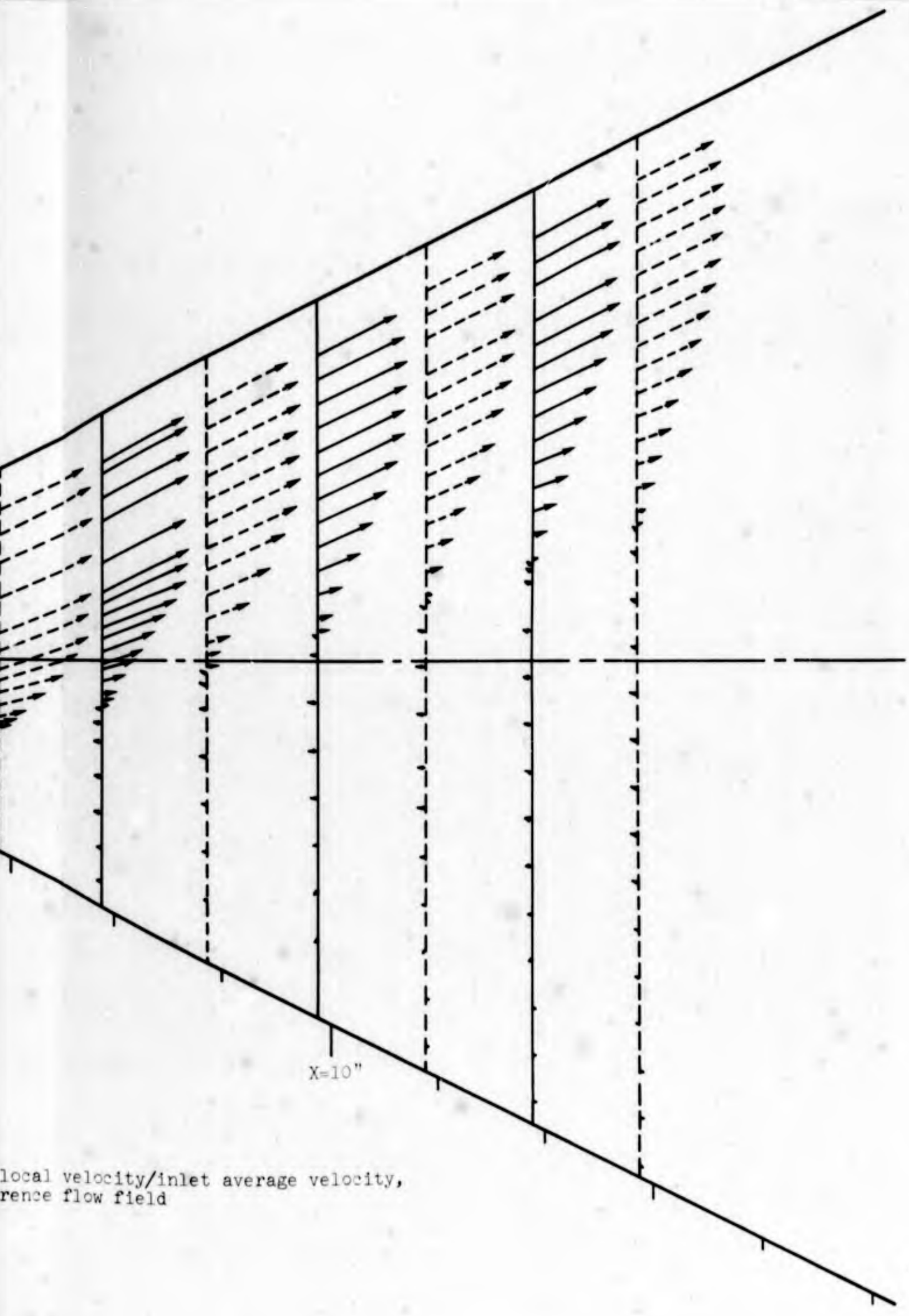

local velocity/inlet average velocity,
rence flow field

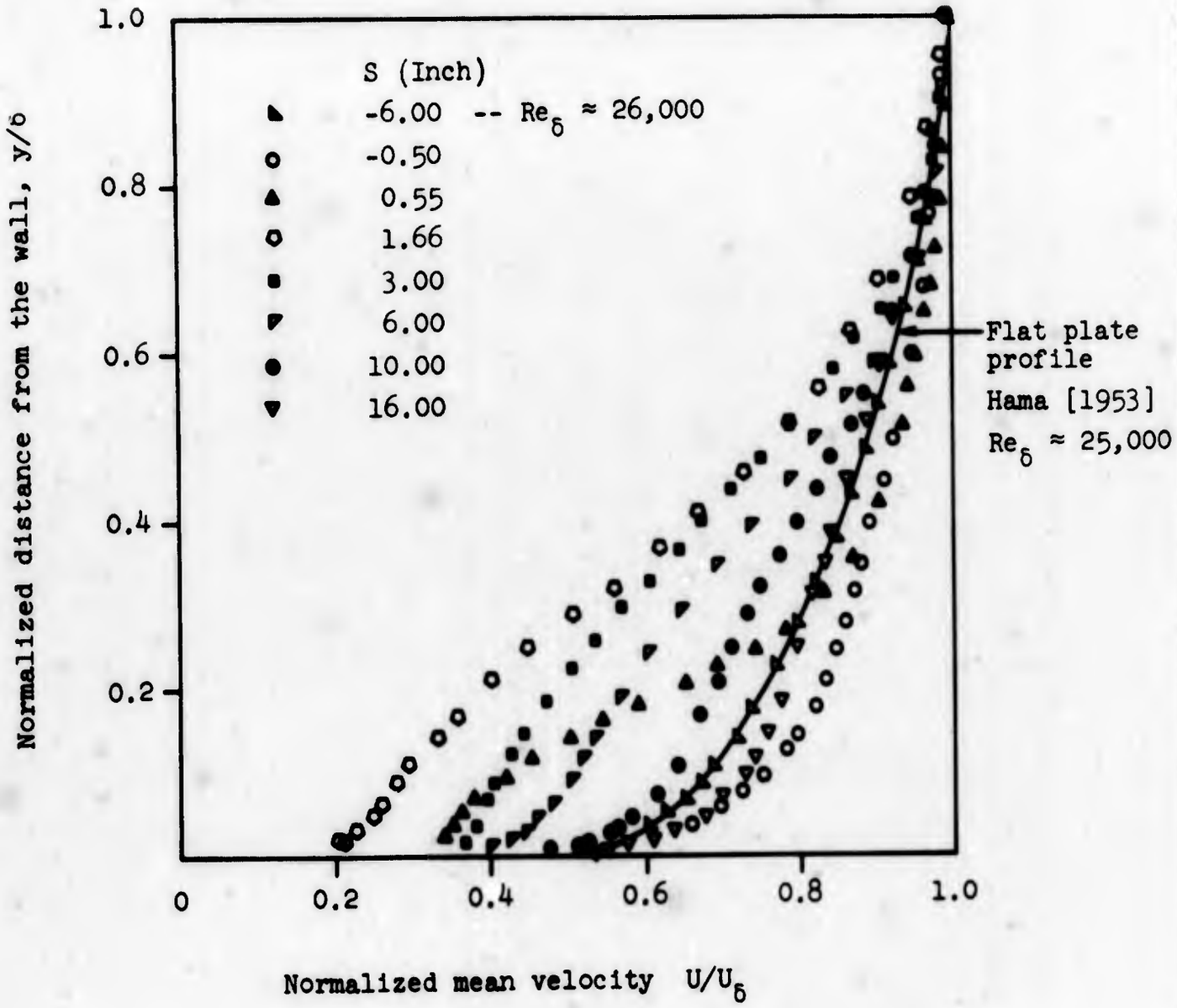

Fig. III-6 Boundary layer profiles along unstalled wall for REF flow

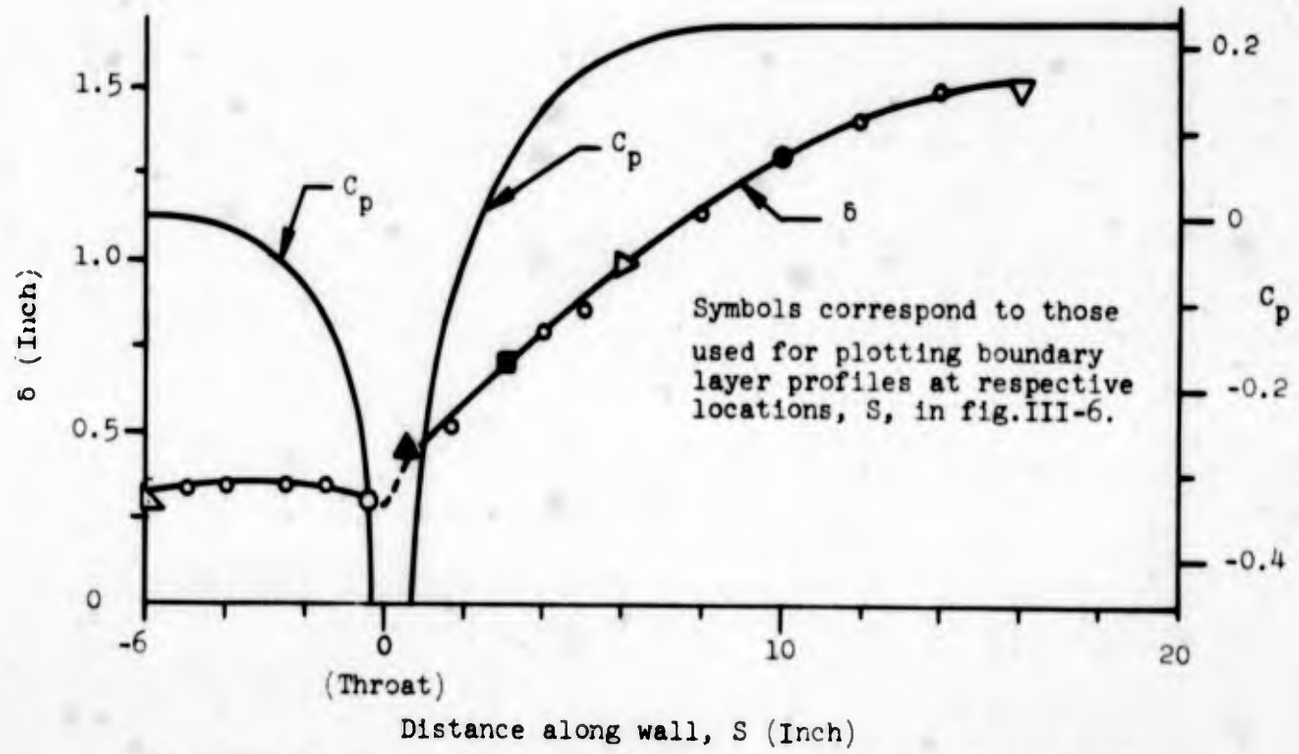

Fig. III-7a Boundary layer thickness on unstalled wall for REF flow

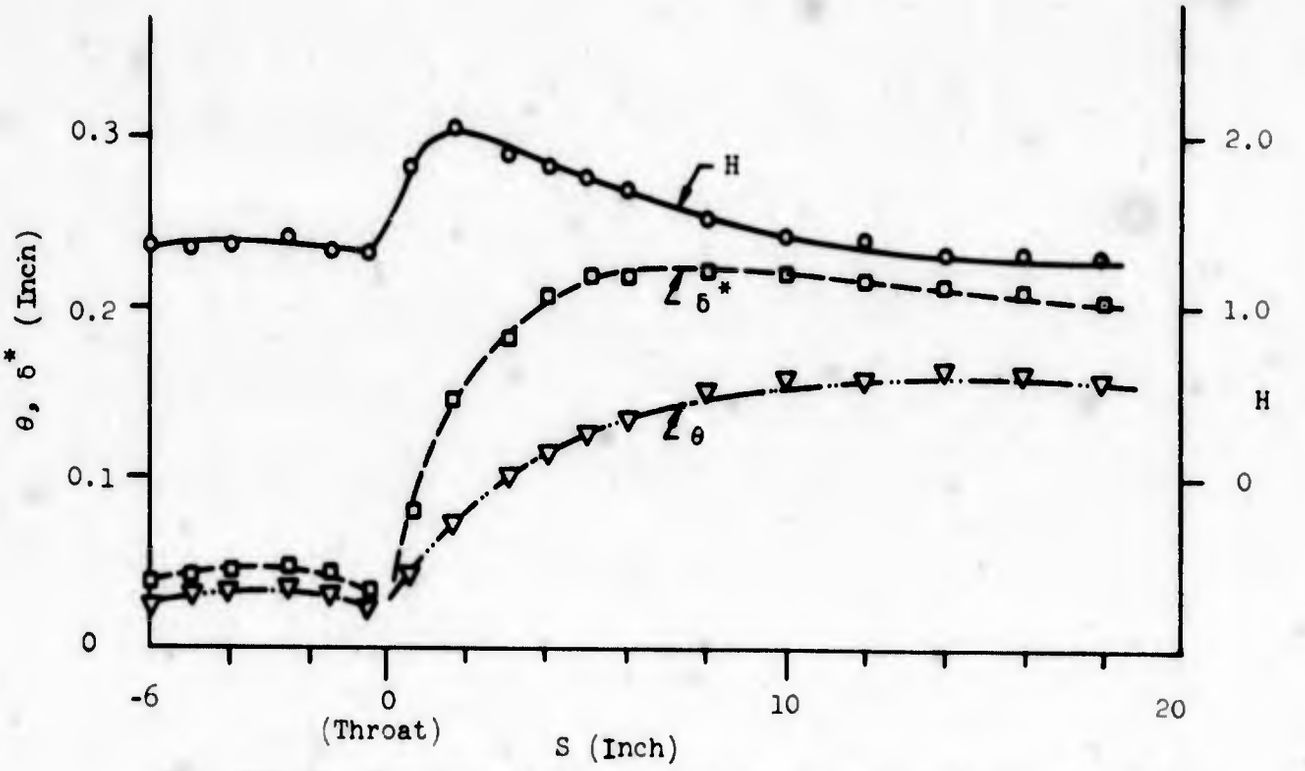

Fig. III-7b Boundary layer parameters on unstalled wall for REF flow

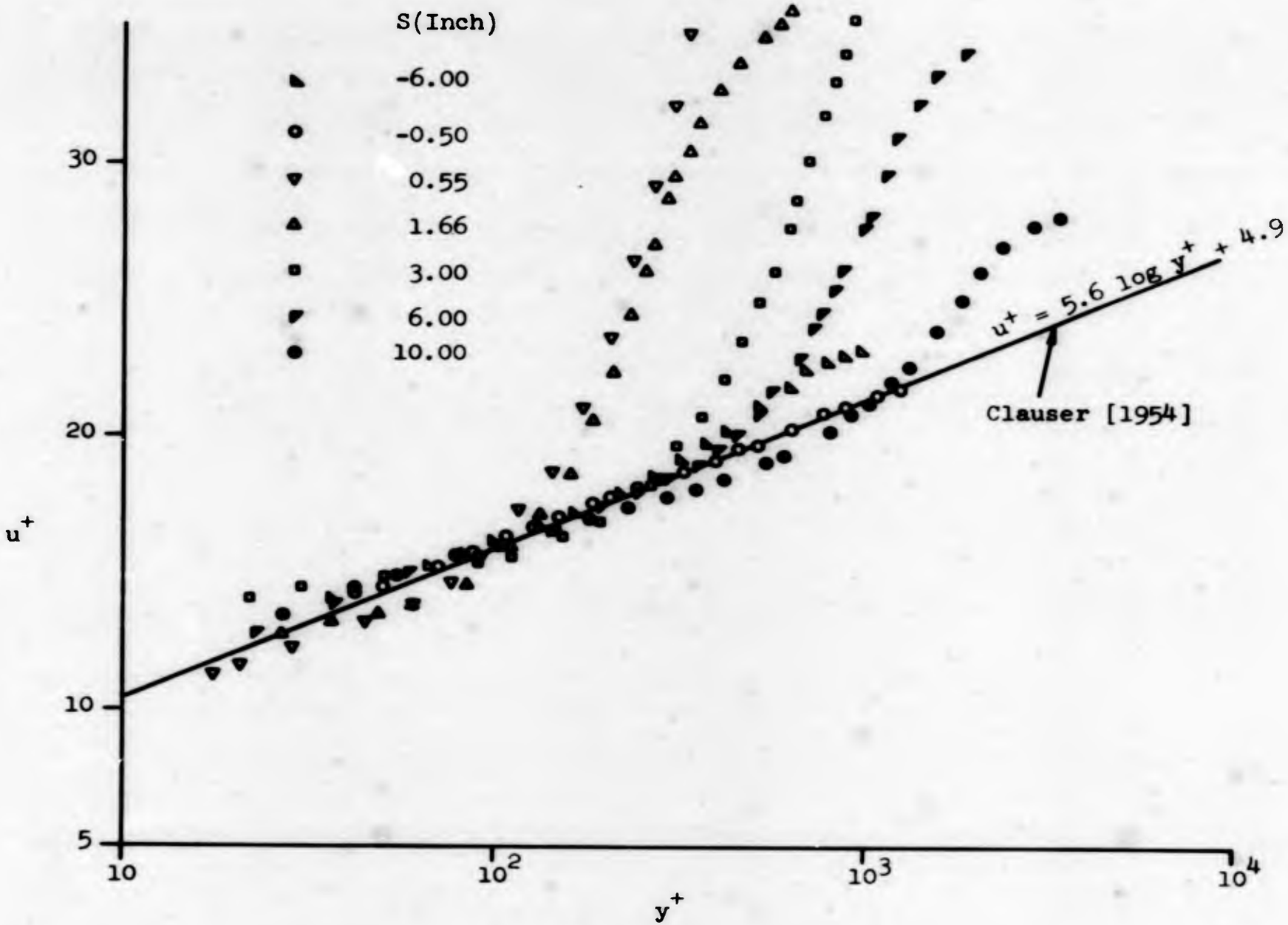

Fig. III-8 Cross plot of unstalled side boundary layers in reference flow field

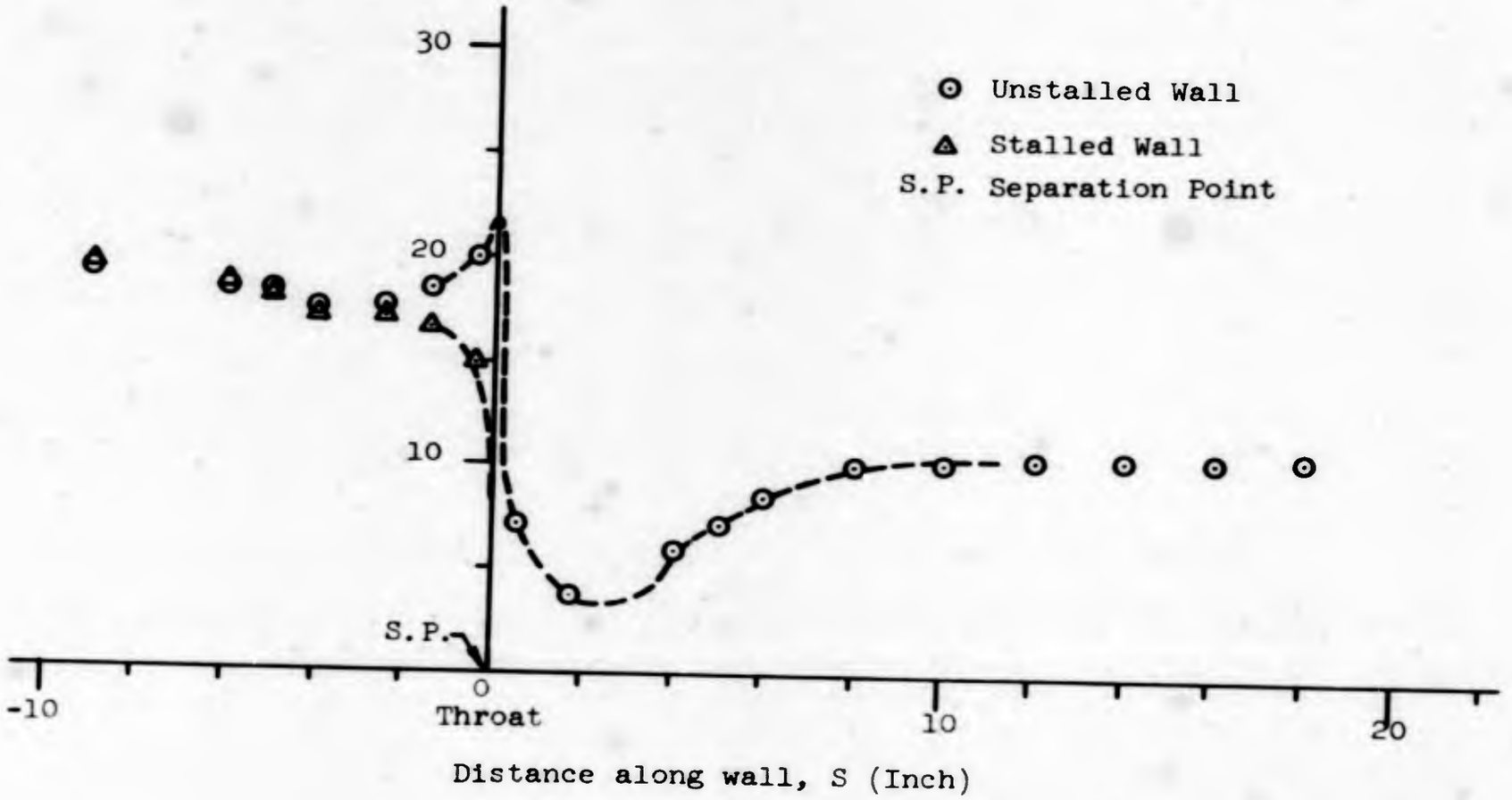

Fig. III-9 Friction factor, C_f, along side walls for REF field

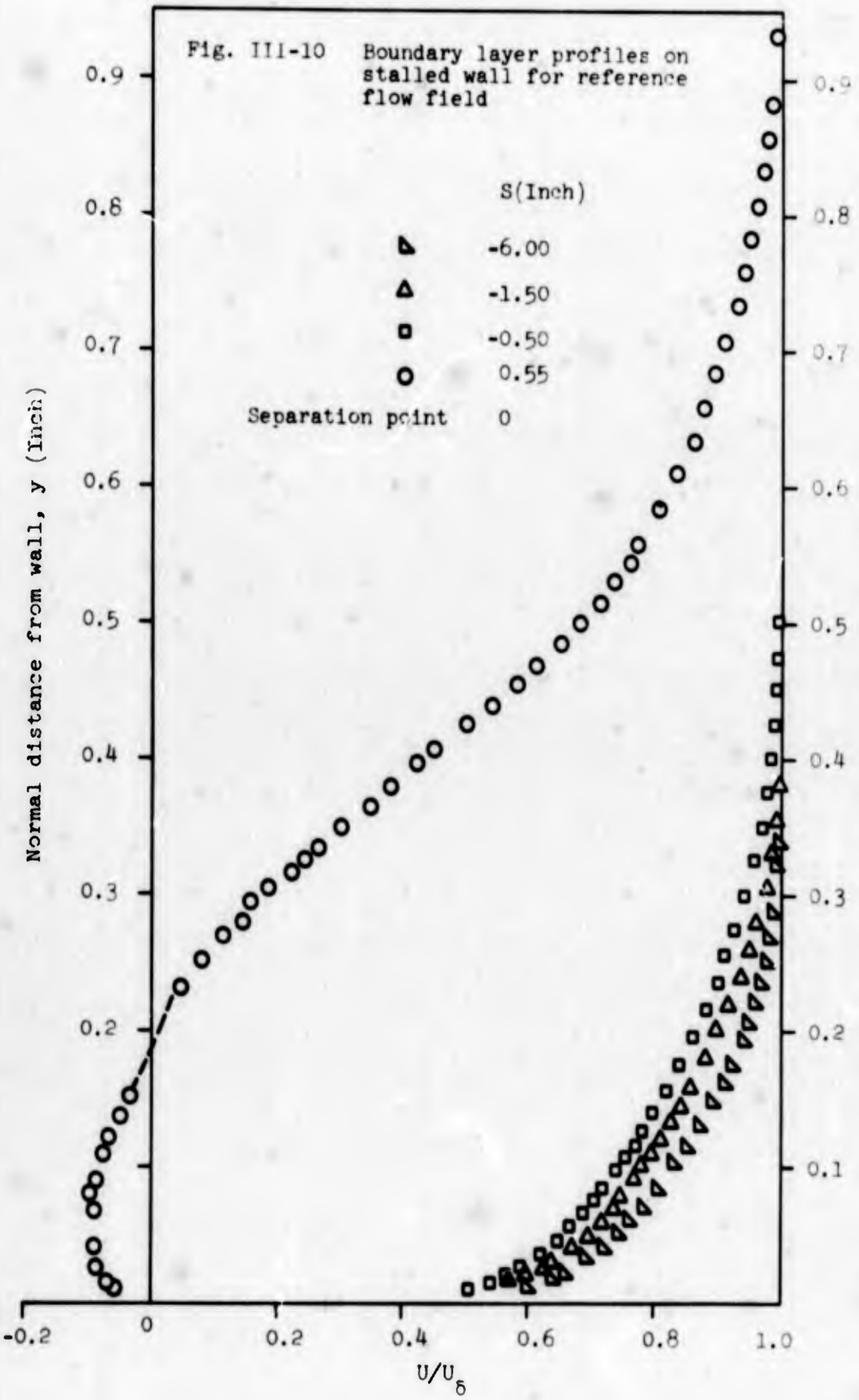
Fig. III-10 Boundary layer profiles on stalled wall for reference flow field
S(Inch)
-6.00
-1.50
-0.50
0.55
Separation point 0
Normal distance from wall, y (Inch)
0.9
0.8
0.7
0.6
0.5
0.4
0.3
0.2
0.1
-0.2
0
0.2
0.4
0.6
0.8
1.0
U/U$_\delta$

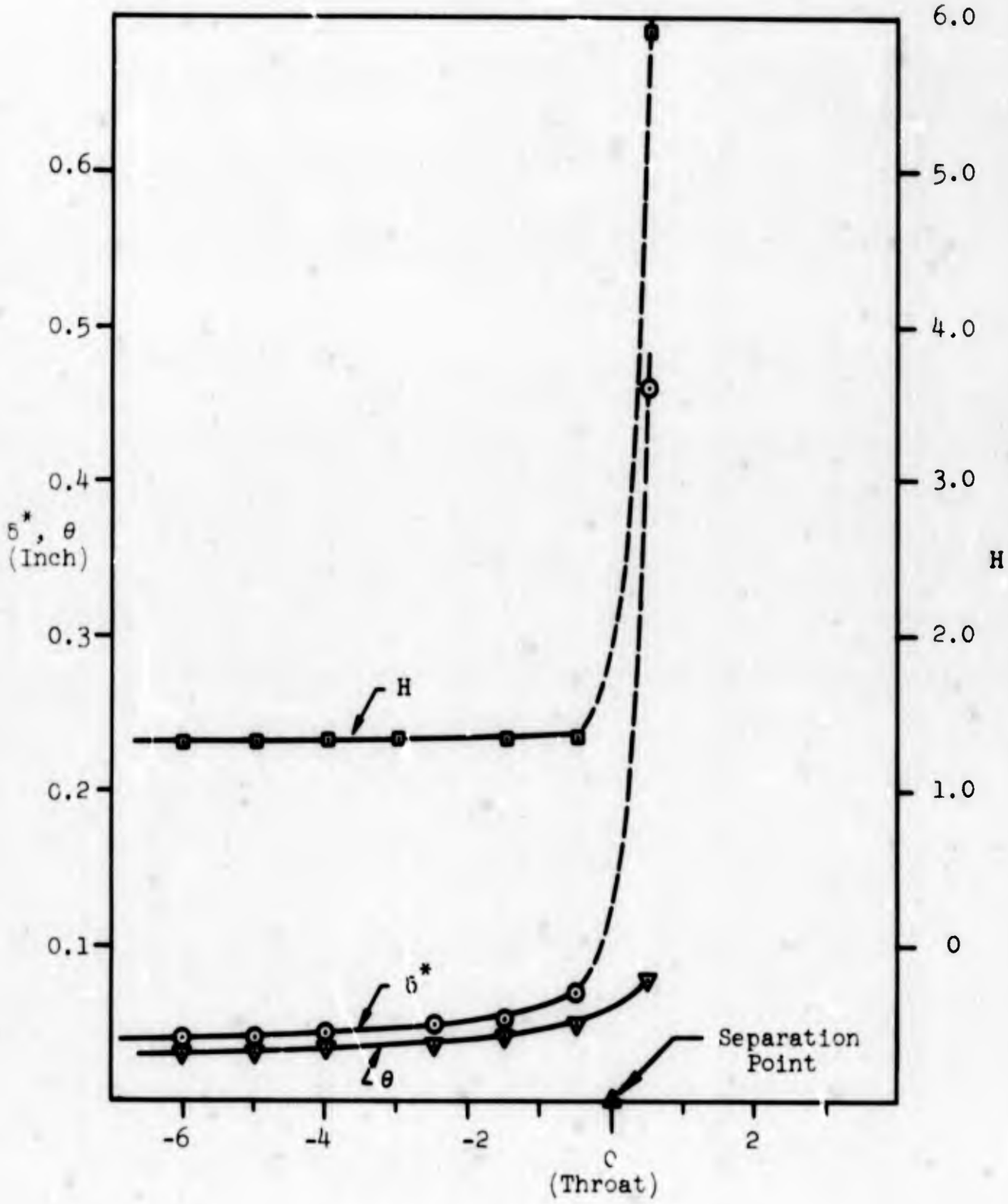

Fig. III-11 Boundary layer parameters on stalled wall for REF flow field

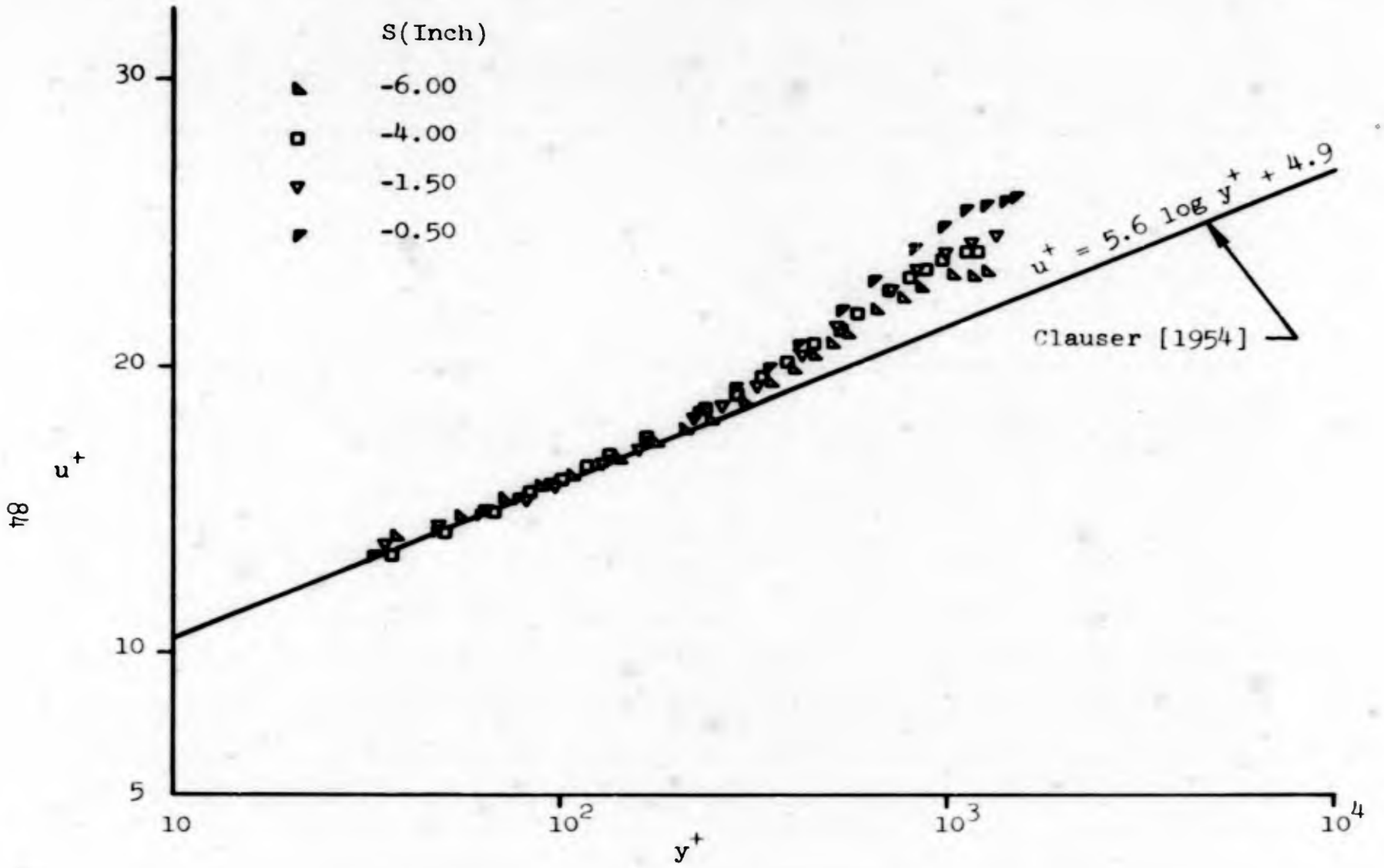

Fig. III-12 Cross plot of boundary layers before separation in reference flow field

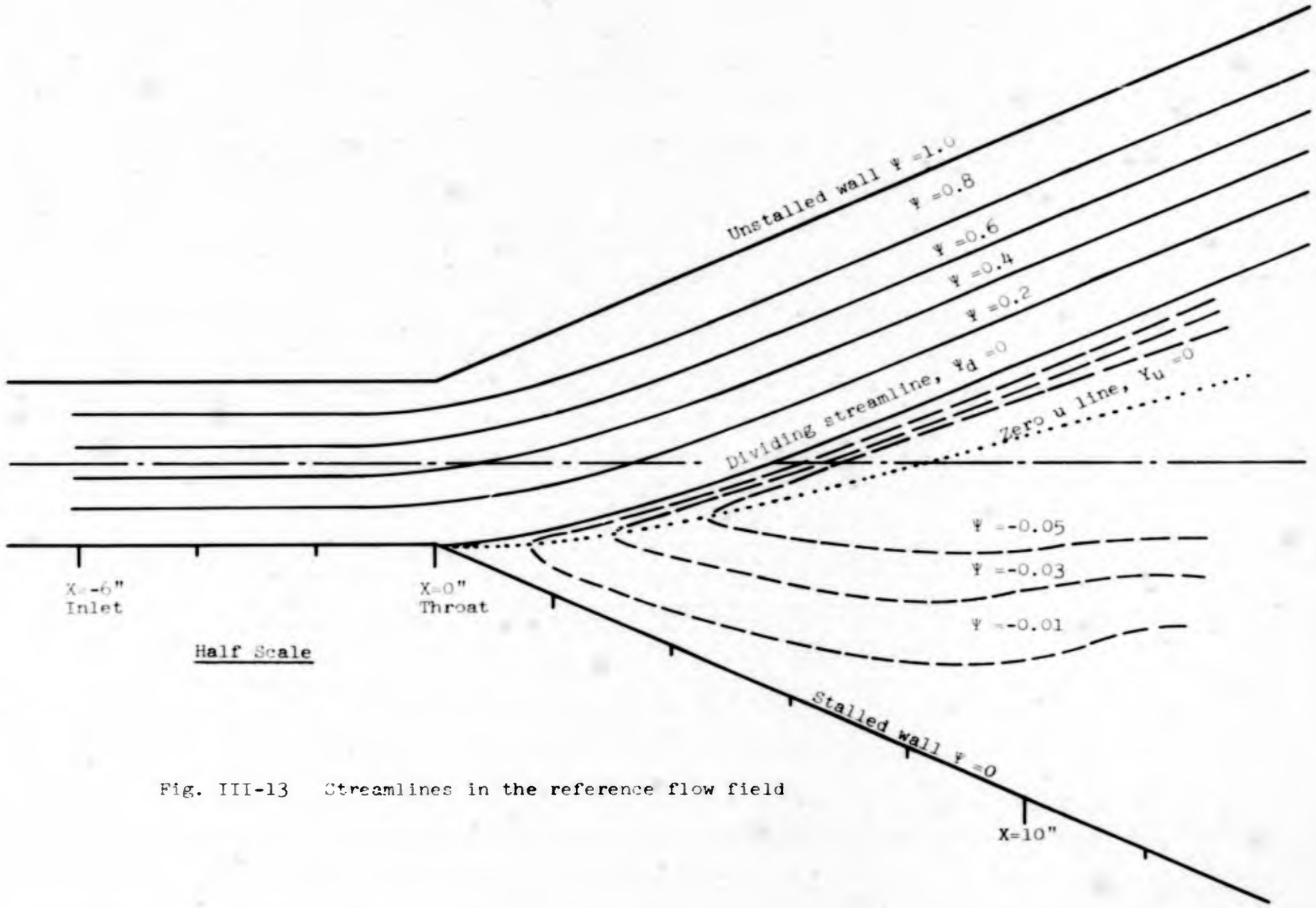

Fig. III-13 Streamlines in the reference flow field

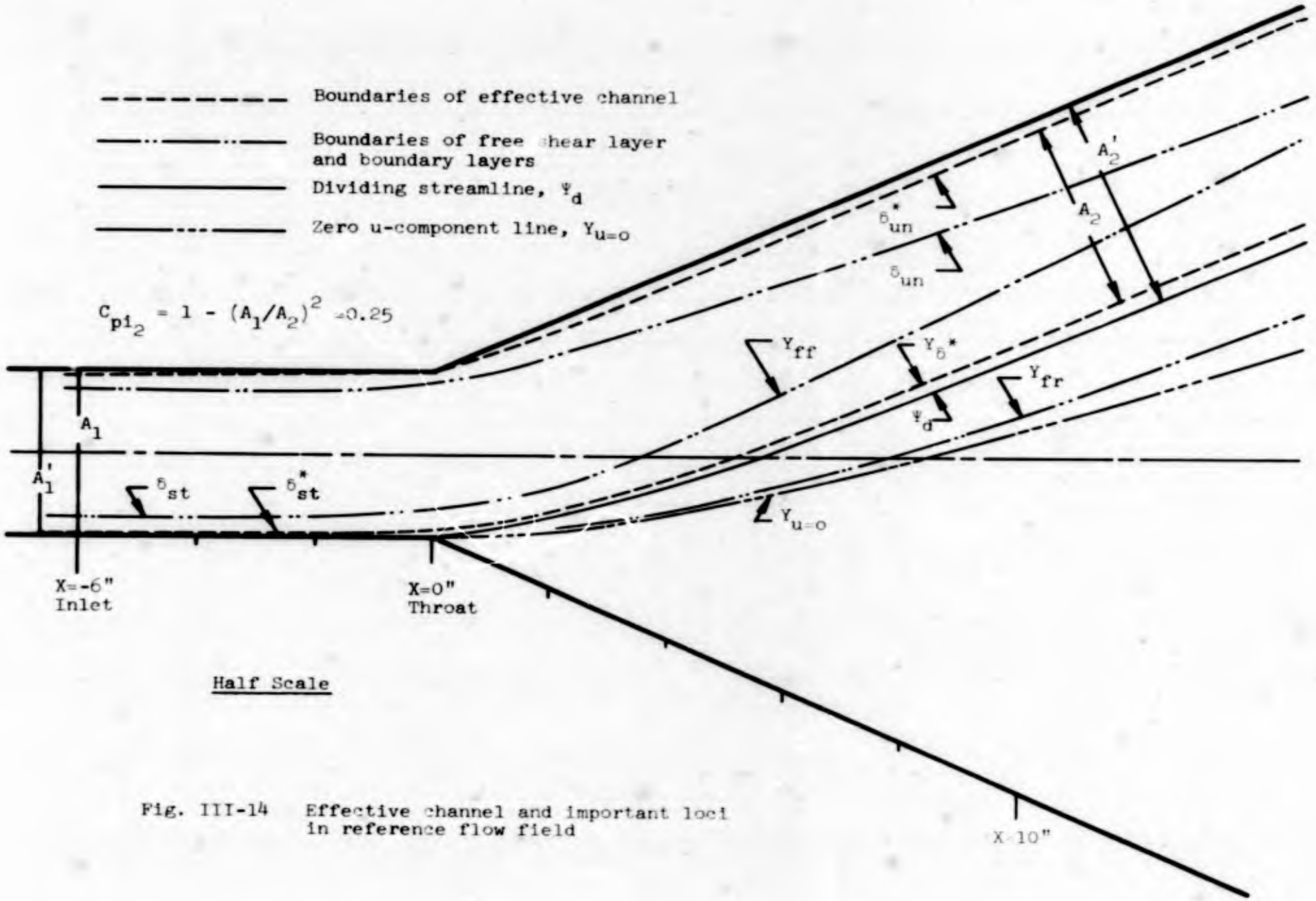

Fig. III-14 Effective channel and important loci in reference flow field

Dots are pressure coefficients as shown on fig. III-4.

Arrows are velocity vectors as shown on fig. III-5.

Both are relative to base-lines as in figs. III-4, III-5.

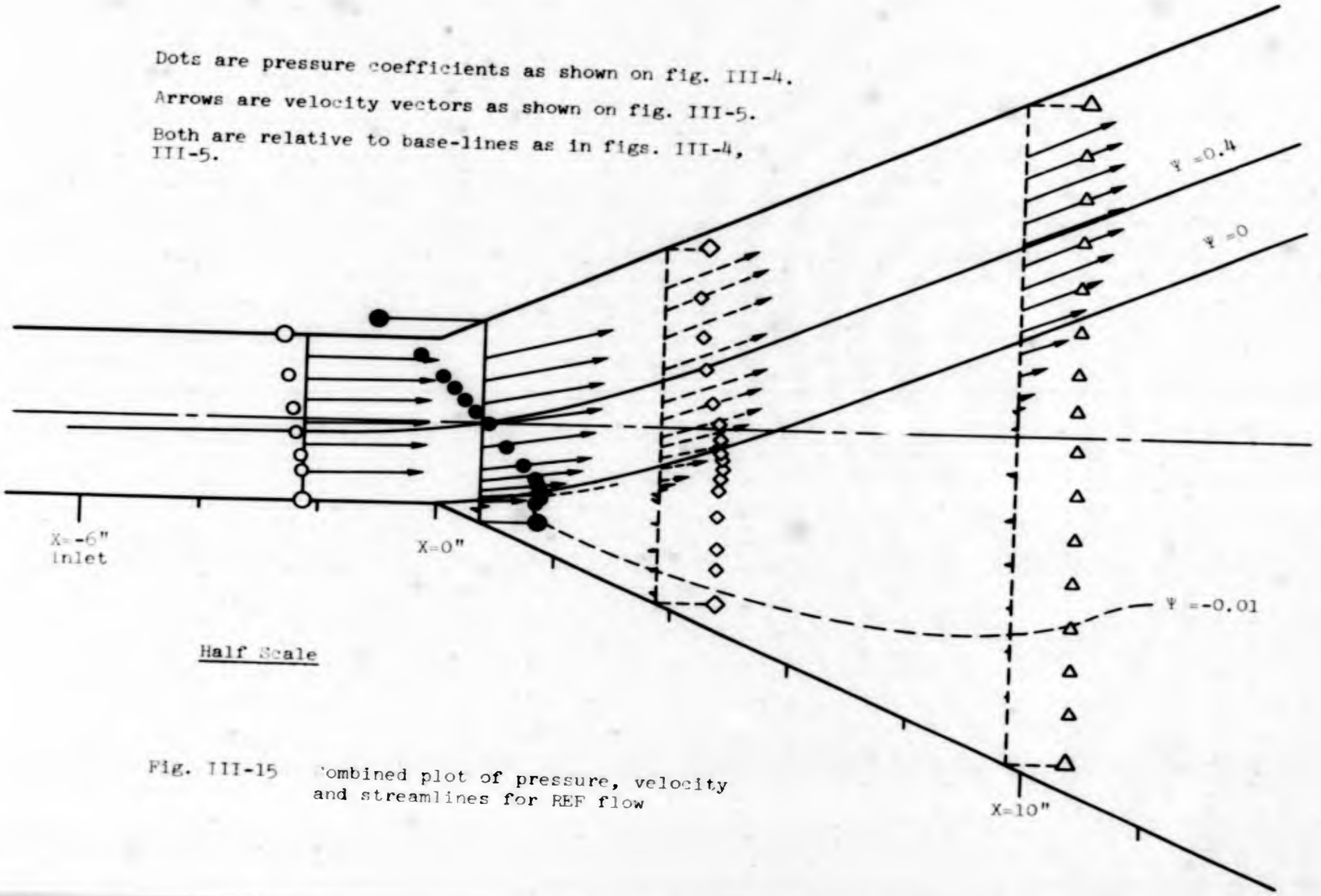

Fig. III-15 Combined plot of pressure, velocity and streamlines for REF flow

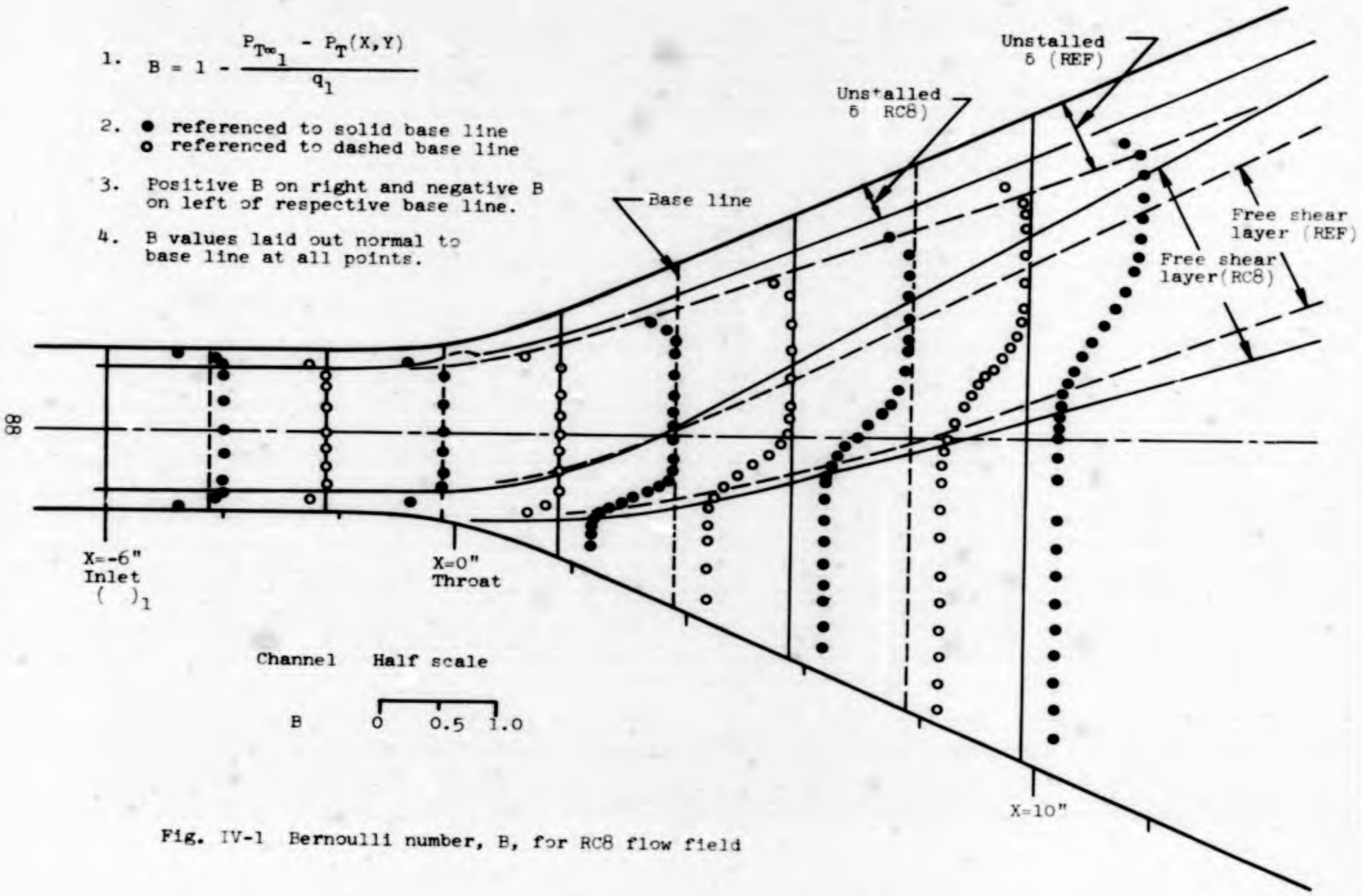

Fig. IV-1 Bernoulli number, B, for RC8 flow field

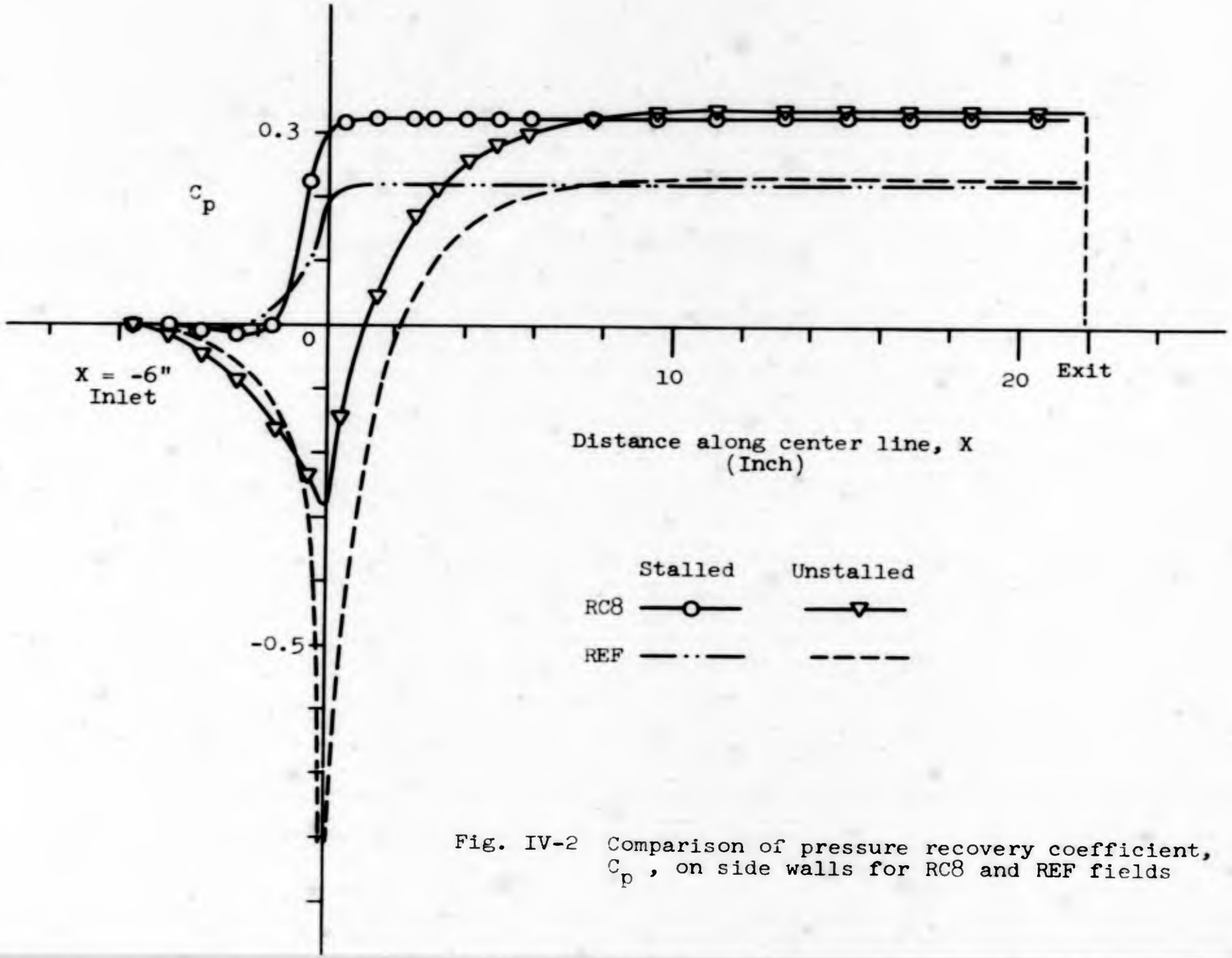

Fig. IV-2 Comparison of pressure recovery coefficient, C_p, on side walls for RC8 and REF fields

Note:

1. $C_p = \frac{P(X,Y) - P_1}{q_1}$
2. Symbols are for C_p in RC8 flow field. Dashed curves are C_p in REF flow field.
3. C_p values laid out normal to base line at all points.
4. Positive C_p are on right and negative C_p are on left of respective base line.

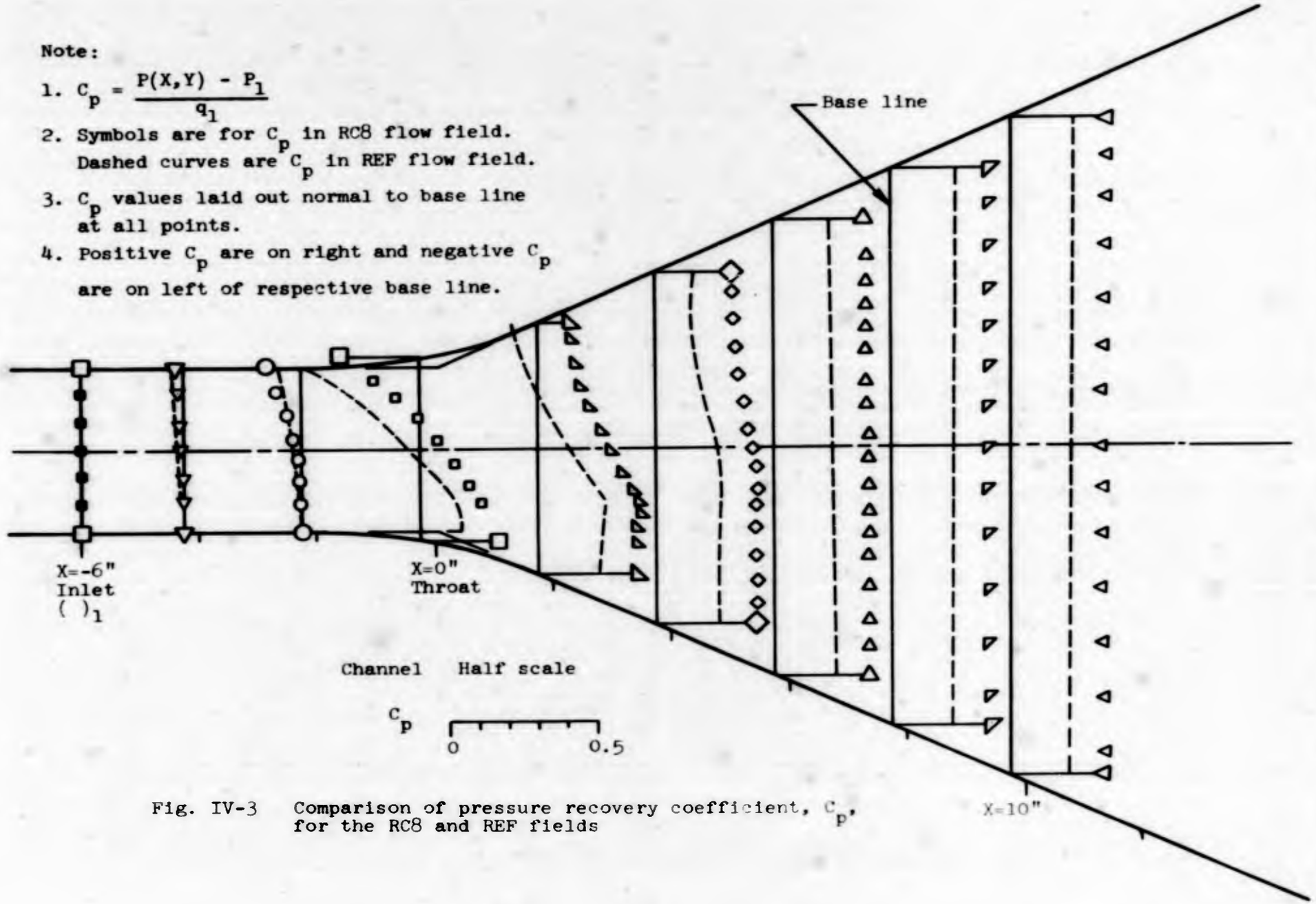

Fig. IV-3 Comparison of pressure recovery coefficient, C_p, for the RC8 and REF fields

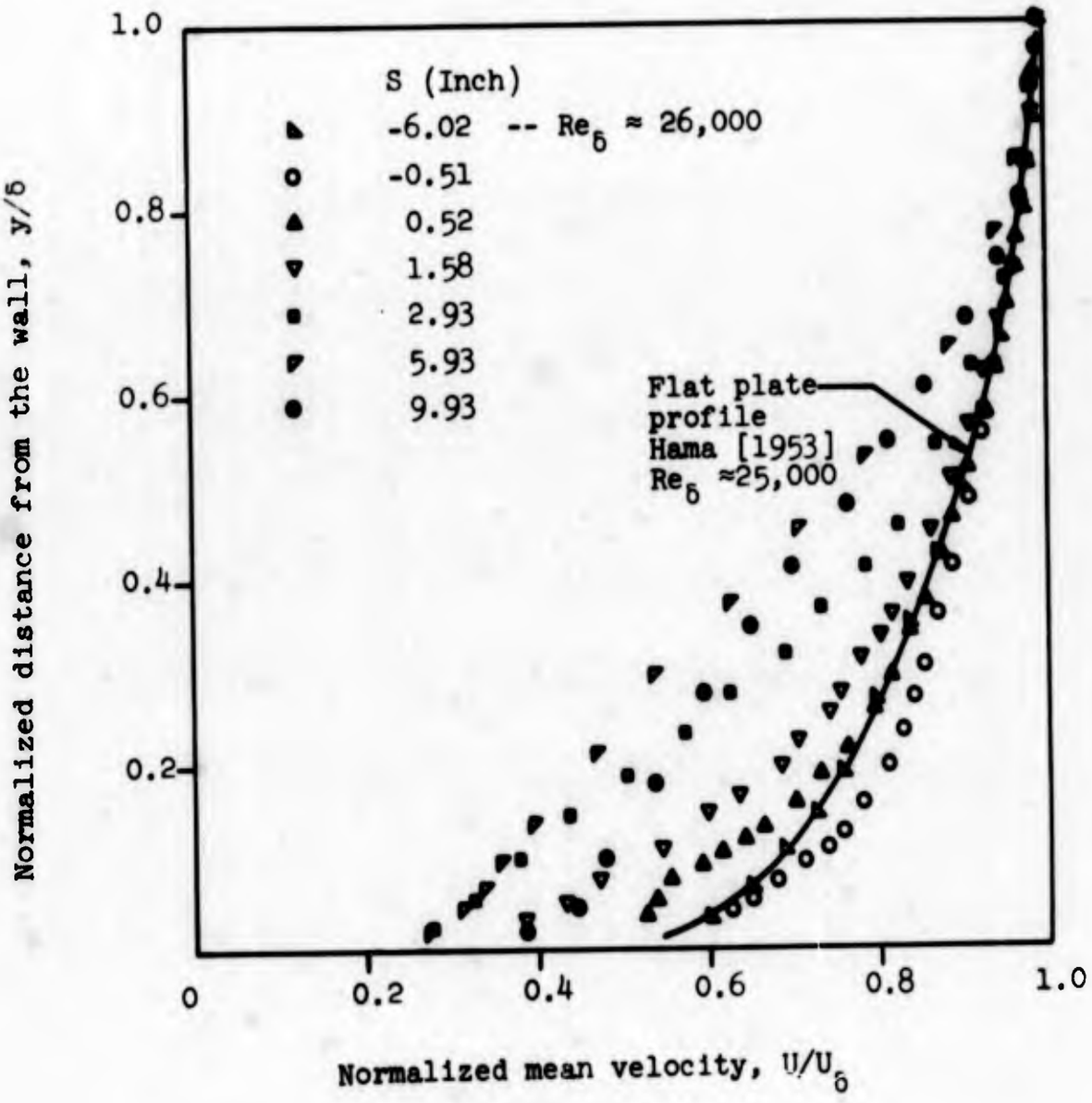

Fig. IV-4 Boundary layer profiles on unstalled wall for RC8 case

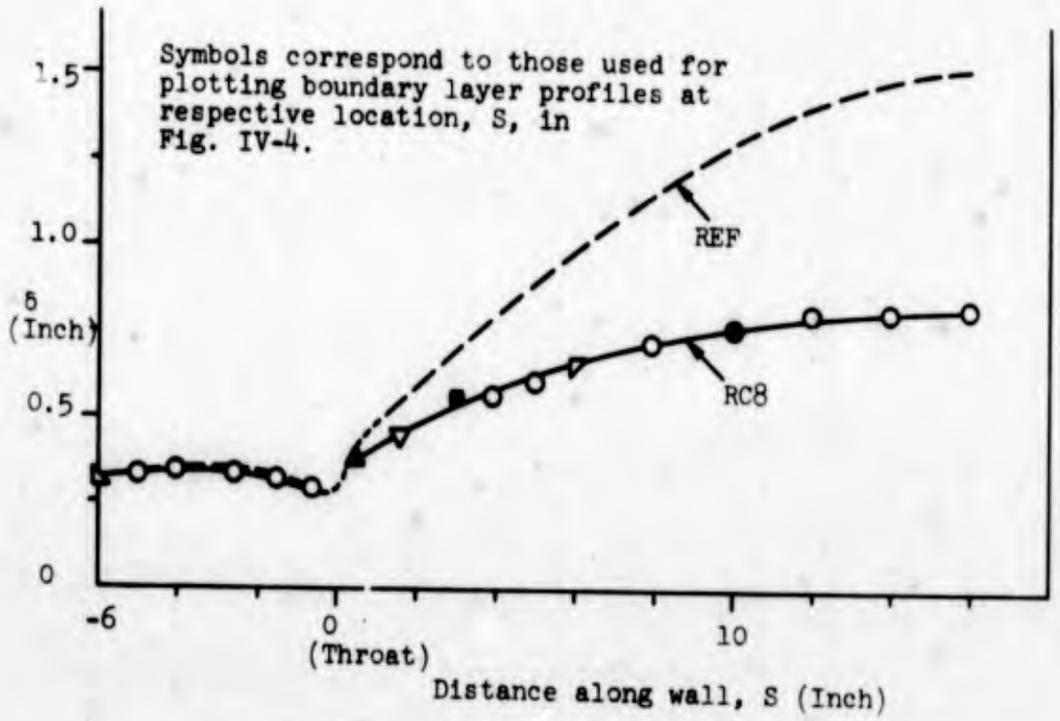

Fig. IV-5a Comparison of boundary layer thicknesses on unstalled wall for RC8 and REF flow field

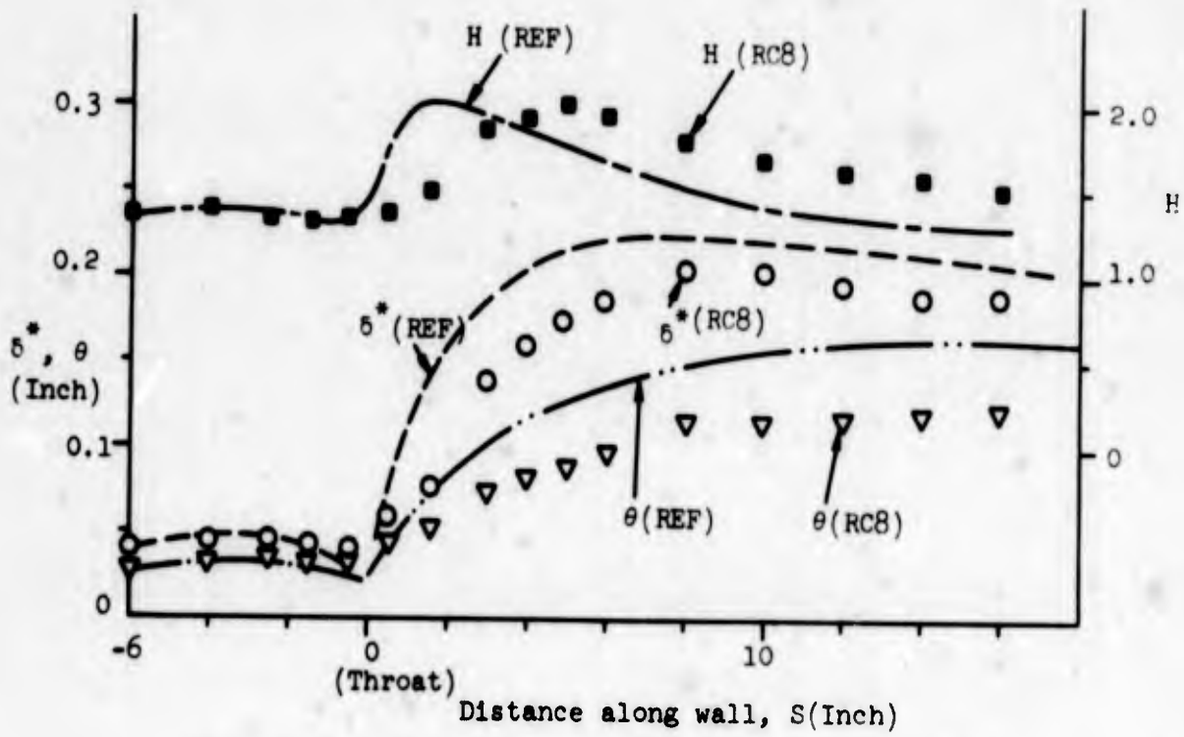

Fig. IV-5b Comparison of boundary layer parameters on unstalled wall for RC8 and REF flow field

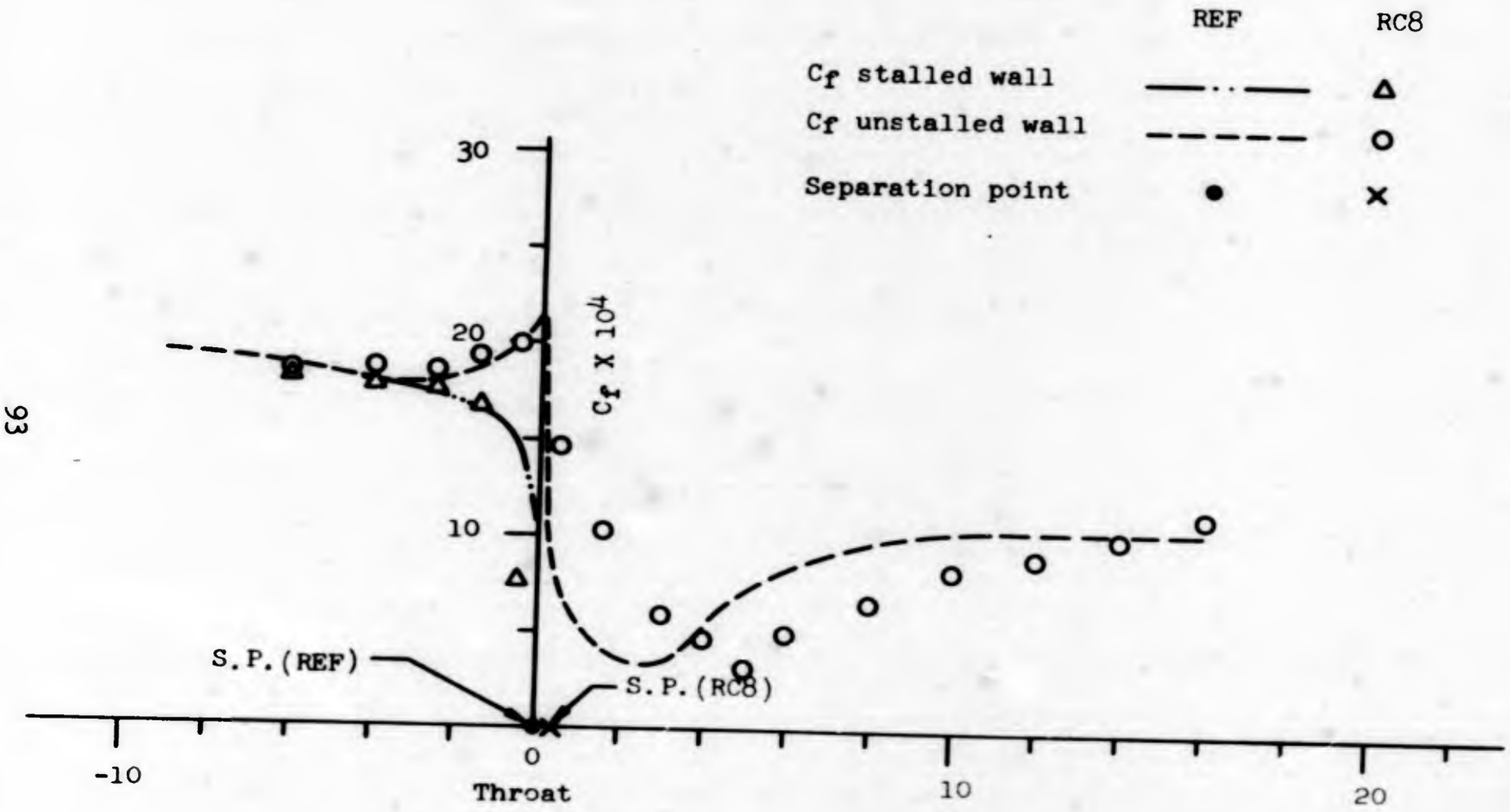

Fig. IV-6 Comparison of friction factor, C_f, along side walls for RC8 and REF flow fields

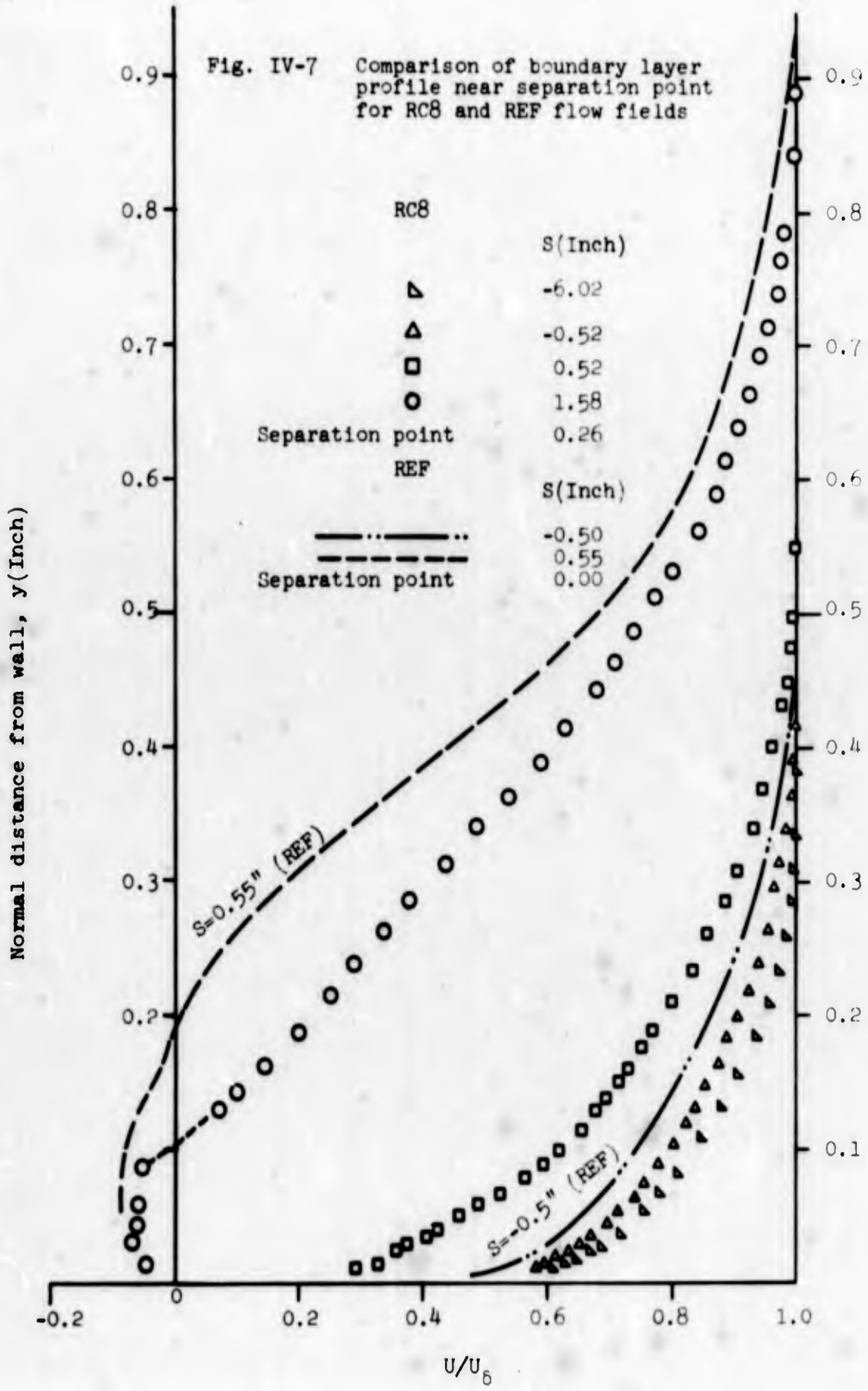
Fig. IV-7 Comparison of boundary layer profile near separation point for RC8 and REF flow fields
RC8
S(Inch)
-6.02
-0.52
0.52
1.58
Separation point 0.26
REF
S(Inch)
-0.50
0.55
Separation point 0.00
S=0.55" (REF)
S=-0.5" (REF)
Normal distance from wall, y(Inch)
U/U$_\delta$
0.9
0.8
0.7
0.6
0.5
0.4
0.3
0.2
0.1
-0.2
0
0.2
0.4
0.6
0.8
1.0

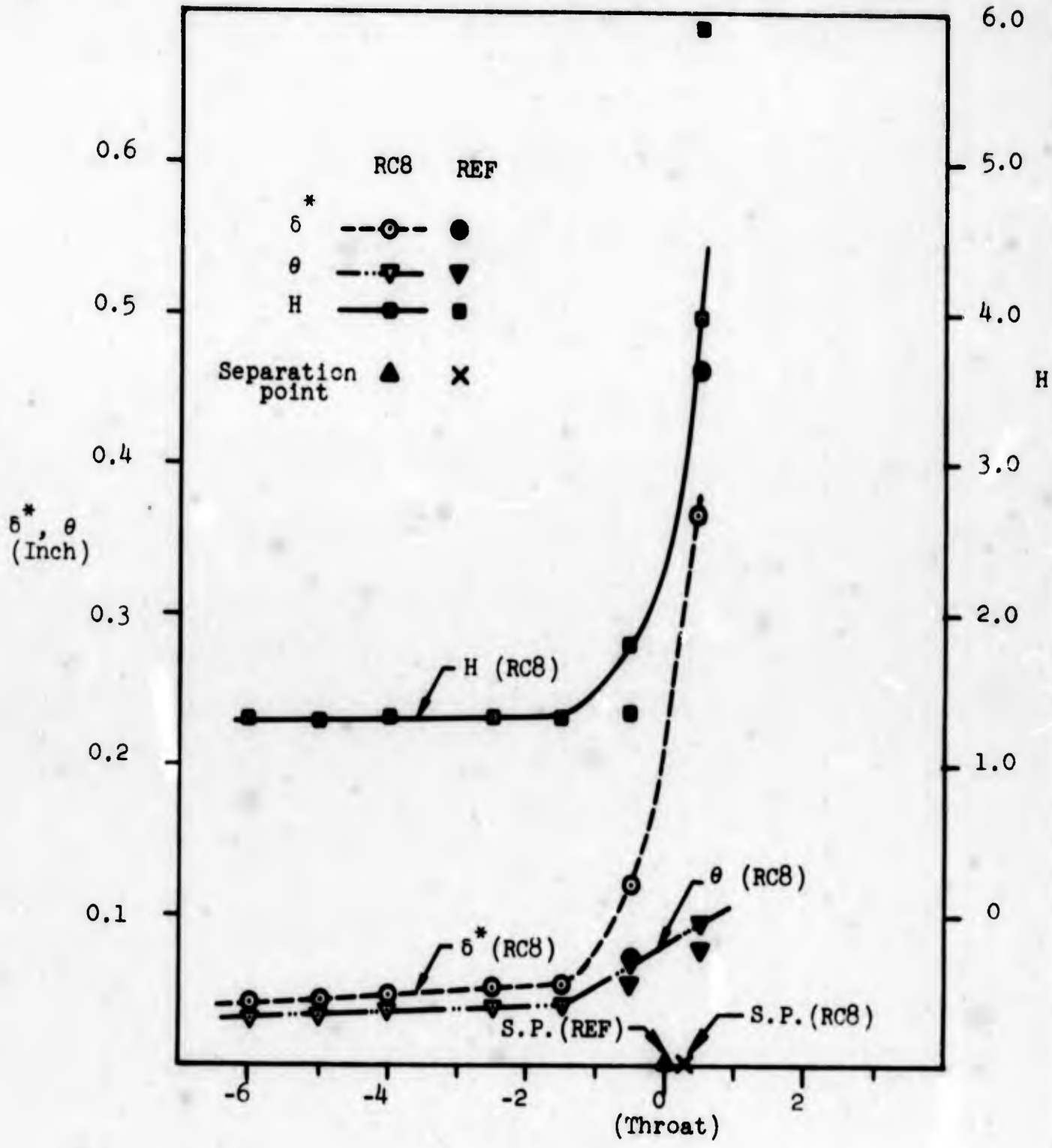

Fig. IV-8 Boundary layer parameters on stalled wall of RC8 flow field and comparison of their changes against those in REF flow around the separation point

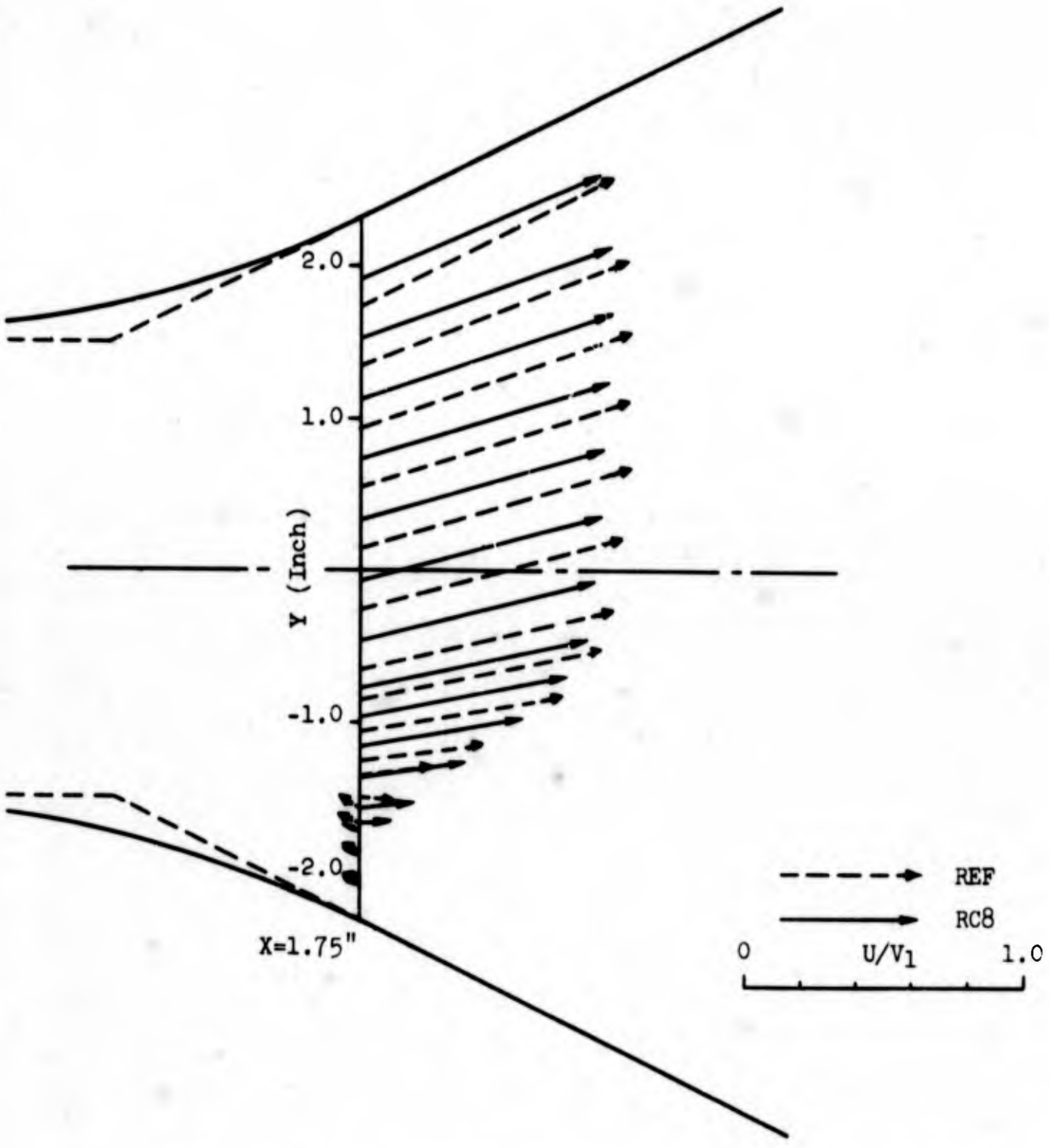

Fig. IV-9a Comparison of velocity/inlet average velocity, U/V_1 at X=1.75" for RC8 and REF flow fields

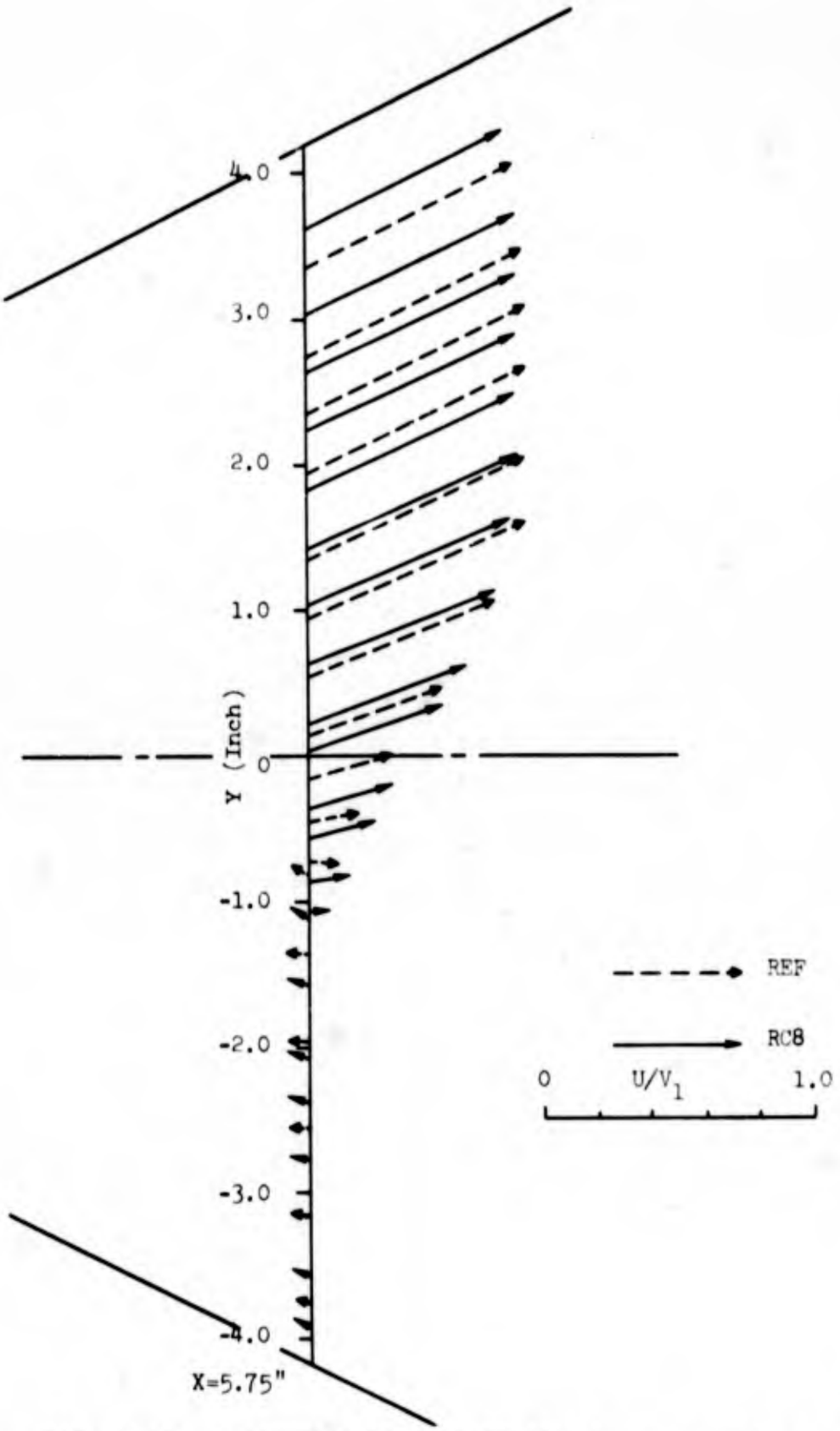

Fig. IV-9b Comparison of velocity/inlet average velocity U/V_1, at X=5.75" for RC8 and REF flow fields

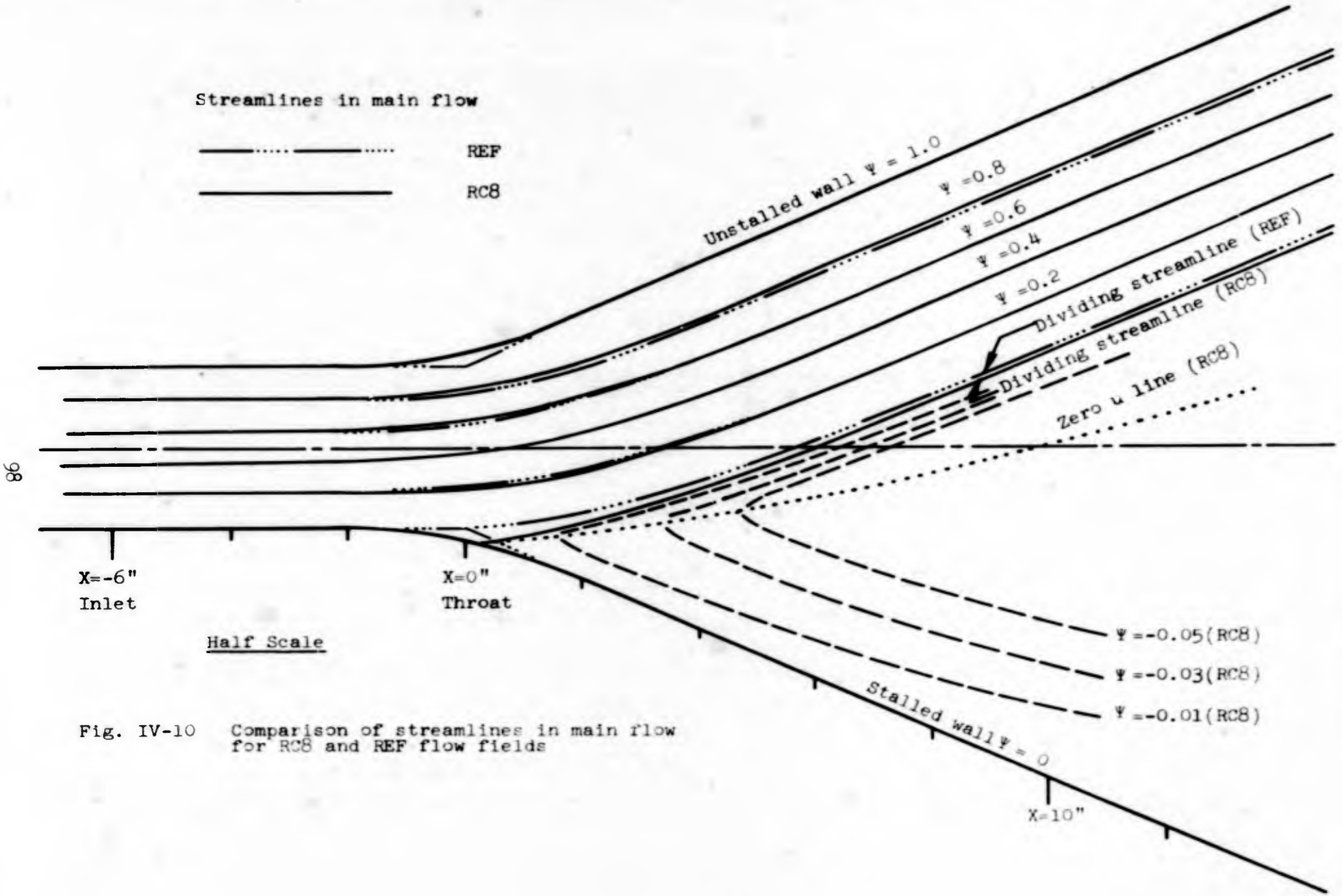

Fig. IV-10 Comparison of streamlines in main flow for RC8 and REF flow fields

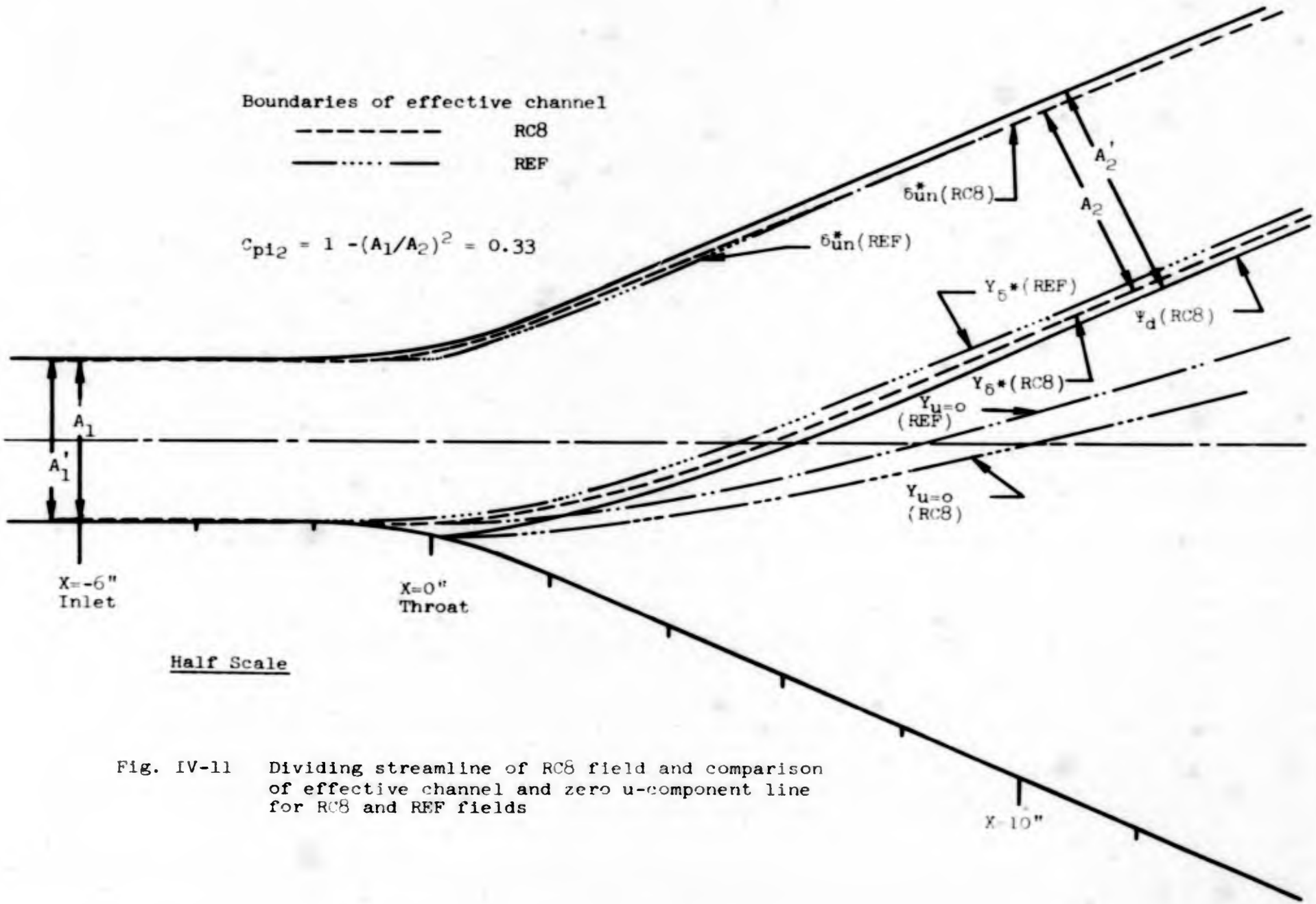

Fig. IV-11 Dividing streamline of RC8 field and comparison of effective channel and zero u-component line for RC8 and REF fields

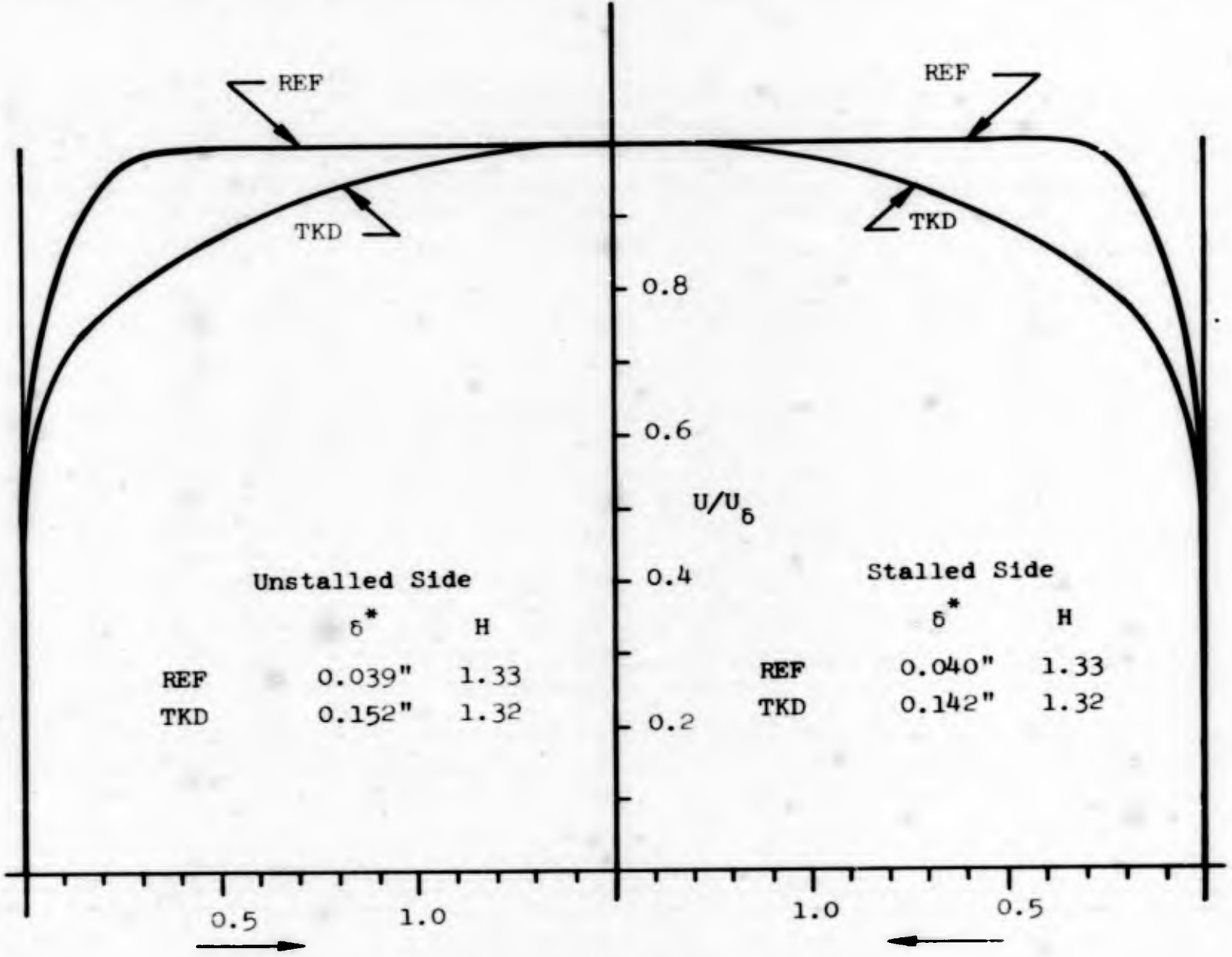

Fig. IV-12 Comparison of inlet velocity profile for TKD and REF flow fields

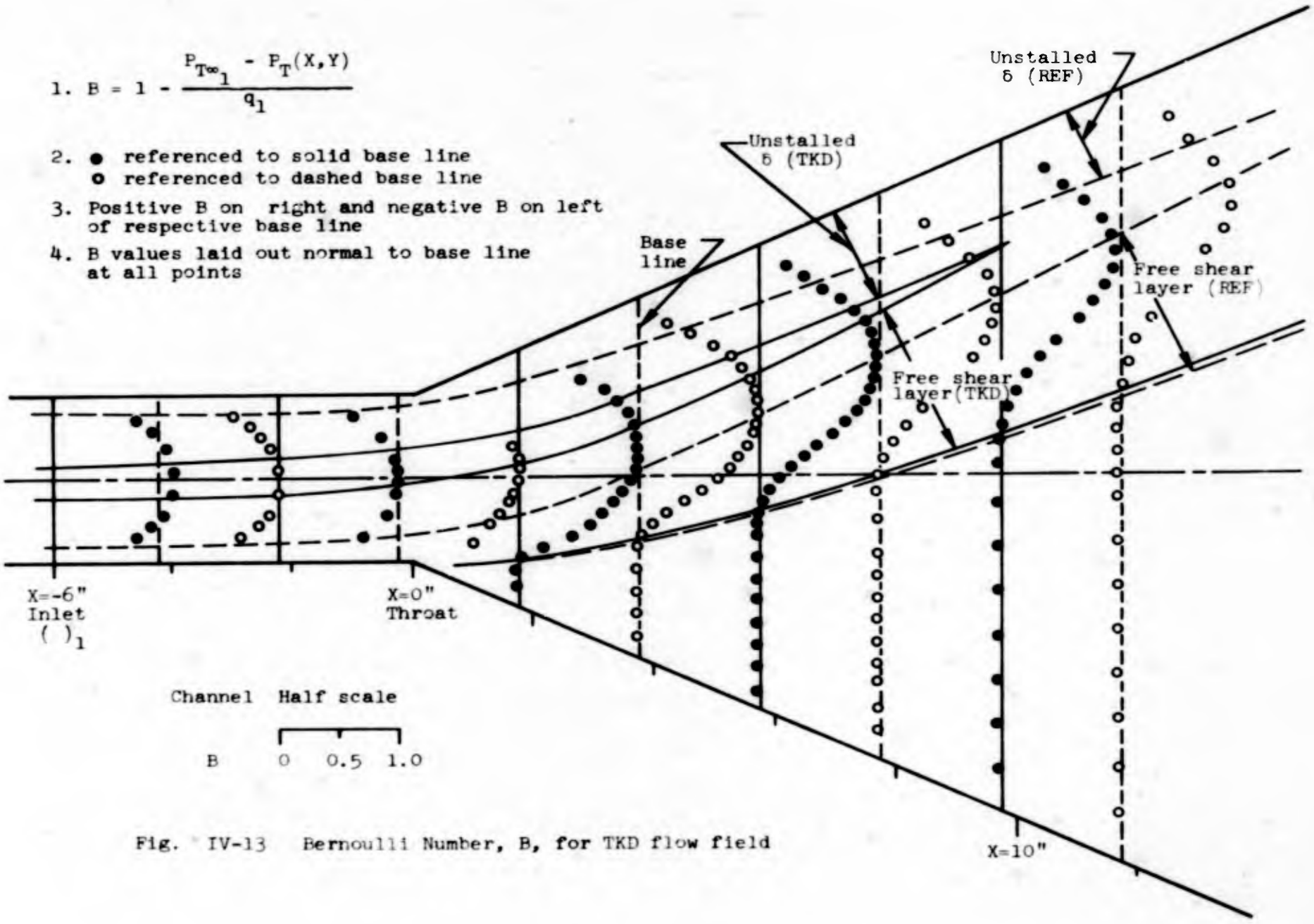

Fig. IV-13 Bernoulli Number, B, for TKD flow field

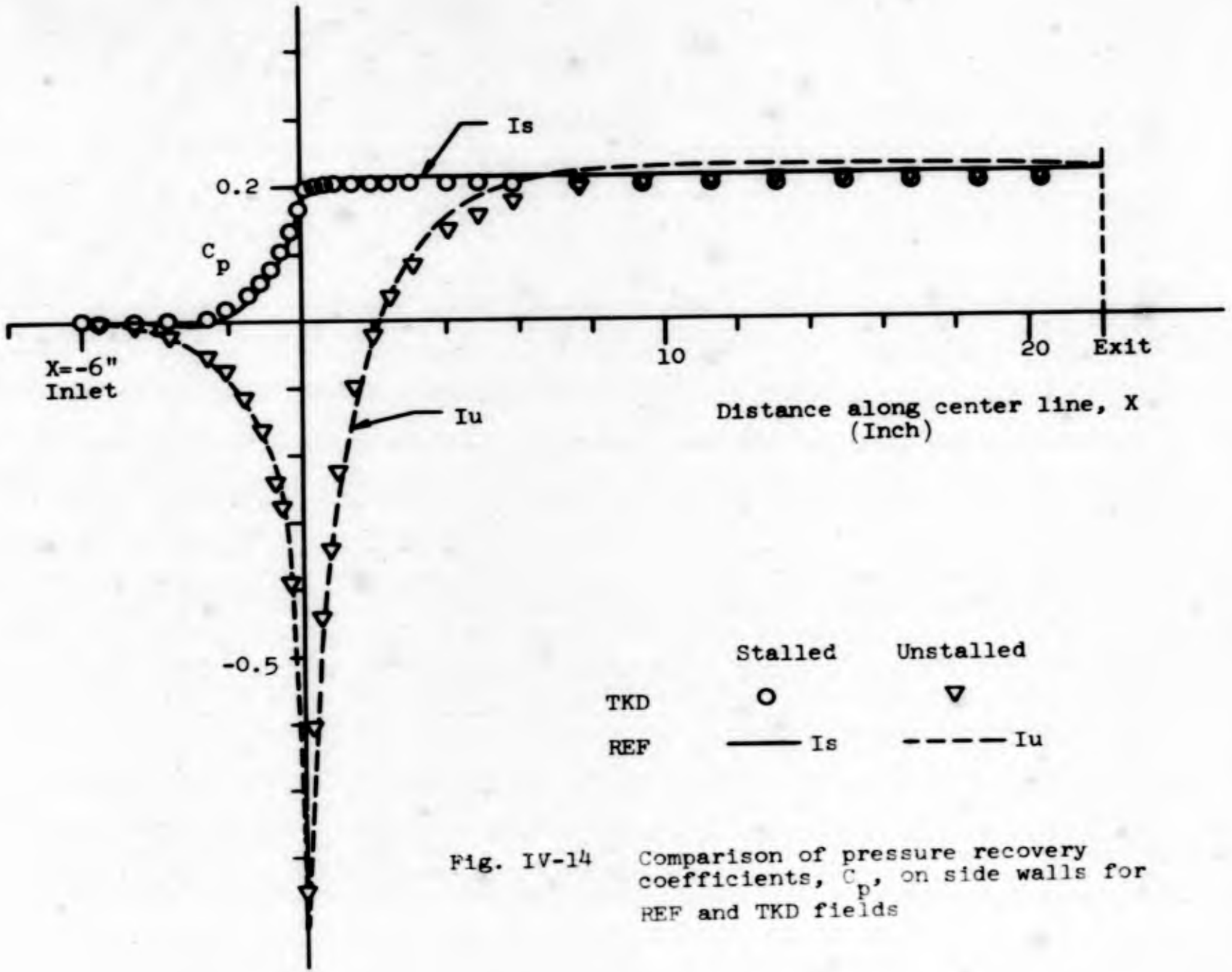

Fig. IV-14 Comparison of pressure recovery coefficients, C_p, on side walls for REF and TKD fields

Note:

1. $C_p = \dfrac{P(X,Y) - P_1}{q_1}$
2. Symbols are for C_p in TKD flow field. Dashed curves are C_p in REF flow field.
3. C_p values laid out normal to base line at all points.
4. Positive C_p are on right and negative C_p are on left of respective base line.

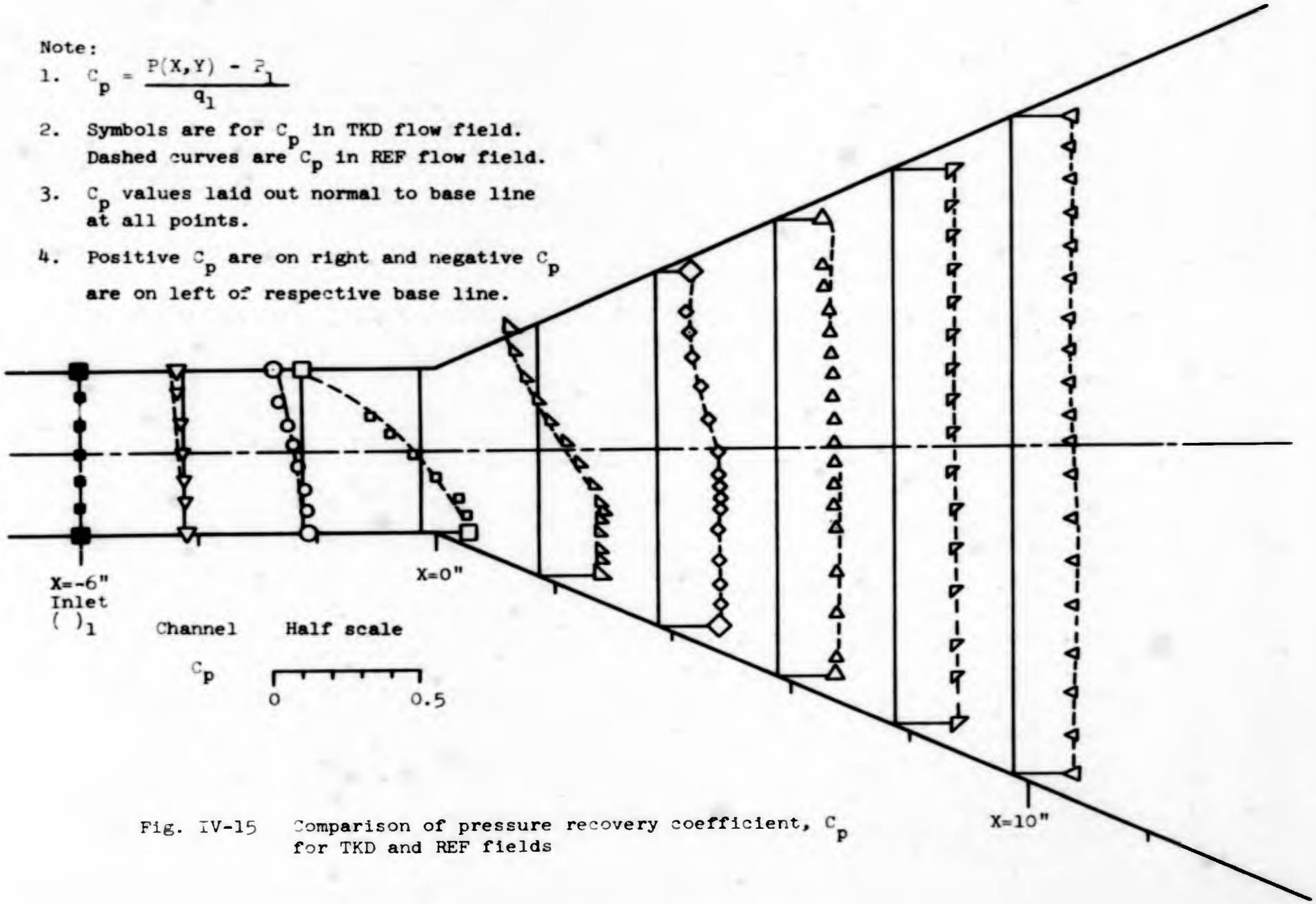

Fig. IV-15 Comparison of pressure recovery coefficient, C_p for TKD and REF fields

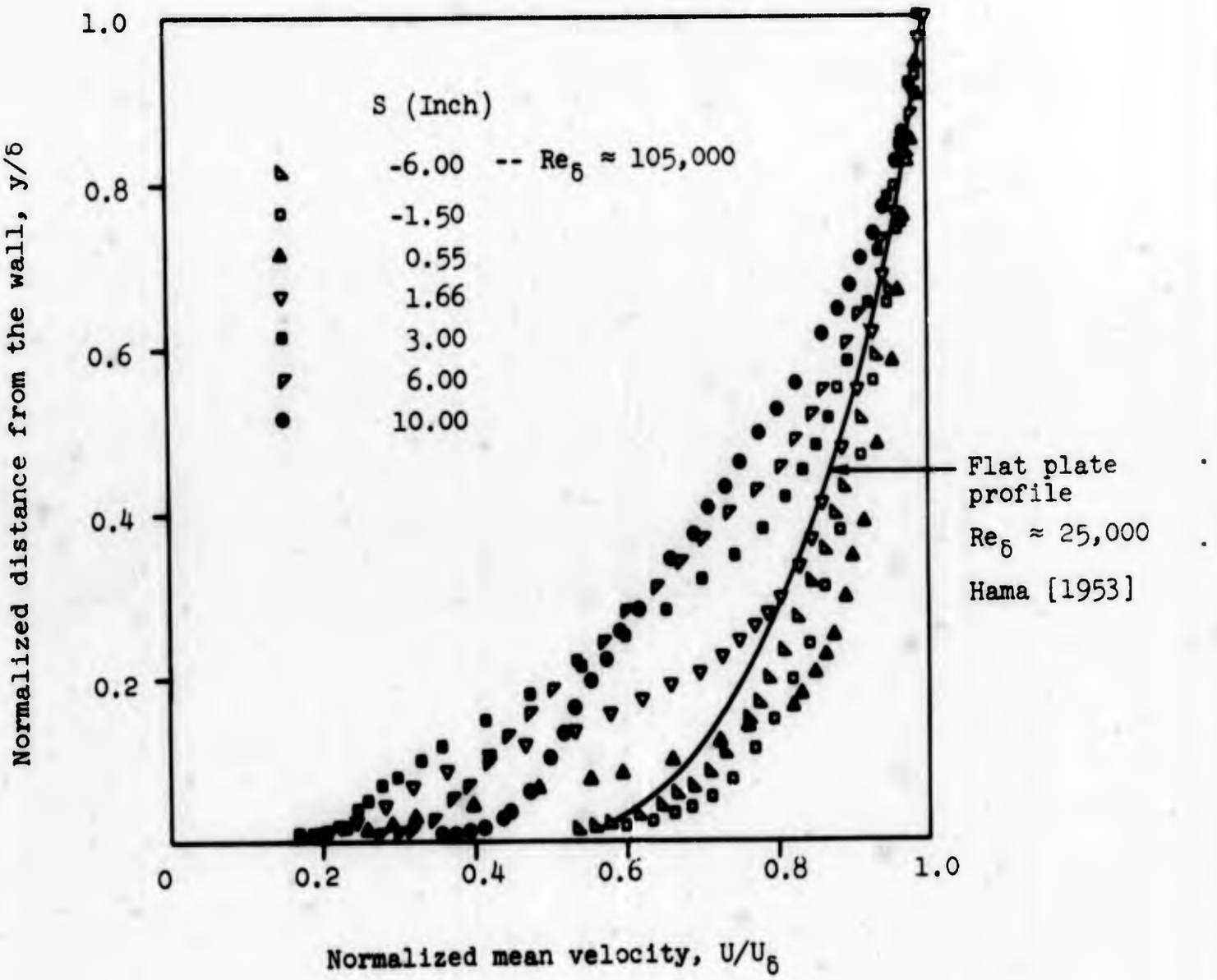

Fig. IV-16 Boundary layer profiles on unstalled wall for TKD flow

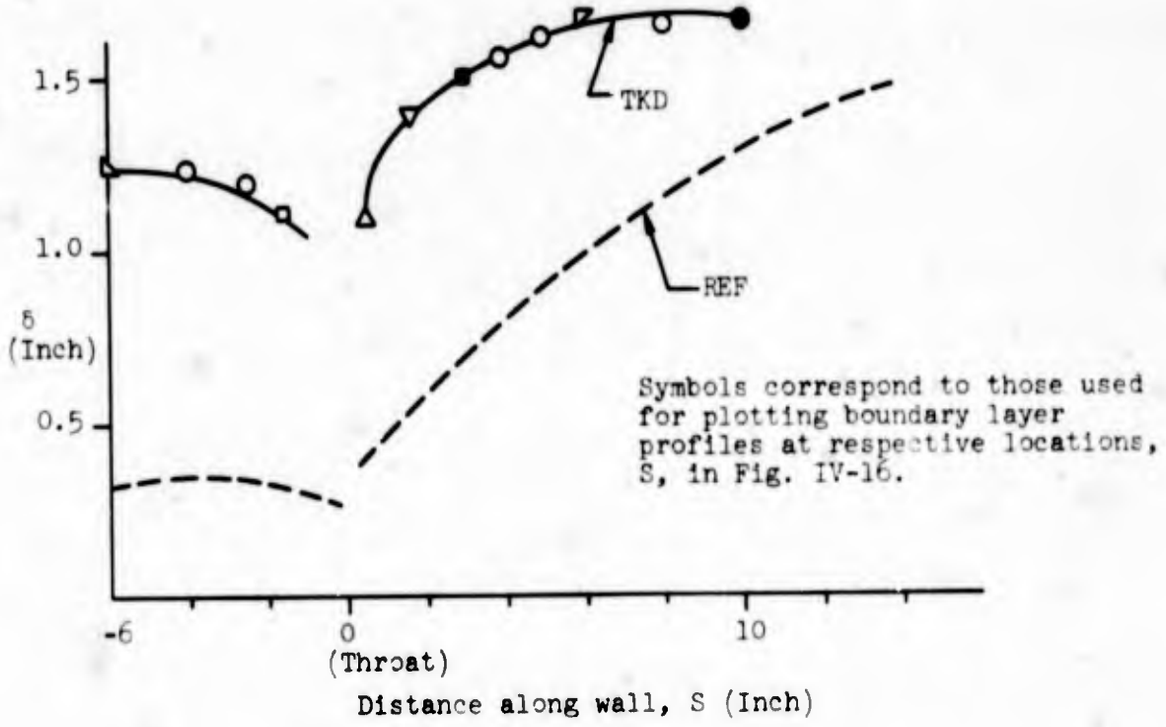

Fig. IV-17a Comparison of boundary layer thicknesses on unstalled wall for REF and TKD flow field

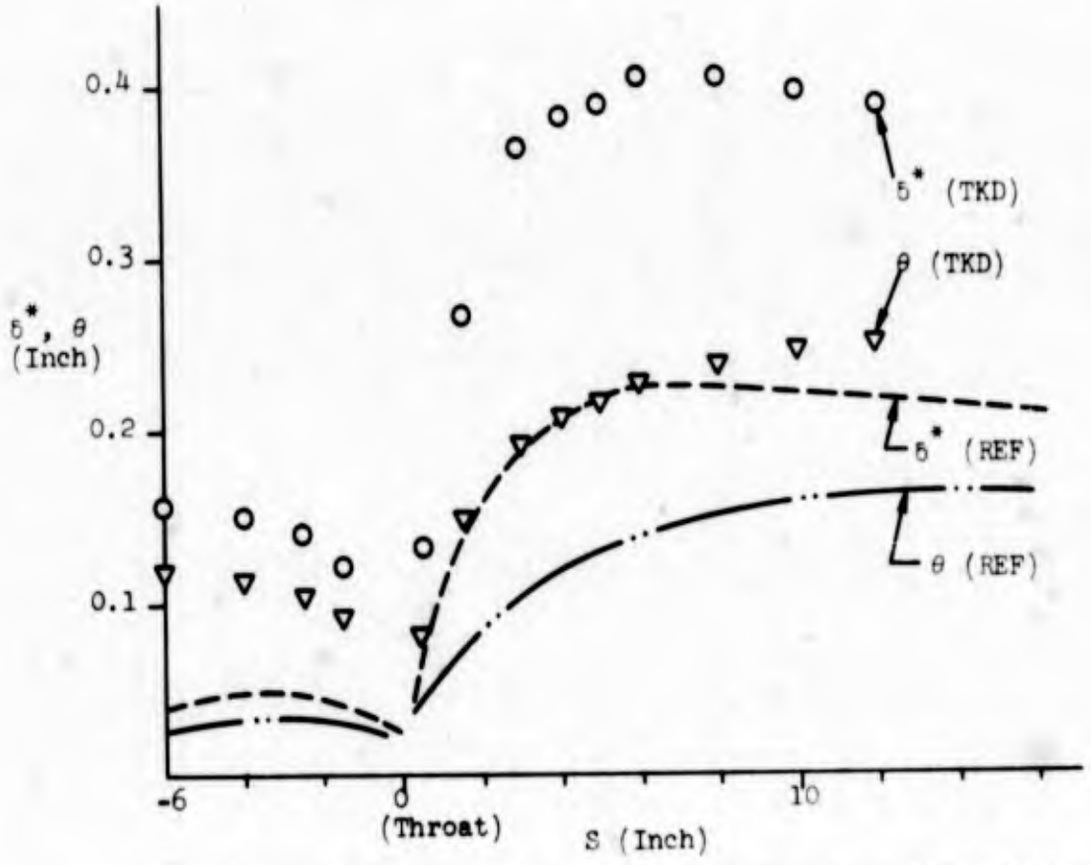

Fig. IV-17b Comparison of boundary layer parameters on unstalled wall for TKD and REF flow fields

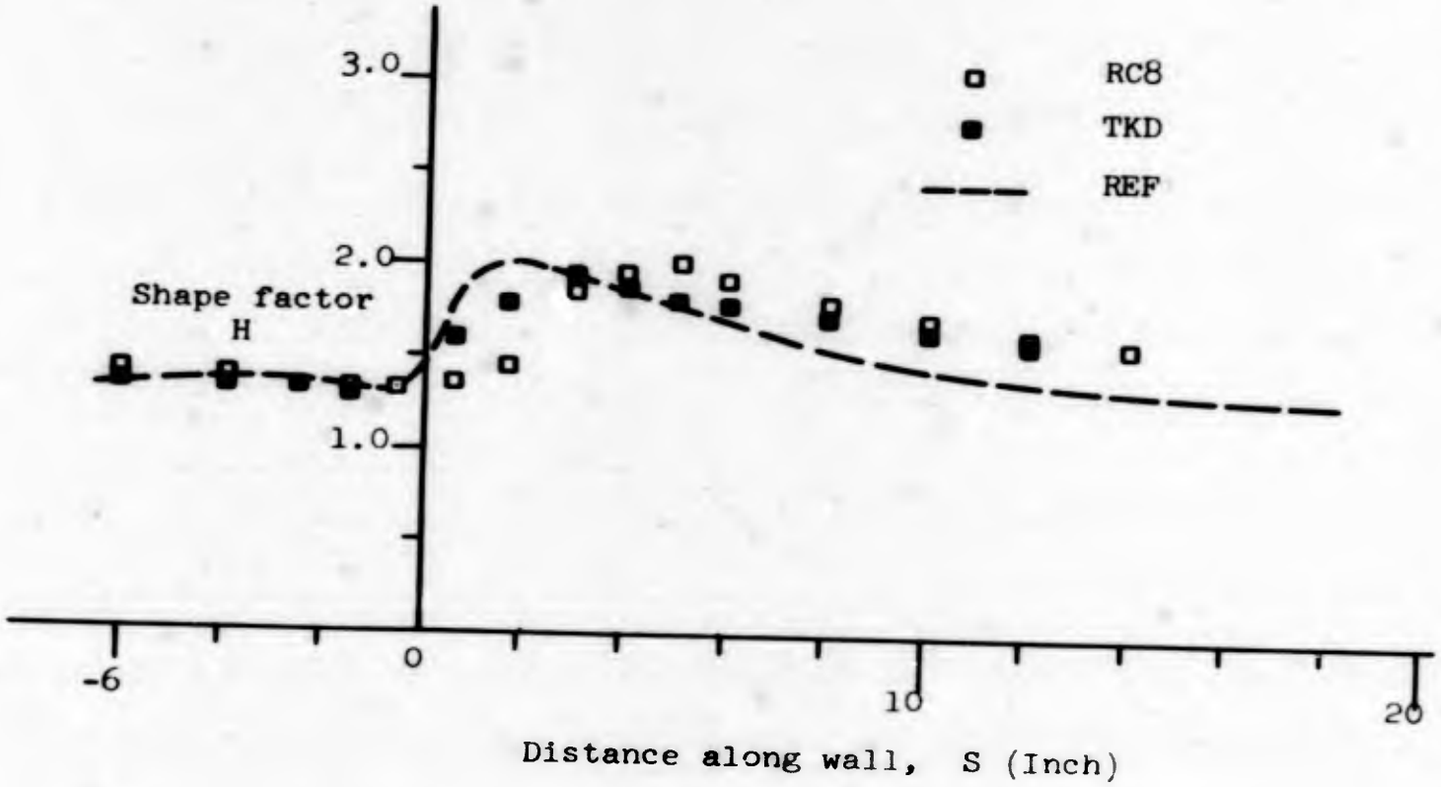

Fig. IV-18 Comparison of shape factors on unstalled wall for REF, RC8 and TKD flow fields

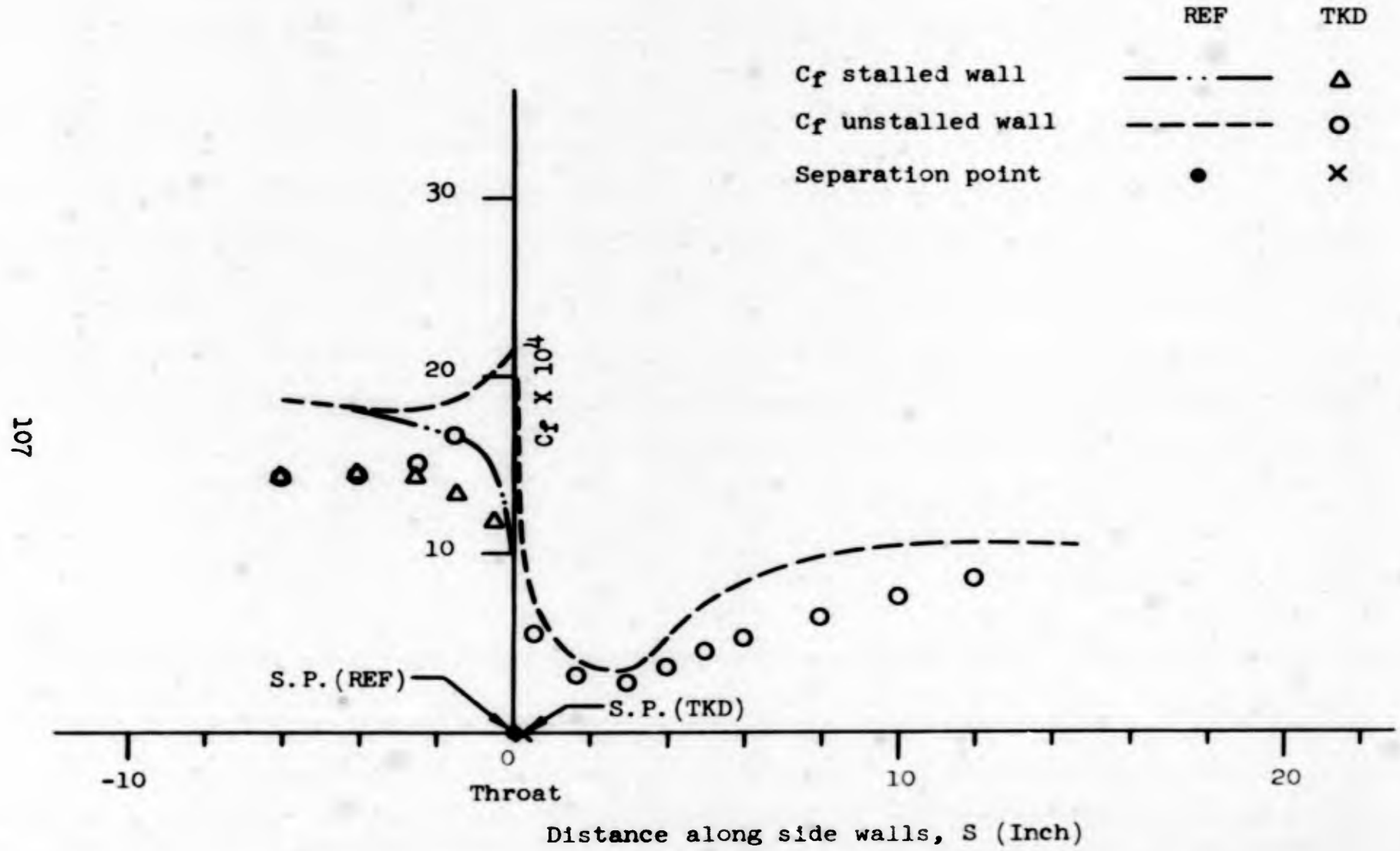

Fig. IV-19 Comparison of friction factor, C_f, along side walls for TKD and REF flow fields

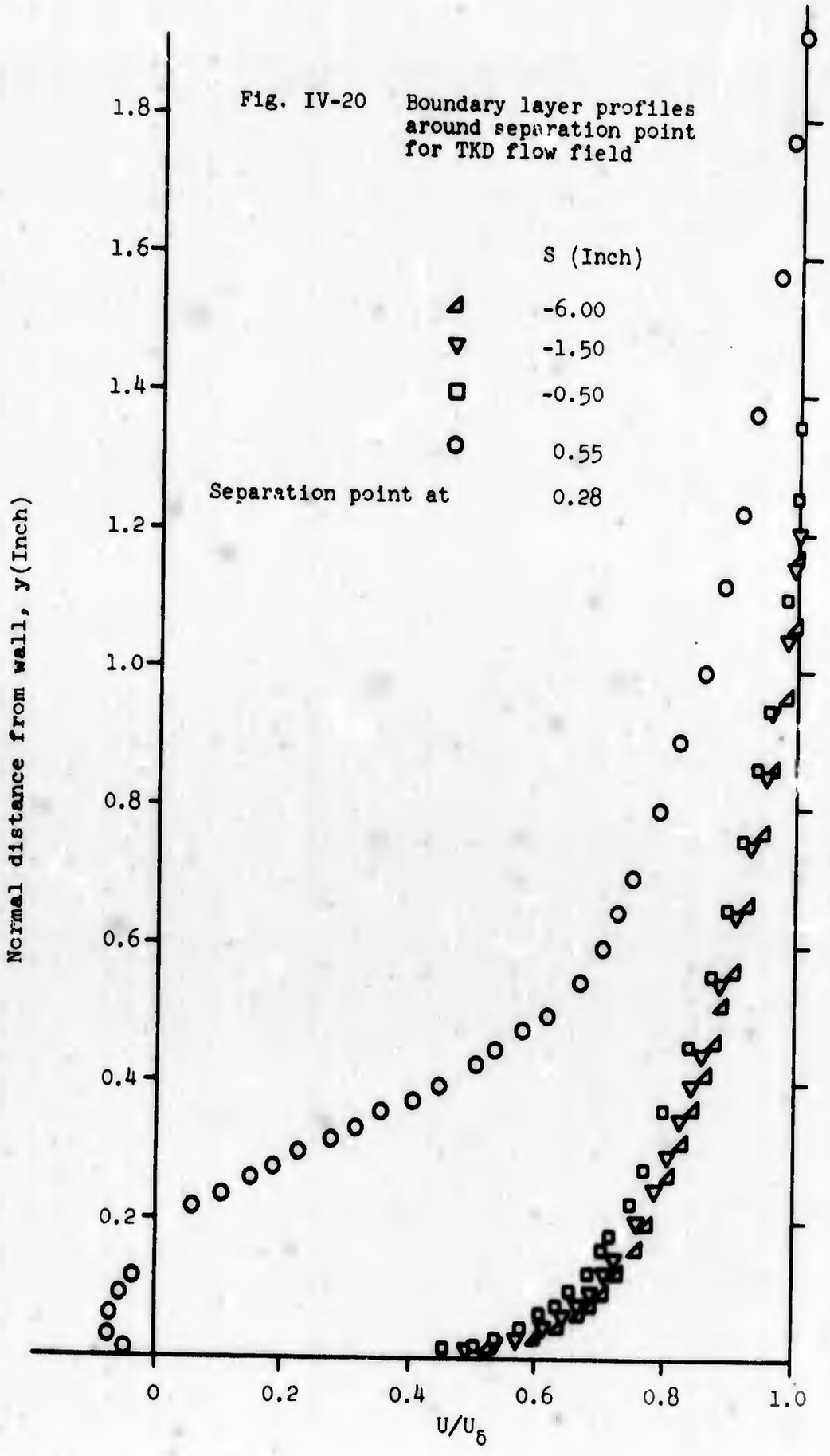

Fig. IV-20 Boundary layer profiles around separation point for TKD flow field

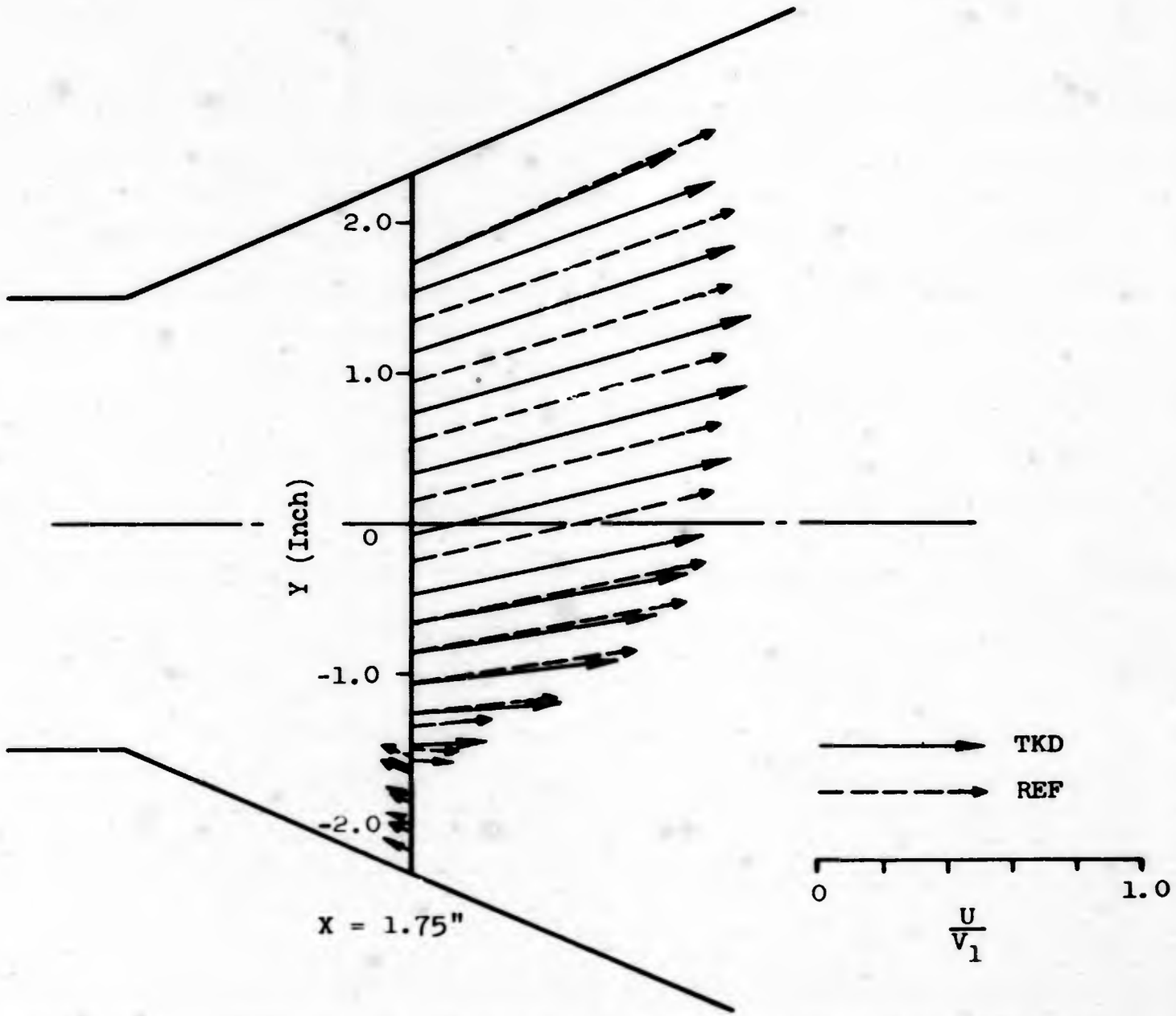

Fig. IV-21 Comparison of velocity/inlet average velocity, U/V_1 , at X = 1.75" for TKD and REF flow fields

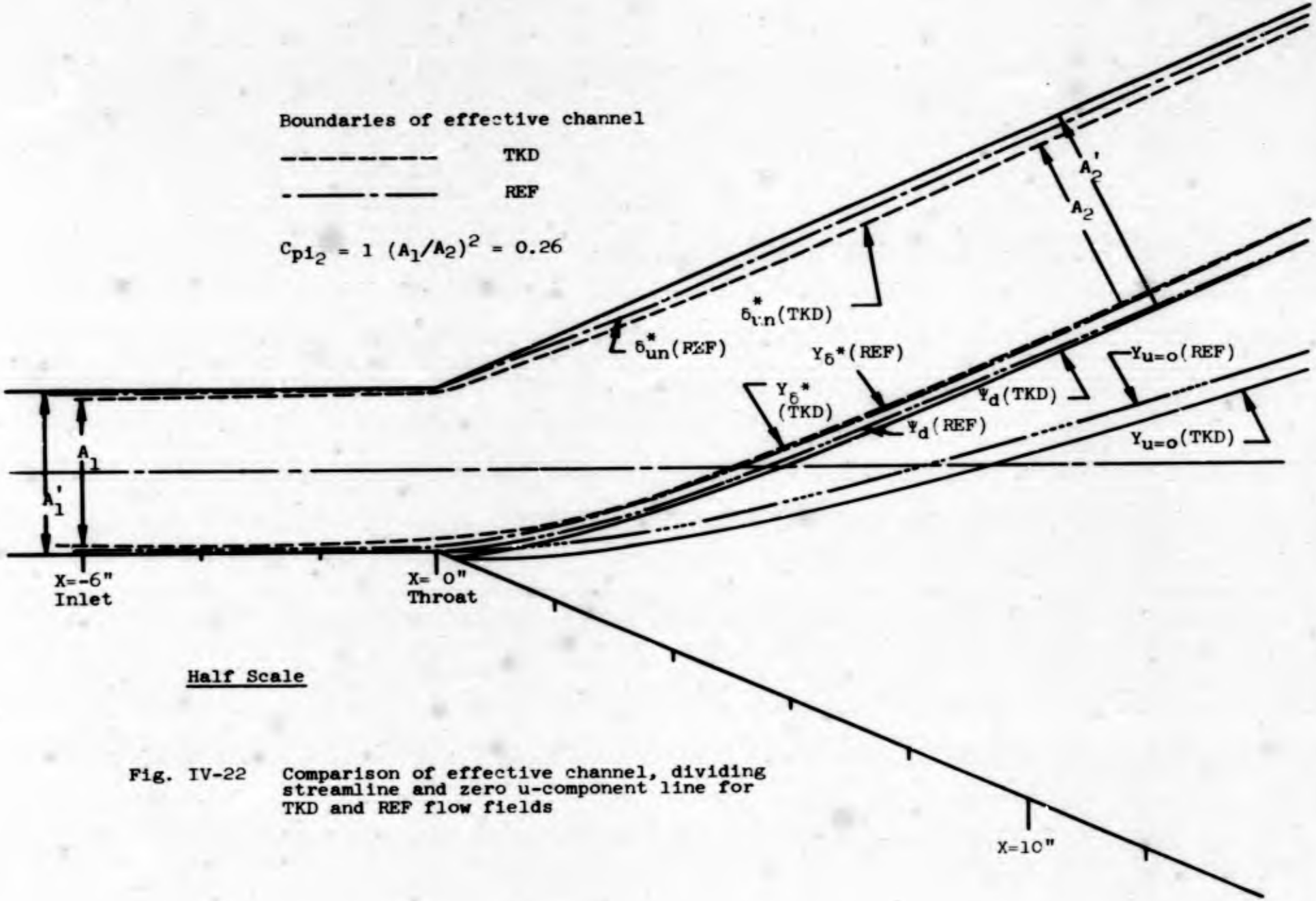

Fig. IV-22 Comparison of effective channel, dividing streamline and zero u-component line for TKD and REF flow fields

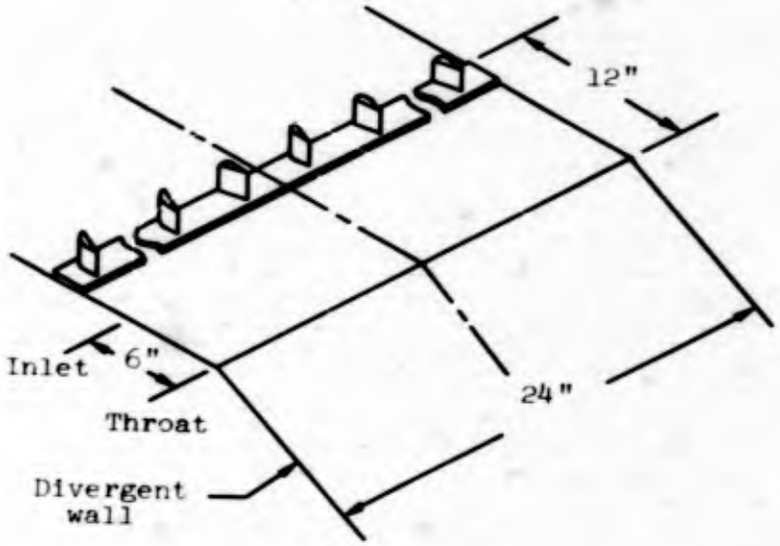

Location of vortex generator on side wall

Fig. IV-23 Dimensions and arrangement of vortex generator

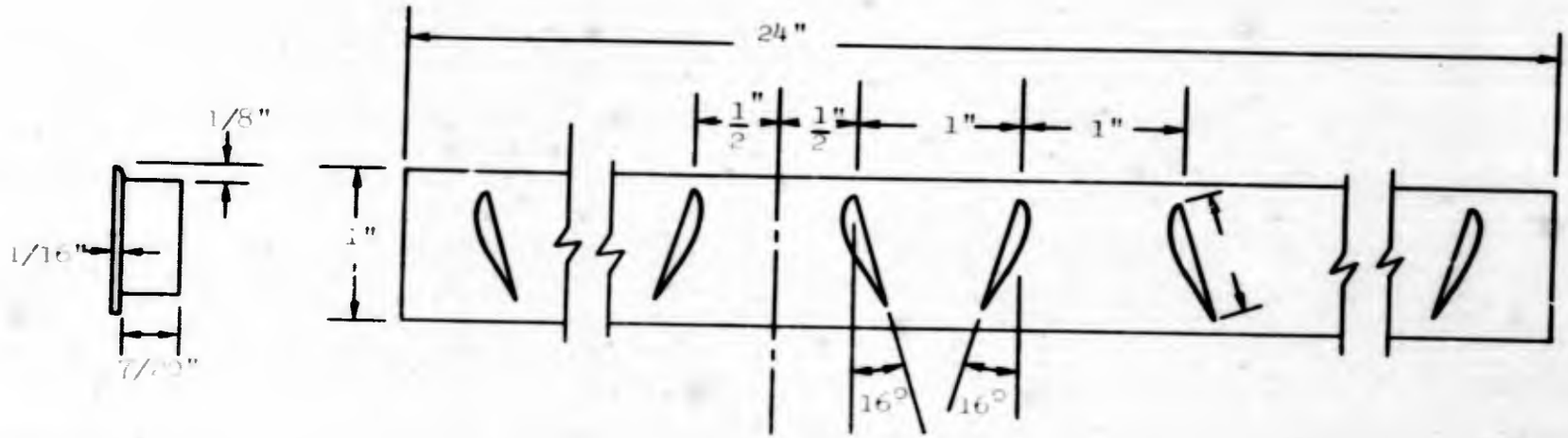

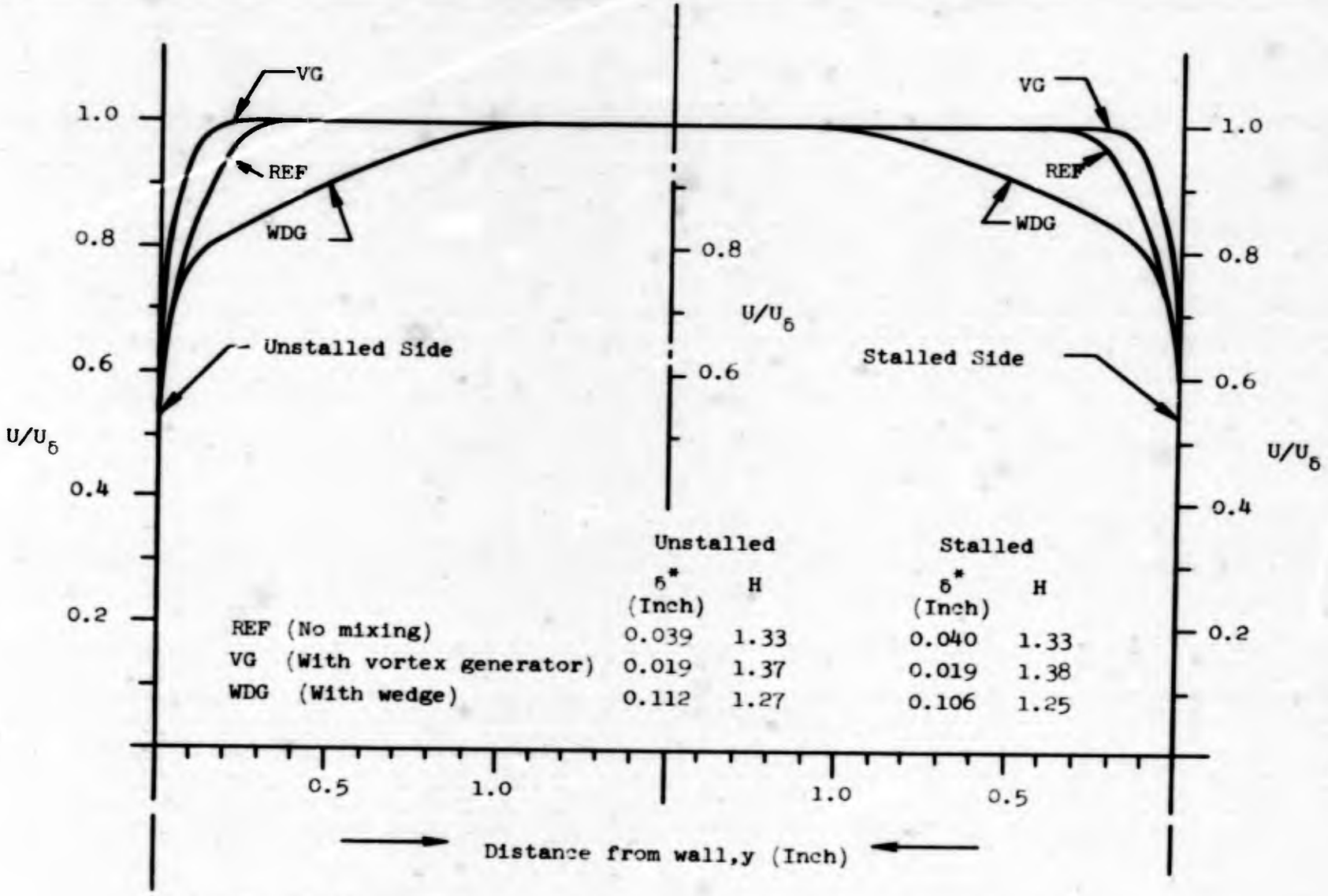

	Unstalled		Stalled	
	δ^* (Inch)	H	δ^* (Inch)	H
REF (No mixing)	0.039	1.33	0.040	1.33
VG (With vortex generator)	0.019	1.37	0.019	1.38
WDG (With wedge)	0.112	1.27	0.106	1.25

Fig. IV-24 Comparison of inlet velocity profile with and without turbulent mixing in the reference flow field

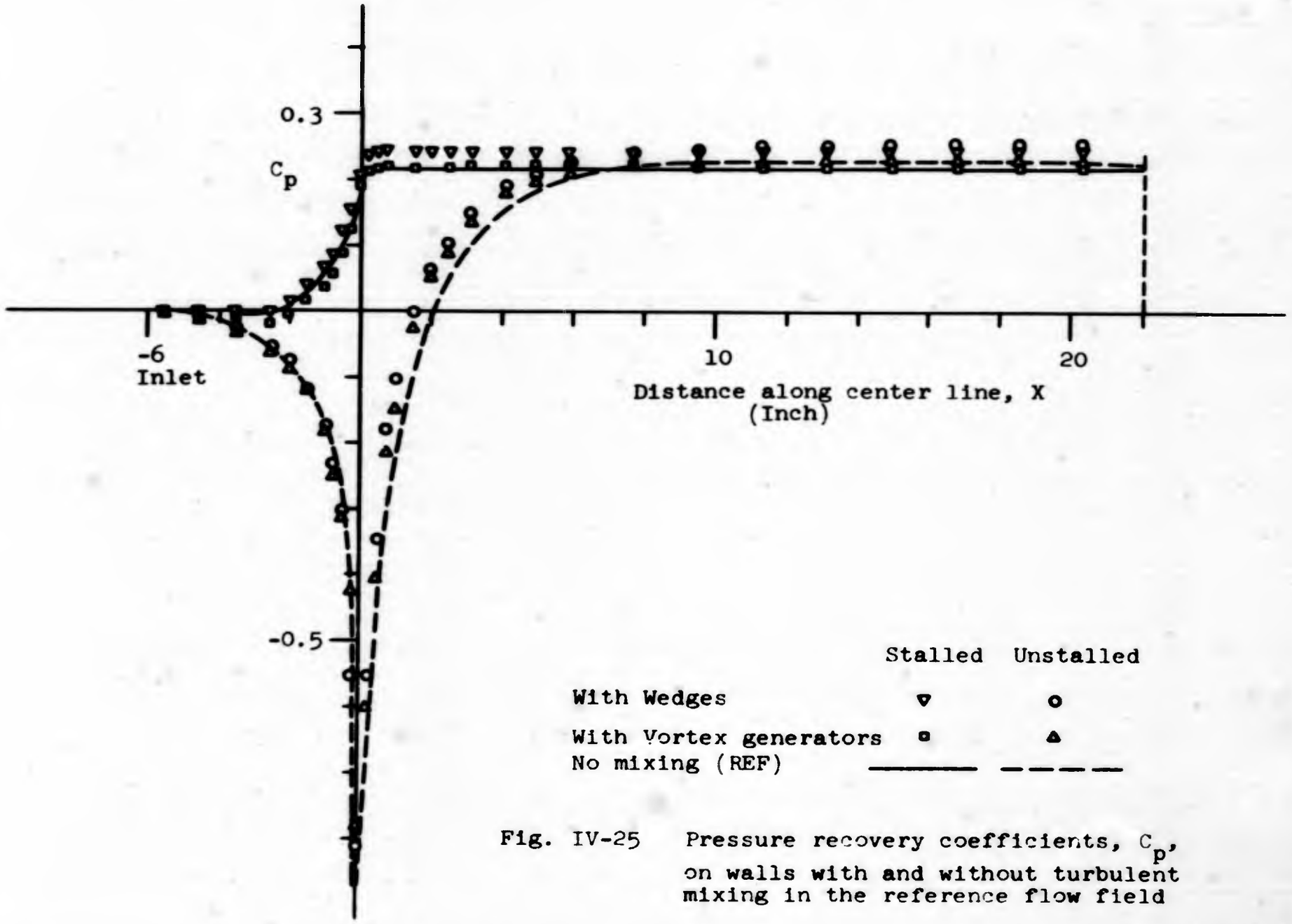

Fig. IV-25 Pressure recovery coefficients, C_p, on walls with and without turbulent mixing in the reference flow field

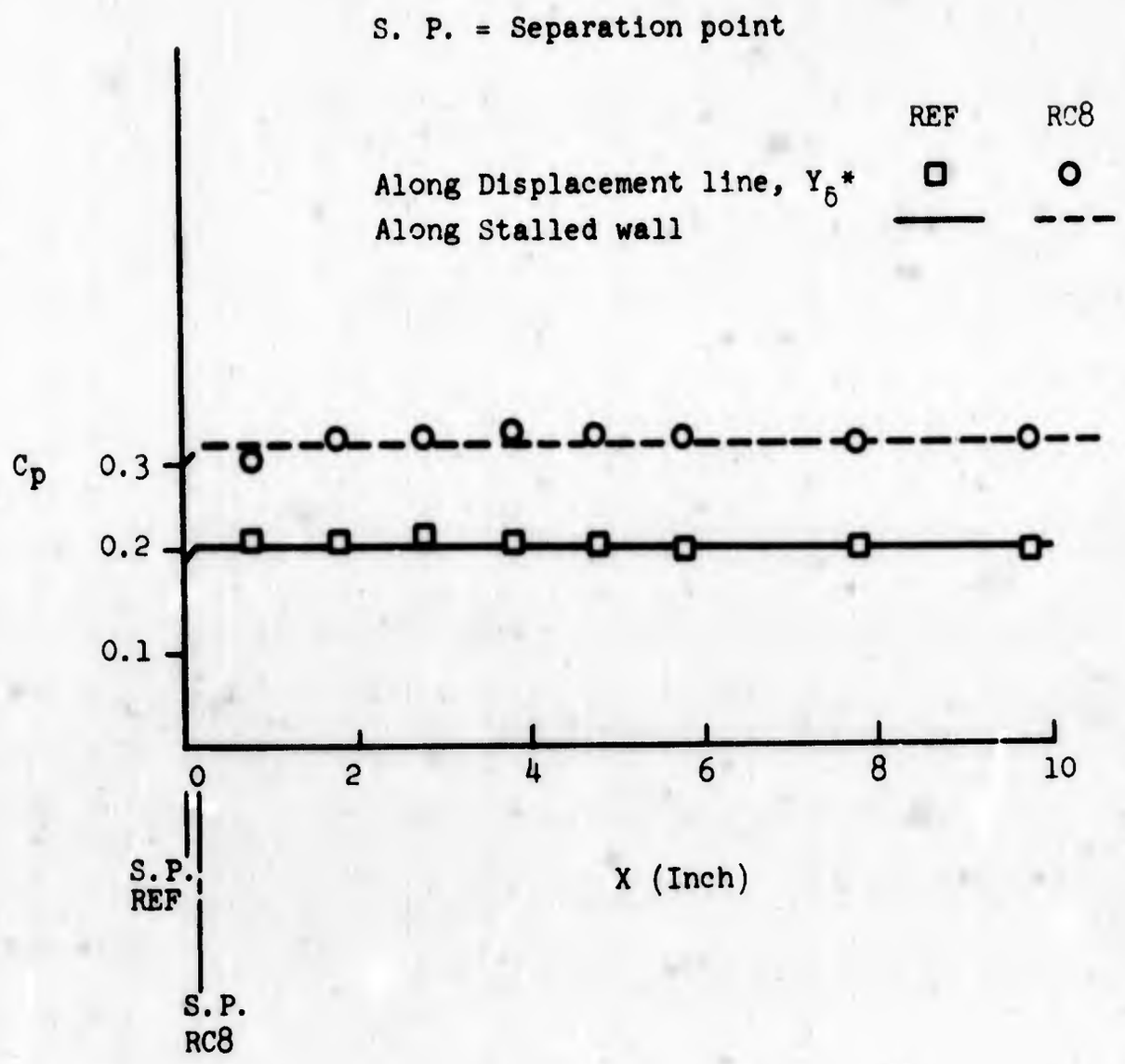

Fig. V-1 Pressure recovery coefficients along stalled wall and displacement line for RC8 and REF flow fields

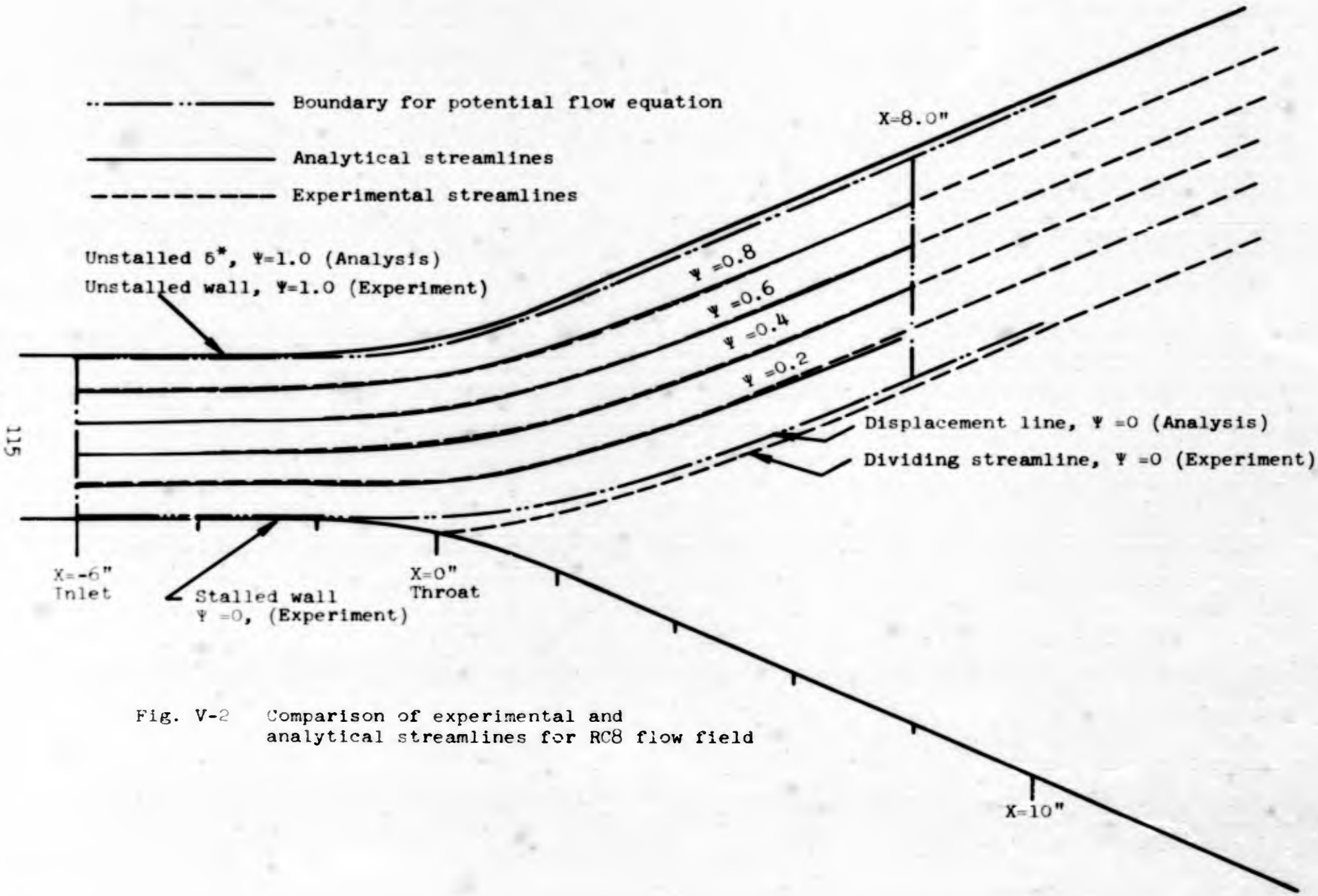

Fig. V-2 Comparison of experimental and analytical streamlines for RC8 flow field

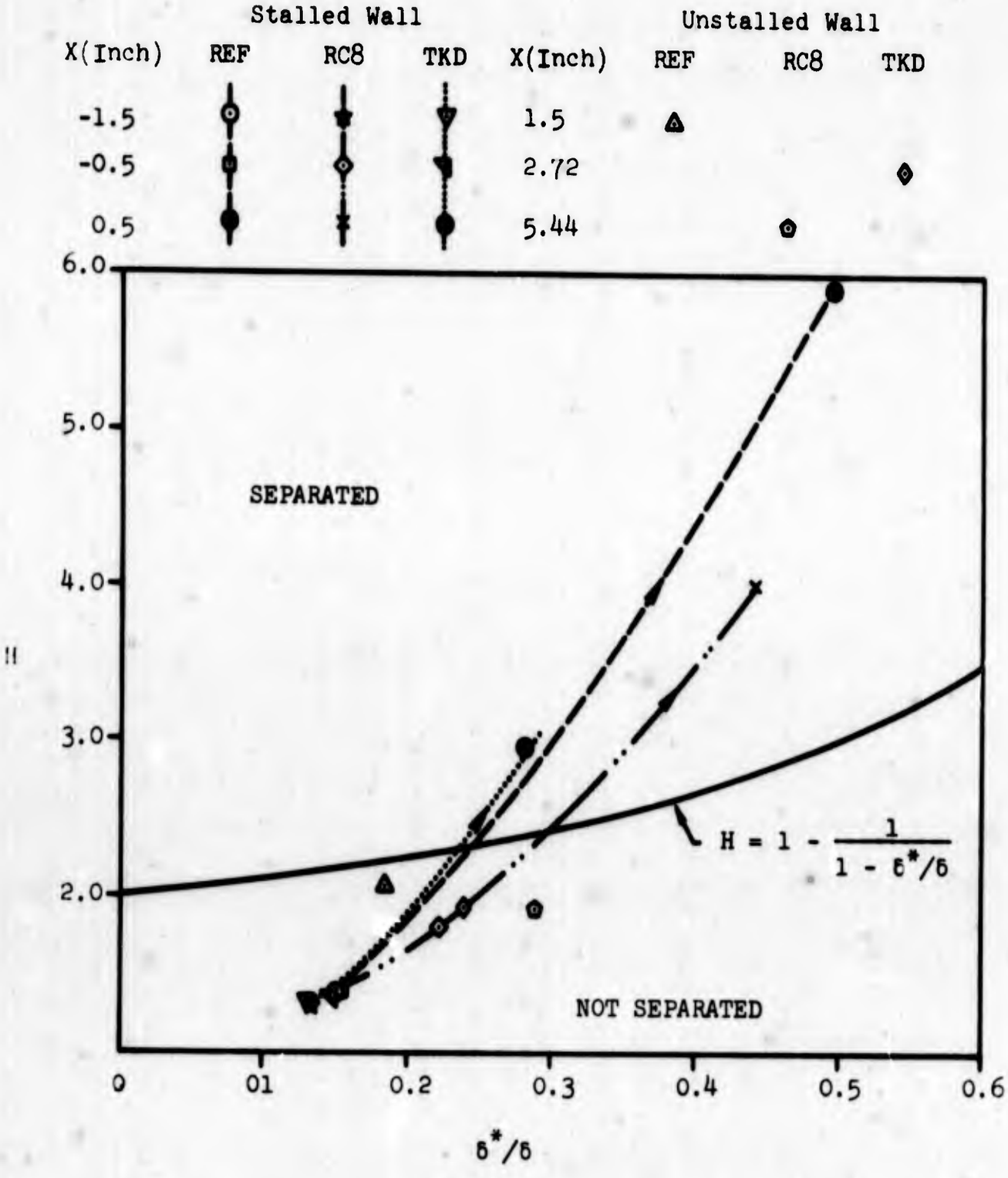

Fig. V-3 Comparison of boundary layer parameters at several experimental stations with the separation criterion of Sandborn [1959]

Fig. V-4 Comparison of experimental and calculated values of δ^* and H on unstalled wall for RC8 flow field

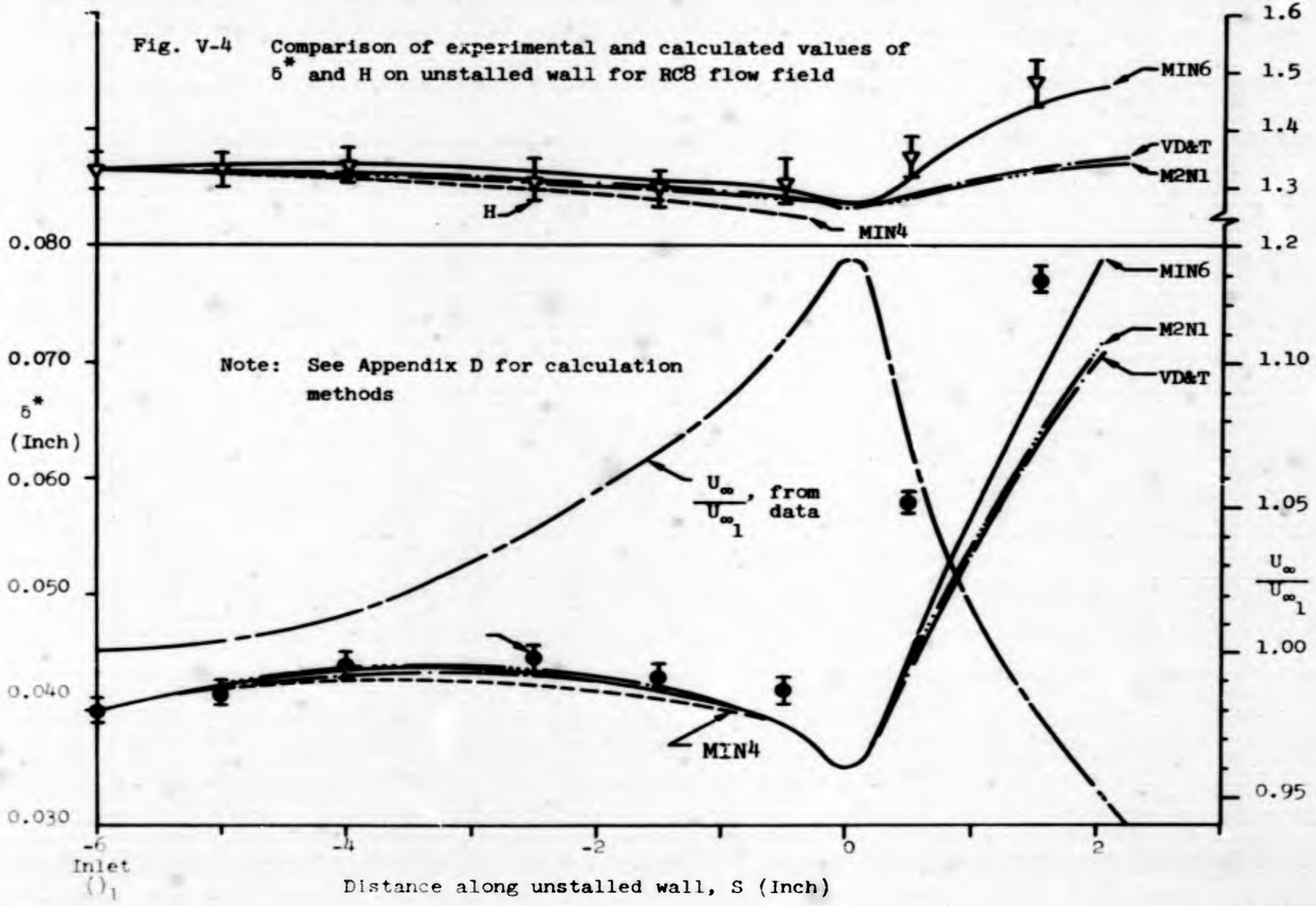

Fig. V-5 Comparison of experimental and calculated values of δ^* and H on stalled wall for RC8 flow field

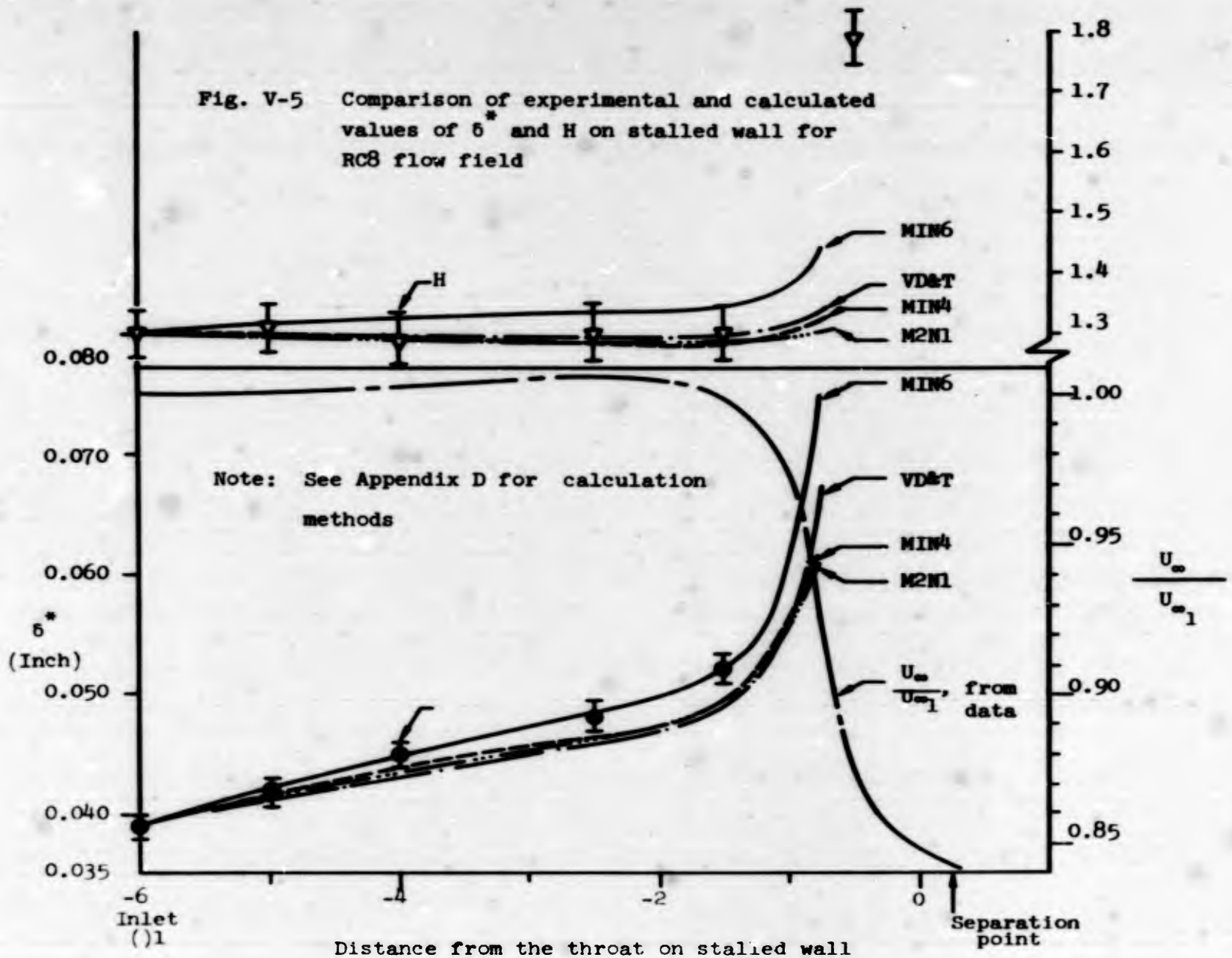

REFERENCES

Chang, S. C. [1966], "Velocity Distribution in the Separated Flow Behind a Wedge Shaped Model Hill," Tech. Report, Fluid Mechanics Program, College of Engineering, Colorado State University.

Chapman, D. R. [1951], "An Analysis of Base Pressure at Supersonic Velocities and Comparison with Experiment," NACA Report 1051, 1951.

Clauser, F. H. [1954], "Turbulent Boundary Layers in Adverse Pressure Gradients," Journal of the Aeronautical Sciences, February 1954.

Cocanower, A. B., Kline, S. J., and Johnston, J. P. [1965], "A Unified Method for Predicting the Performance of Subsonic Diffusers of Several Geometries," Report PD-10, Thermosciences Div., Mech. Engrg. Dept., Stanford University, May 1965.

Copp, M. R. [1951], "Effects of Inlet Wall Contour on the Pressure Recovery of a 10° 10-inch I.D. Conical Diffuser," NACA RM L51E11a, September 1951.

Feil, O. G. [1962], Vane Systems for Very Wide Angle Subsonic Diffuser," Report PL-7, Dept. of Mech. Engrg., Stanford University, 1962.

Fox, L. [1962], Numerical Solution of Ordinary and Partial Equations, Addison Wesley International Series.

Fox, R. W. and Kline, S. J. [1962], "Flow Regime Data and Design Methods for Curved Subsonic Diffusers," TASME, Journal of Basic Engineering, Vol. 84, Series D, September 1962.

Kline, S. J. [1963], "Flow Visualization," No. K-4, Educational Services Incorporated, 39 Chapel Street, Newton, Massachusetts.

Kline, S. J. [1965], "Flow Regimes in Subsonic Diffusers," Movie loop, FM49, Encyclopaedia Britannica film loop.

Kline, S. J. and McClintoch, F. A. [1953], "The Description of Uncertainty in Single Sample Experiments," Mech. Engrg., January 1953.

McDonald, A. T. [1962], "Evaluation of Incompressible Turbulent Boundary Layer Prediction Methods Applied to Diffusers," Masters Thesis, School of Mechanical Engineering, Purdue University, June 1962.

Moore, C. A. and Kline, S. J. [1958], "Some Effects of Vanes and of Turbulence on Two-Dimensional Wide-Angle Subsonic Diffusers," NACA TN4080, June 1958.

Moses, H. L., Chappel, J. R. and Goldberg, T. [1965], "Boundary Layer Separation in Internal Flow," Report No. 81, Gas Turbine Laboratory, MIT.

Nice, G. R., Teng, W. Y., and Moses, H. L. [1966], "Separation of Turbulent Incompressible Flow From a Curved Backward-Facing Step," MIT, Gas Turbine Laboratory, Report No. 87, October 1966.

Reneau, L. R., Johnston, J. P., and Kline, S. J. [1964], "Performance and Design of Straight, Two-Dimensional Diffusers," Report PD-8, Thermosciences Div., Mech. Engrg. Dept., Stanford University, September 1964.

Robertson, J. M. [1965], Hydrodynamics in Theory and Application, Prentice Hall, 1965.

Rotta, J. C. [1962], "Turbulent Boundary Layers in Incompressible Flow," Progress in Aeronautical Sciences, Vol. 2, Pergamon Press, Inc., 1962.

Rotta, J. C. [1965], "Critical Review of Existing Methods for Calculating the Development of Turbulent Boundary Layer," Proceedings of Symposium on Fluid Mechanics of Internal Flow, Edited by G. Sovran, Elsevier Publishing Co., 1967.

Sagi, C. J., Johnston, J. P., and Kline, S. J. [1965], "The Design and Performance of Two-Dimensional Curved Subsonic Diffusers," Report PD-9, Thermosciences Div., Mech. Engrg. Dept., Stanford University, May 1965.

Sandborn, V. A. [1959], "An Equation for the Mean Velocity Distribution of Boundary Layers," NASA Memo. 2-5-59 E, February 1959.

Schraub, F. A. and Kline, S. J. [1965], "A Study of the Structure of the Turbulent Boundary Layer With and Without Longitudinal Pressure Gradients," Report MD-12, Thermosciences Div., Mech. Engrg. Dept., Stanford University, March 1965.

Shapiro, A. H. [1963], "Design of Tuft for Flow Visualization," AIAA Volume 1, 1963.

Sovran, G. and Klomp, E. D. [1965], "Experimentally Determined Optimum Geometries for Rectilinear Diffusers with Rectangular, Conical or Annular Cross-Section," Research Publication GMR-511, Research Labs., General Motors Corp., Nov. 16, 1965. (Or Proceedings of General Motors Research Laboratory Symposium, The Fluid Mechanics of Integral Flow, Elsevier Publishing Co., 1967).

Taylor, H. D. [1948], "Application of Vortex Generator Mixing Principle to Diffusers - Concluding Report," Report R-15064-5, Research Department, United Aircraft Corporation.

Todd, K. W. [1949], "Some Developments in Instrumentation for Air Flow Analysis," Proc. I. Mech. E. 1949, Vol. 160.

Valentine, H. R. [1961], Applied Hydrodynamics, Butterworths and Co., London.

VanSant, J. H., Jr. and Larson, M. B. [1965], "Convection Heat Transfer in Separated Regions - Subsonic Diffusers," TASME, Journal of Heat Transfer, November 1966. Also PhD Thesis, Oregon State University, August 1964.

Table 1
Pressure recovery coefficients and velocities inside REF flow field

X = -4.25"

Y (Inches)	C_p	$\frac{U}{V_1}$	α (Degrees)
0.94	-0.03	1.03	-0.2
0.54	-0.02	1.03	0.0
0.14	-0.01	1.03	0.0
-0.26	-0.00	1.03	0.2
-0.66	0.00	1.03	0.2
-1.06	0.01	1.03	0.2

X = -3.25"

Y (Inches)	C_p	$\frac{U}{V_1}$	α (Degrees)
0.94	-0.04	1.03	-0.2
0.74	-0.03	1.03	-0.1
0.34	-0.02	1.03	0.1
-0.06	-0.01	1.03	0.3
-0.46	-0.00	1.03	0.4
-0.86	0.01	1.02	0.4

X = -2.25"

Y (Inches)	C_p	$\frac{U}{V_1}$	α (Degrees)
0.94	-0.08	1.06	0.0
0.74	-0.07	1.06	0.2
0.34	-0.05	1.05	0.8
-0.06	-0.03	1.05	1.0
-0.46	-0.01	1.04	1.0
-0.96	-0.00	1.03	0.8

X = -1.25"

Y (Inches)	C_p	$\frac{U}{V_1}$	α (Degrees)
0.74	-0.12	1.08	2.0
0.34	-0.08	1.06	2.0
-0.06	-0.04	1.05	2.2
-0.46	-0.00	1.03	2.0
-0.86	0.03	1.02	1.8
-1.05	0.03	1.01	1.4

Table 1 (Continued)
Pressure recovery coefficients and velocities inside REF flow field

X = -0.25

Y (Inches)	C_p	$\frac{U}{V_1}$	α (Degrees)
0.74	-0.16	1.10	6.2
0.54	-0.14	1.09	5.8
0.34	-0.10	1.07	5.4
0.00	-0.03	1.04	5.2
-0.26	0.01	1.03	5.2
-0.46	0.04	1.01	4.8
-0.66	0.08	0.99	4.4
-0.94	0.13	0.97	3.8

X = 0.75"

Y (Inches)	C_p	$\frac{U}{V_1}$	α (Degrees)
1.14	-0.21	1.11	14.8
0.74	-0.13	1.08	13.0
0.34	-0.05	1.04	11.4
-0.06	0.25	1.01	10.0
-0.46	0.09	0.98	9.2
-0.66	0.12	0.96	8.5
-0.86	0.16	0.94	8.0
-1.06	0.19	0.88	7.2
-1.26	0.22	0.71	6.0
-1.36	0.22	0.59	5.0
-1.46	0.21	0.37	3.0
-1.56	0.20	0.15	1.0
-1.60	0.21	0.07	166.0

Table 1 (Continued)
Pressure recovery coefficients and velocities inside REF flow field

X = 1.75"

Y (Inches)	C_p	$\frac{U}{V_1}$	α (Degrees)
1.74	-0.10	1.01	25.0
1.34	-0.05	1.04	19.6
0.94	-0.01	1.02	17.8
0.54	0.03	1.01	16.2
0.14	0.08	0.98	15.0
-0.26	0.13	0.96	13.8
-0.46	0.15	0.94	13.2
-0.66	0.18	0.92	12.0
-0.86	0.20	0.87	10.5
-0.96	0.22	0.80	9.7
-1.06	0.23	0.71	8.9
-1.16	0.22	0.59	7.9
-1.26	0.21	0.44	6.7
-1.36	0.22	0.26	5.0
-1.51	0.21	0.11	-5.0
-1.56	0.21	0.06	158.0
-1.66	0.21	0.07	167.0
-1.86	0.21	0.07	161.0
-2.06	0.21	0.07	155.0

X = 2.75"

Y (Inches)	C_p	$\frac{U}{V_1}$	α (Degrees)
1.94	0.03	1.00	23.8
1.54	0.05	0.99	21.6
1.14	0.08	0.98	20.4
0.74	0.10	0.97	19.4
0.34	0.13	0.96	18.4
-0.06	0.16	0.94	17.6
-0.26	0.18	0.93	16.6
-0.46	0.20	0.90	15.4
-0.56	0.20	0.87	14.5
-0.66	0.22	0.81	13.5
-0.86	0.23	0.62	10.9
-1.06	0.22	0.39	7.9
-1.16	0.21	0.27	4.8
-1.26	0.21	0.18	-1.0
-1.36	0.21	0.11	-7.0
-1.41	0.21	0.06	149.0
-1.46	0.21	0.06	158.0
-1.66	0.21	0.06	169.0
-1.86	0.21	0.06	165.0
-2.06	0.21	0.06	162.0
-2.26	0.21	0.06	159.0
-2.46	0.21	0.06	156.0

Table 1 (Continued)
Pressure recovery coefficients and velocities inside REF flow field

X = 3.75"				X = 4.75"			
Y (Inches)	C_p	$\frac{U}{V_1}$	α (Degrees)	Y (Inches)	C_p	$\frac{U}{V_1}$	α (Degrees)
2.54	0.10	0.88	24.8	2.94	0.14	0.86	25.0
2.14	0.11	0.96	24.2	2.74	0.15	0.91	25.0
1.94	0.12	0.96	23.2	2.44	0.15	0.93	24.5
1.64	0.13	0.96	22.7	2.14	0.16	0.93	23.9
1.34	0.14	0.95	22.4	1.84	0.16	0.93	23.4
1.04	0.15	0.95	21.6	1.54	0.17	0.93	23.0
0.74	0.16	0.94	21.2	1.24	0.17	0.93	22.6
0.44	0.18	0.93	20.6	0.94	0.18	0.93	22.3
0.14	0.19	0.92	19.7	0.74	0.19	0.92	21.9
-0.16	0.20	0.88	18.2	0.54	0.19	0.92	21.4
-0.36	0.20	0.77	16.2	0.34	0.20	0.89	20.6
-0.56	0.21	0.61	13.8	0.14	0.20	0.81	19.4
-0.76	0.22	0.43	11.6	-0.06	0.20	0.68	17.8
-0.96	0.21	0.24	8.3	-0.26	0.21	0.55	16.0
-1.16	0.21	0.15	4.2	-0.46	0.21	0.41	14.0
-1.16	0.21	0.10	-1.8	-0.66	0.20	0.26	10.6
-1.26	0.21	0.06	154.0	-0.86	0.20	0.13	3.0
-1.36	0.21	0.06	164.0	-0.96	0.21	0.09	-4.0
-1.76	0.21	0.06	172.0	-1.06	0.21	0.06	157.0
-2.26	0.21	0.06	168.0	-1.26	0.21	0.09	172.0
-2.66	0.21	0.05	163.0				
-3.06	0.21	0.04	155.0				

Table 1 (Continued)
Pressure recovery coefficients and velocities inside REF flow field

X = 4.75"
(Continued)

Y (Inches)	C_p	$\frac{U}{V_1}$	α (Degrees)
-1.66	0.21	0.07	174.0
-2.06	0.21	0.06	174.0
-2.36	0.21	0.05	171.0
-2.66	0.21	0.04	169.0
-3.06	0.21	0.04	167.0
-3.46	0.21	0.04	159.0

X = 5.75"

Y (Inches)	C_p	$\frac{U}{V_1}$	α (Degrees)
3.34	0.18	0.87	25.0
3.14	0.18	0.91	25.0
2.74	0.19	0.92	24.6
2.34	0.19	0.92	24.4
1.94	0.19	0.92	23.8
1.64	0.19	0.92	23.6
1.34	0.19	0.92	23.4
1.14	0.20	0.92	23.0
0.94	0.20	0.91	22.4
0.74	0.20	0.87	21.0

X = 5.75"
(Continued)

Y (Inches)	C_p	$\frac{U}{V_1}$	α (Degrees)
0.54	0.20	0.78	20.2
0.34	0.20	0.67	19.2
0.14	0.21	0.55	18.2
-0.06	0.21	0.43	16.0
-0.16	0.21	0.36	14.4
-0.36	0.21	0.24	11.7
-0.46	0.21	0.19	9.6
-0.56	0.21	0.14	6.6
-0.66	0.21	0.10	1.2
-0.73	0.21	0.08	-1.0
-0.81	0.21	0.06	158.0
-1.06	0.21	0.07	175.0
-1.36	0.21	0.07	178.0
-1.96	0.21	0.06	177.0
-2.56	0.21	0.05	178.0
-3.16	0.21	0.04	175.0
-3.76	0.21	0.03	165.0

Table 1 (Continued)
Pressure recovery coefficients and velocities inside REF flow field

X = 7.75"

Y (Inches)	C_p	$\frac{U}{V_1}$	α (Degrees)
4.70	0.21	0.68	25.0
4.30	0.21	0.83	25.0
3.90	0.21	0.90	25.0
3.50	0.21	0.91	24.8
3.10	0.21	0.91	24.6
2.70	0.21	0.91	24.4
2.30	0.21	0.91	24.2
2.10	0.21	0.91	24.0
1.90	0.21	0.89	23.8
1.70	0.21	0.84	23.6
1.50	0.21	0.77	23.2
1.30	0.21	0.69	22.8
1.10	0.21	0.60	22.0
0.90	0.21	0.50	21.0
0.70	0.21	0.40	19.4
0.50	0.21	0.30	16.8
0.30	0.20	0.23	13.8
0.10	0.20	0.13	10.0
-0.10	0.20	0.09	3.0
-0.15	0.20	0.08	-1.0

X = 7.75"
(Continued)

Y (Inches)	C_p	$\frac{U}{V_1}$	α (Degrees)
-0.20	0.20	0.06	153.0
-0.40	0.21	0.07	167.0
-0.80	0.21	0.08	177.0
-1.20	0.21	0.08	179.0
-1.60	0.21	0.07	182.0
-2.00	0.21	0.06	182.0
-2.40	0.21	0.06	183.0
-2.80	0.21	0.06	185.0
-3.20	0.21	0.04	188.0
-3.60	0.21	0.04	190.0
-4.00	0.21	0.02	193.0
-4.40	0.21	0.01	187.0

Table 1 (Continued)
Pressure recovery coefficients and velocities inside REF flow field

X = 9.75"

Y (Inches)	C_p	$\frac{U}{V_1}$	α (Degrees)
5.50	0.22	0.75	25.0
5.10	0.22	0.85	25.0
4.70	0.22	0.90	25.0
4.30	0.22	0.91	24.6
3.90	0.22	0.91	24.5
3.50	0.21	0.91	24.4
3.30	0.21	0.91	24.2
3.10	0.20	0.90	24.0
2.90	0.20	0.88	23.8
2.70	0.20	0.83	23.4
2.50	0.20	0.78	23.0
2.30	0.20	0.70	22.6
2.10	0.20	0.63	22.0
1.90	0.20	0.56	21.4
1.70	0.20	0.49	20.8
1.50	0.20	0.40	19.8
1.30	0.20	0.31	18.0
1.10	0.20	0.24	16.0
0.90	0.20	0.17	12.4
0.70	0.20	0.12	9.2

X = 9.75"
(Continued)

Y (Inches)	C_p	$\frac{U}{V_1}$	α (Degrees)
0.50	0.20	0.08	4.0
0.40	0.20	0.06	151.0
0.30	0.20	0.07	161.0
0.10	0.20	0.07	171.0
-0.30	0.21	0.08	179.0
-0.70	0.21	0.09	181.0
-1.10	0.21	0.08	180.0
-1.50	0.21	0.08	181.0
-1.90	0.21	0.07	182.0
-2.30	0.21	0.07	183.0
-2.70	0.21	0.06	186.0
-3.10	0.21	0.04	189.0
-3.50	0.21	0.04	194.0
-3.90	0.21	0.03	201.0
-4.30	0.21	0.02	215.0
-4.70	0.21	0.02	219.0
-5.10	0.21	0.02	225.0

Table 1 (Continued)
Pressure recovery coefficients and velocities inside REF flow field

X = 11.75"

Y (Inches)	C_p	$\frac{U}{V_1}$	α (Degrees)
6.60	0.22	0.70	25.0
6.20	0.22	0.81	25.0
5.80	0.22	0.88	25.0
5.40	0.22	0.91	24.8
5.20	0.22	0.91	24.8
4.80	0.22	0.91	24.6
4.40	0.22	0.90	24.4
4.00	0.21	0.88	23.8
3.80	0.21	0.85	23.4
3.60	0.21	0.81	23.0
3.40	0.20	0.76	22.6
3.10	0.20	0.76	22.6
2.90	0.20	0.60	21.4
2.70	0.20	0.52	20.8
2.50	0.20	0.47	20.0
2.30	0.20	0.39	18.2
2.10	0.20	0.33	17.2
1.90	0.20	0.26	15.8
1.70	0.20	0.21	14.4
1.50	0.20	0.16	12.7

X = 11.75"
(Continued)

Y (Inches)	C_p	$\frac{U}{V_1}$	α (Degrees)
1.30	0.20	0.10	9.0
1.10	0.20	0.07	3.0
1.00	0.20	0.06	-6.0
0.90	0.20	0.06	161.0
0.70	0.21	0.07	171.0
0.50	0.21	0.08	176.0
0.30	0.21	0.08	179.0
-0.10	0.21	0.09	179.0
-0.50	0.21	0.09	179.0
-0.90	0.21	0.08	178.0
-1.30	0.21	0.08	179.0
-1.70	0.21	0.08	179.0
-2.10	0.21	0.08	179.0
-2.50	0.21	0.07	179.0
-2.90	0.21	0.06	182.0
-3.33	0.21	0.05	185.0
-3.70	0.21	0.04	191.0
-4.10	0.21	0.02	194.0
-4.50	0.21	0.02	201.0
-4.90	0.21	0.02	215. ±10

Table 1 (Continued)
Pressure recovery coefficients and velocities inside REF flow field

X = 11.75" (Continued)

Y (Inches)	C_p	$\frac{U}{V_1}$	α (Degrees)
-5.30	0.21	0.01	119.+20
-5.70	0.21	0.02	-21.0
-6.10	0.21	0.02	-21.0
-6.50	0.21	0.02	-21.0

X = 13.75"

7.10	0.22	0.82	25.0
6.70	0.22	0.88	25.0
6.30	0.22	0.91	25.0
5.70	0.22	0.91	24.5
5.30	0.21	0.91	24.0
5.10	0.21	0.89	23.8
4.90	0.20	0.86	23.6
4.70	0.20	0.83	23.4
4.50	0.20	0.79	23.2
4.30	0.20	0.74	23.0
4.10	0.20	0.69	22.6
3.90	0.20	0.64	22.2
3.70	0.20	0.57	21.8
3.50	0.20	0.51	21.0
3.30	0.20	0.45	19.8

X = 13.75" (Continued)

Y (Inches)	C_p	$\frac{U}{V_1}$	α (Degrees)
3.10	0.20	0.39	18.6
2.90	0.20	0.34	17.4
2.70	0.20	0.29	16.3
2.50	0.20	0.23	15.0
2.30	0.20	0.18	13.8
2.10	0.20	0.13	12.4
1.90	0.21	0.10	10.5
1.70	0.21	0.06	4.0
1.60	0.21	0.05	150.0
1.50	0.21	0.06	156.0
1.30	0.21	0.07	167.0
0.90	0.21	0.08	174.0
0.50	0.21	0.08	175.0
0.10	0.21	0.08	174.0
-0.30	0.21	0.08	174.0
-0.70	0.21	0.09	173.0
-1.10	0.21	0.09	172.0
-1.50	0.21	0.09	172.0
-1.90	0.21	0.08	173.0
-2.30	0.21	0.08	172.0

Table 1 (Continued)
Pressure recovery coefficients and velocities inside REF flow field

X = 13.75"
(Continued)

Y (Inches)	C_p	$\frac{U}{V_1}$	α (Degrees)
-2.70	0.21	0.07	172.0
-3.10	0.21	0.06	174.0
-3.50	0.21	0.06	176.0
-3.90	0.21	0.04	179.0
-4.30	0.21	0.04	183.0
-4.70	0.21	0.02	184.0
-5.10	0.21	0.02	195.0
-5.50	0.21	0.02	190.0
-5.90	0.21	0.02	-10.0
-6.30	0.21	0.02	-9.0
-6.70	0.21	0.02	-15.0
-7.10	0.21	0.03	-17.0
-7.50	0.21	0.04	-20.0

X = 15.75"

8.30	0.22	0.75	25.0
8.10	0.22	0.79	25.0
7.70	0.22	0.86	25.0
7.30	0.22	0.89	25.0
6.90	0.22	0.90	24.0

X = 15.75"
(Continued)

Y (Inches)	C_p	$\frac{U}{V_1}$	α (Degrees)
6.50	0.21	0.90	24.3
6.30	0.21	0.89	24.2
6.10	0.20	0.87	24.0
5.90	0.20	0.85	23.8
5.70	0.20	0.82	23.6
5.50	0.20	0.78	23.4
5.30	0.20	0.74	23.2
4.90	0.20	0.65	22.6
4.50	0.20	0.55	21.6
4.10	0.20	0.43	20.2
3.70	0.20	0.33	18.2
3.50	0.20	0.27	17.0
3.30	0.20	0.24	15.4
3.10	0.20	0.19	14.0
2.90	0.20	0.15	12.6
2.70	0.20	0.11	11.6
2.50	0.21	0.09	10.2
2.30	0.21	0.06	7.0
2.20	0.21	0.05	139.0
2.10	0.21	0.06	145.0

Table 1 (Continued)
Pressure recovery coefficients and velocities inside REF flow field

X = 15.75"
(Continued)

Y (Inches)	C_p	$\frac{U}{V_1}$	α (Degrees)
1.80	0.21	0.06	161.0
1.40	0.21	0.07	167.0
1.00	0.21	0.07	168.0
0.60	0.21	0.08	167.0
0.20	0.21	0.08	166.0
-0.20	0.21	0.08	165.0
-0.60	0.21	0.08	164.0
-1.00	0.21	0.08	164.0
-1.40	0.21	0.08	163.0
-1.80	0.21	0.09	163.0
-2.20	0.21	0.08	163.0
-2.60	0.21	0.08	163.0
-3.00	0.21	0.08	163.0
-3.40	0.21	0.08	163.0
-3.80	0.21	0.07	164.0
-4.20	0.21	0.05	165.0
-4.60	0.21	0.04	166.0
-5.00	0.21	0.04	171.0
-5.40	0.21	0.03	176.0
-5.80	0.21	0.02	177.0

X = 15.75"
(Continued)

Y (Inches)	C_p	$\frac{U}{V_1}$	α (Degrees)
-6.20	0.21	0.02	172.0
-6.60	0.21	0.02	-1.0
-7.00	0.21	0.02	-5.0
-7.40	0.21	0.02	-11.0
-7.80	0.21	0.02	-13.0
-8.20	0.21	0.03	-15.0
-8.60	0.21	0.03	-19.0

Table 2

Pressure recovery coefficients and velocities inside RC8 flow field

X = -4.25"

Y (Inches)	C_p	$\frac{U}{V_1}$	α (Degrees)
1.04	-0.03	1.03	-0.2
0.64	-0.02	1.03	-0.1
0.24	-0.01	1.03	-0.1
-0.16	-0.01	1.03	0.0
-0.56	-0.01	1.03	0.0
-0.76	-0.01	1.03	0.0
-0.96	-0.01	1.03	0.0

X = -3.25"

Y (Inches)	C_p	$\frac{U}{V_1}$	α (Degrees)
1.09	-0.04	1.05	-0.1
0.84	-0.04	1.05	-0.1
0.60	-0.03	1.04	0.1
0.34	-0.02	1.04	0.2
0.00	-0.01	1.04	0.2
-0.40	-0.01	1.04	0.2
-0.77	-0.01	1.03	0.6

X = -2.25"

Y (Inches)	C_p	$\frac{U}{V_1}$	α (Degrees)
1.04	-0.09	1.07	0.2
0.64	-0.06	1.05	0.6
0.24	-0.03	1.04	0.8
-0.16	-0.02	1.04	0.8
-0.56	0.00	1.03	0.8
-0.96	0.01	1.03	0.5

X = -1.25"

Y (Inches)	C_p	$\frac{U}{V_1}$	α (Degrees)
0.94	-0.12	1.08	2.6
0.54	-0.05	1.05	2.7
0.14	-0.01	1.03	2.5
-0.16	0.02	1.02	2.2
-0.56	0.05	1.00	1.4
-0.86	0.06	1.00	0.8
-0.93	0.06	1.00	0.6

Table 2 (Continued)
Pressure recovery coefficients and velocities inside RC8 flow field

X = -0.25"

Y (Inches)	C_p	$\frac{U}{V_1}$	α (Degrees)
1.24	-0.15	1.09	8.5
0.94	-0.08	1.07	7.6
0.54	0.00	1.03	6.8
0.14	0.06	1.00	5.8
0.00	0.08	0.99	5.6
-0.26	0.11	0.97	4.8
-0.66	0.16	0.95	3.6
-1.03	0.20	0.92	1.0

X = 0.75"

Y (Inches)	C_p	$\frac{U}{V_1}$	α (Degrees)
1.69	-0.05	0.92	16.0
1.49	-0.04	1.03	14.8
1.24	-0.02	1.03	13.6
0.94	0.04	1.00	12.6
0.64	0.08	0.98	11.6
0.34	0.12	0.96	10.6
0.04	0.16	0.94	9.8
-0.16	0.19	0.93	9.4
-0.36	0.22	0.92	9.0
-0.56	0.25	0.90	8.4

X = 0.75"
(Continued)

Y (Inches)	C_p	$\frac{U}{V_1}$	α (Degrees)
-0.76	0.28	0.89	8.0
-0.96	0.30	0.86	7.4
-1.16	0.32	0.80	6.6
-1.36	0.34	0.63	5.4
-1.56	0.33	0.36	4.0
-1.66	0.33	0.13	0.8
-1.80	0.33	0.05	168.0

X = 1.75"

Y (Inches)	C_p	$\frac{U}{V_1}$	α (Degrees)
1.93	0.11	0.93	21.2
1.53	0.12	0.96	18.4
1.13	0.14	0.95	16.8
0.73	0.18	0.93	15.4
0.33	0.21	0.91	14.4
-0.07	0.24	0.89	13.6
-0.47	0.28	0.87	12.6
-0.67	0.31	0.86	11.6
-0.77	0.32	0.84	11.0
-0.97	0.33	0.76	10.0

Table 2 (Continued)
Pressure recovery coefficients and velocities inside RC8 flow field

X = 1.75"
(Continued)

Y (Inches)	C_p	$\frac{U}{V_1}$	α (Degrees)
-1.17	0.34	0.60	9.0
-1.37	0.34	0.38	7.4
-1.47	0.33	0.29	6.6
-1.57	0.33	0.19	5.8
-1.67	0.33	0.11	3.0
-1.72	0.33	0.062	159.0
-1.87	0.33	0.072	161.6
-2.07	0.33	0.075	161.0

X = 2.75"

2.43	0.21	0.80	25.0
2.23	0.21	0.90	22.8
2.03	0.21	0.91	21.4
1.63	0.21	0.91	20.0
1.23	0.22	0.90	19.3
0.83	0.24	0.89	18.2
0.43	0.26	0.88	17.6
0.23	0.28	0.87	17.2
-0.17	0.30	0.86	16.0
-0.47	0.32	0.84	14.8

X = 2.75"
(Continued)

Y (Inches)	C_p	$\frac{U}{V_1}$	α (Degrees)
-0.67	0.33	0.77	13.6
-0.87	0.34	0.63	12.0
-1.07	0.34	0.48	10.4
-1.27	0.33	0.30	8.0
-1.47	0.33	0.17	2.0
-1.57	0.33	0.10	-4.0
-1.67	0.33	0.062	159.0
-1.87	0.33	0.071	164.0
-2.07	0.33	0.071	163.0
-2.27	0.33	0.067	160.0
-2.47	0.33	0.067	168.0

X = 3.75"

2.85	0.27	0.78	25.0
2.35	0.27	0.88	22.2
1.85	0.27	0.88	21.6
1.35	0.28	0.87	20.6
0.85	0.29	0.87	19.8

Table 2 (Continued)
Pressure recovery coefficients and velocities inside RC8 flow field

X = 3.75"
(Continued)

Y (Inches)	C_p	$\frac{U}{V_1}$	α (Degrees)
0.35	0.31	0.86	18.8
0.05	0.32	0.84	18.0
-0.25	0.33	0.77	16.8
-0.45	0.34	0.68	16.0
-0.65	0.34	0.58	15.0
-0.85	0.34	0.43	14.0
-1.05	0.33	0.27	12.0
-1.25	0.33	0.18	8.0
-1.40	0.33	0.14	4.0
-1.65	0.33	0.068	165.0
-1.90	0.33	0.079	169.0
-2.15	0.33	0.071	168.0
-2.40	0.33	0.062	166.0
-2.65	0.33	0.061	163.0
-2.90	0.33	0.057	158.0

X = 4.75"

Y (Inches)	C_p	$\frac{U}{V_1}$	α (Degrees)
3.33	0.29	0.72	25.0
3.03	0.29	0.86	25.0
2.63	0.29	0.86	23.0
2.23	0.29	0.86	22.4
1.83	0.30	0.86	21.8
1.43	0.30	0.86	21.6
1.03	0.31	0.86	21.0
0.63	0.32	0.83	20.4
0.23	0.33	0.77	19.6
-0.07	0.33	0.69	18.8
-0.27	0.33	0.59	18.0
-0.47	0.33	0.48	17.0
-0.67	0.33	0.36	15.4
-0.87	0.33	0.28	13.0
-0.97	0.33	0.21	10.0
-1.17	0.33	0.13	4.0
-1.27	0.33	0.077	156.0
-1.37	0.33	0.081	158.0
-1.57	0.33	0.087	164.0
-1.92	0.33	0.087	167.0

Table 2 (Continued)

Pressure recovery coefficients and velocities inside RC8 flow field

X = 4.75"

(Continued)

Y (Inches)	C_p	$\frac{U}{V_1}$	α (Degrees)
-2.17	0.33	0.082	167.0
-2.52	0.33	0.069	165.0
-2.92	0.33	0.069	162.0
-3.17	0.33	0.067	160.0
-3.42	0.33	0.062	157.0

X = 5.75"

3.83	0.31	0.65	25.0
3.63	0.31	0.81	25.0
3.43	0.31	0.85	24.4
3.03	0.31	0.86	23.6
2.63	0.31	0.86	23.2
2.23	0.31	0.86	22.8
1.83	0.32	0.86	22.6
1.43	0.32	0.85	22.0
1.23	0.32	0.85	21.6
1.03	0.32	0.82	21.0

X = 5.75"

(Continued)

Y (Inches)	C_p	$\frac{U}{V_1}$	α (Degrees)
0.83	0.32	0.80	20.4
0.63	0.32	0.77	19.8
0.43	0.32	0.72	19.2
0.23	0.32	0.63	18.4
0.03	0.32	0.54	17.6
-0.17	0.33	0.44	16.6
-0.37	0.33	0.35	15.0
-0.57	0.33	0.26	13.0
-0.77	0.33	0.18	9.0
-0.87	0.33	0.16	6.0
-1.07	0.33	0.09	1.0
-1.12	0.33	0.071	153.0
-1.17	0.33	0.079	161.0
-1.57	0.33	0.093	166.0
-1.97	0.33	0.094	168.0
-2.37	0.33	0.087	168.0
-2.77	0.33	0.075	167.0
-3.17	0.33	0.069	167.0
-3.57	0.33	0.062	163.0
-3.97	0.33	0.050	157.0

Table 2 (Continued)
Pressure recovery coefficients and velocities inside RC8 flow field

X = 7.75"

Y (Inches)	C_p	$\frac{U}{V_1}$	α (Degrees)
4.67	0.33	0.71	25.0
4.42	0.33	0.83	25.0
3.92	0.33	0.85	24.2
3.42	0.33	0.85	23.8
2.92	0.32	0.85	23.4
2.42	0.32	0.84	23.0
2.17	0.32	0.83	22.8
1.92	0.32	0.80	22.4
1.72	0.32	0.77	21.6
1.52	0.32	0.74	21.2
1.32	0.32	0.69	20.6
1.12	0.32	0.62	20.0
0.92	0.32	0.56	19.2
0.72	0.32	0.50	18.0
0.52	0.32	0.44	17.0
0.32	0.32	0.36	17.8
0.12	0.32	0.29	14.4
-0.08	0.32	0.21	13.0
-0.23	0.32	0.15	11.0
-0.43	0.32	0.13	8.0

X = 7.75"
(Continued)

Y (Inches)	C_p	$\frac{U}{V_1}$	α (Degrees)
-0.58	0.32	0.12	3.0
-0.68	0.32	0.09	0.0
-0.83	0.32	0.092	163.0
-1.08	0.32	0.098	168.0
-1.58	0.33	0.101	172.0
-2.08	0.33	0.101	174.0
-2.58	0.33	0.091	174.0
-3.08	0.33	0.082	176.0
-3.58	0.33	0.067	177.0
-4.08	0.33	0.057	175.0
-4.58	0.33	0.043	172.0

Table 2 (Continued)
Pressure recovery coefficients and velocities inside RC8 flow field

X = 9.75"

Y (Inches)	C_p	$\frac{U}{V_1}$	α (Degrees)
5.72	0.34	0.59	25.0
5.32	0.34	0.82	25.0
4.92	0.34	0.84	24.2
4.52	0.34	0.84	24.0
4.12	0.34	0.84	23.8
3.72	0.34	0.83	23.6
3.42	0.34	0.82	23.4
3.12	0.33	0.80	23.2
2.72	0.33	0.76	22.8
2.42	0.33	0.71	22.4
2.12	0.33	0.63	21.8
1.82	0.33	0.56	21.0
1.52	0.33	0.48	20.0
1.22	0.33	0.38	18.8
1.02	0.33	0.33	18.0
0.82	0.33	0.25	16.8
0.62	0.33	0.23	15.2
0.42	0.33	0.19	13.6
0.22	0.33	0.14	10.0
0.02	0.33	0.12	6.0

X = 9.75"
(Continued)

Y (Inches)	C_p	$\frac{U}{V_1}$	α (Degrees)
-0.08	0.33	0.10	2.2
-0.18	0.33	0.092	156.0
-0.38	0.33	0.098	163.0
-0.78	0.33	0.108	169.0
-1.18	0.33	0.107	172.0
-1.58	0.33	0.111	176.0
-2.08	0.33	0.109	176.0
-2.58	0.33	0.105	177.0
-3.08	0.33	0.094	180.0
-3.58	0.33	0.089	183.0
-4.08	0.33	0.070	186.0
-4.58	0.33	0.056	195.0
-5.08	0.33	0.042	189.0
-5.58	0.33	0.030	179.0

Table 3
Pressure recovery coefficients and velocities inside TKD flow field

X = -4.25"

Y (Inches)	C_p	$\frac{U}{V_1}$	α (Degrees)
0.93	-0.02	1.01	0.6
0.53	-0.01	1.08	0.4
0.13	-0.01	1.11	0.2
-0.27	0.00	1.11	0.0
-0.47	0.00	1.10	0.0
-0.67	0.00	1.07	0.0
-0.87	0.00	1.03	0.0

X = -2.25"

Y (Inches)	C_p	$\frac{U}{V_1}$	α (Degrees)
1.13	-0.09	0.98	1.0
0.73	-0.06	1.07	1.4
0.33	-0.04	1.11	1.2
-0.07	-0.02	1.12	1.0
-0.47	0.00	1.09	0.5
-0.67	0.00	1.06	0.2
-0.87	0.01	1.01	0.0

X = -1.25"

Y (Inches)	C_p	$\frac{U}{V_1}$	α (Degrees)
0.93	-0.14	1.06	2.2
0.73	-0.12	1.10	2.2
0.33	-0.08	1.13	2.4
-0.07	-0.03	1.12	2.2
-0.47	0.01	1.08	1.8
-0.87	0.03	0.99	0.8
-1.07	0.04	0.93	0.6
-1.27	0.04	0.88	0.4

Y (Inches)	C_p	$\frac{U}{V_1}$	α (Degrees)
0.73	-0.16	1.13	5.0
0.53	-0.14	1.14	5.2
0.33	-0.10	1.15	5.4
-0.07	-0.02	1.12	5.4
-0.47	0.05	1.05	4.2
-0.67	0.13	0.93	3.2
-1.07	0.15	0.85	2.0
-1.17	0.16	0.83	2.0

Table 3 (Continued)
Pressure recovery coefficients and velocities inside TKD flow field

X = 0.75"				X = 1.75"			
Y (Inches)	C_p	$\frac{U}{V_1}$	α (Degrees)	Y (Inches)	C_p	$\frac{U}{V_1}$	α (Degrees)
1.33	-0.24	1.07	18.4	1.73	-0.09	0.92	24.0
1.13	-0.21	1.10	16.4	1.53	-0.07	1.00	21.2
0.73	-0.14	1.14	14.6	1.13	-0.03	1.08	18.6
0.33	-0.01	1.11	11.4	0.73	0.01	1.10	16.6
-0.07	0.04	1.07	9.8	0.33	0.05	1.08	15.2
-0.47	0.10	1.00	8.2	-0.07	0.11	1.03	13.8
-0.67	0.14	0.94	7.2	-0.27	0.13	0.98	12.7
-0.87	0.16	0.88	6.4	-0.47	0.15	0.93	12.0
-1.07	0.20	0.79	4.8	-0.67	0.18	0.87	11.0
-1.27	0.20	0.68	3.4	-0.87	0.20	0.78	9.6
-1.47	0.20	0.47	2.0	-1.07	0.21	0.67	7.2
-1.57	0.19	0.25	-2.0	-1.27	0.21	0.47	5.0
-1.67	0.19	0.12	165.0	-1.47	0.20	0.24	2.0
-1.70	0.19	0.08	166.0	-1.57	0.19	0.13	-4.0
				-1.67	0.19	0.07	153.0
				-1.77	0.19	0.08	163.0
				-1.97	0.20	0.08	160.0
				-2.17	0.20	0.08	155.0

Table 3 (Continued)
Pressure recovery coefficients and velocities inside TKD flow field

X = 2.75"				X = 3.75"			
Y (Inches)	C_p	$\frac{U}{V_1}$	α (Degrees)	Y (Inches)	C_p	$\frac{U}{V_1}$	α (Degrees)
2.13	0.02	0.82	25.0	2.53	0.09	0.76	25.0
1.93	0.03	0.93	24.7	2.13	0.10	0.95	24.5
1.53	0.05	1.02	21.6	1.73	0.12	1.02	22.7
1.13	0.08	1.06	20.0	1.33	0.14	1.04	21.6
0.73	0.10	1.05	18.8	0.93	0.15	1.03	20.6
0.33	0.13	1.02	18.0	0.53	0.17	0.98	19.6
0.13	0.15	0.99	17.2	0.13	0.19	0.90	18.4
-0.07	0.16	0.95	16.6	-0.07	0.20	0.83	17.8
-0.27	0.18	0.89	16.0	-0.27	0.20	0.75	17.0
-0.47	0.20	0.82	15.2	-0.47	0.20	0.64	16.0
-0.67	0.20	0.72	13.6	-0.67	0.21	0.51	14.4
-0.87	0.20	0.60	11.0	-0.87	0.21	0.37	12.4
-1.07	0.21	0.44	7.0	-1.07	0.20	0.35	7.0
-1.27	0.20	0.26	2.6	-1.27	0.20	0.13	3.2
-1.37	0.20	0.18	-1.6	-1.37	0.20	0.09	-5.0
-1.47	0.20	0.11	-7.0	-1.47	0.20	0.074	150.0
-1.57	0.20	0.079	149.0	-1.87	0.20	0.084	167.0
-1.87	0.20	0.084	163.0	-2.27	0.20	0.078	163.0
-2.27	0.20	0.078	158.0	-2.67	0.20	0.076	160.0
-2.61	0.20	0.076	152.0	-3.07	0.20	0.069	153.0

Table 3 (Continued)
Pressure recovery coefficients and velocities inside TKD flow field

X = 4.75"				X = 5.75"			
Y (Inches)	C_p	$\frac{U}{V_1}$	α (Degrees)	Y (Inches)	C_p	$\frac{U}{V_1}$	α (Degrees)
2.93	0.14	0.86	25.0	3.33	0.16	0.78	25.0
2.53	0.15	0.93	25.0	2.93	0.17	0.93	25.0
2.13	0.16	1.02	22.8	2.13	0.19	1.01	23.6
1.33	0.18	1.01	22.0	1.73	0.19	1.00	23.1
0.93	0.19	0.97	21.2	1.33	0.19	0.96	22.4
0.53	0.19	0.88	20.2	0.93	0.19	0.87	21.4
0.33	0.19	0.82	19.6	0.53	0.20	0.72	20.0
0.13	0.20	0.74	19.0	0.33	0.20	0.64	19.2
-0.07	0.20	0.64	18.4	0.13	0.20	0.54	18.0
-0.27	0.20	0.53	17.6	-0.07	0.20	0.44	16.6
-0.47	0.20	0.42	16.6	-0.27	0.20	0.36	15.0
-0.67	0.20	0.31	15.2	-0.47	0.20	0.26	13.0
-0.87	0.20	0.21	11.4	-0.67	0.20	0.17	10.0
-1.17	0.20	0.08	2.0	-0.87	0.20	0.10	5.0
-1.27	0.20	0.072	154.0	-0.97	0.20	0.08	0.2
-1.47	0.20	0.076	166.0	-1.07	0.20	0.072	156.0
-1.87	0.20	0.084	171.0	-1.47	0.20	0.080	172.0
-2.27	0.20	0.076	169.0	-1.87	0.20	0.079	173.0
-2.67	0.20	0.069	167.0	-2.27	0.20	0.076	172.0
-3.07	0.20	0.065	163.0	-3.07	0.20	0.062	169.0
-3.37	0.20	0.061	158.0	-3.47	0.20	0.053	165.0
				-3.87	0.20	0.047	158.0

Table 3 (Continued)
Pressure recovery coefficients and velocities inside TKD flow field

X = 7.75"

Y (Inches)	C_p	$\frac{U}{V_1}$	α (Degrees)
4.80	0.19	0.54	25.0
4.50	0.19	0.66	25.0
4.20	0.19	0.79	25.0
3.90	0.20	0.89	25.0
3.60	0.20	0.97	25.0
3.30	0.20	1.00	24.6
2.70	0.20	0.99	24.0
2.40	0.20	0.96	23.6
2.10	0.20	0.91	23.0
1.80	0.20	0.82	22.0
1.50	0.20	0.74	20.8
1.20	0.20	0.63	19.4
0.90	0.20	0.52	18.0
0.60	0.20	0.40	16.2
0.30	0.20	0.29	14.0
0.00	0.20	0.18	10.0
-0.20	0.20	0.12	6.0
-0.40	0.20	0.08	1.0
-0.50	0.20	0.073	154.0
-0.80	0.20	0.077	170.0

X = 7.75"
(Continued)

Y (Inches)	C_p	$\frac{U}{V_1}$	α (Degrees)
-1.40	0.20	0.088	176.0
-2.20	0.20	0.077	176.0
-3.00	0.20	0.063	178.0
-3.60	0.20	0.045	180.0
-4.20	0.20	0.028	182.0
-4.80	0.20	0.028	170.0

Table 3 (Continued)
Pressure recovery coefficients and velocities inside TKD flow field

X = 9.75"

Y (Inches)	C_p	$\frac{U}{V_1}$	α (Degrees)
5.50	0.20	0.64	25.0
5.20	0.20	0.75	25.0
4.90	0.20	0.86	25.0
4.60	0.20	0.94	25.0
4.30	0.20	0.98	25.0
3.70	0.20	0.99	24.2
3.40	0.20	0.95	23.8
3.10	0.20	0.90	23.5
2.80	0.20	0.83	22.8
2.40	0.20	0.72	21.8
2.10	0.20	0.62	20.7
1.80	0.20	0.52	19.4
1.50	0.20	0.43	18.0
1.20	0.20	0.33	16.4
0.90	0.20	0.24	14.6
0.60	0.20	0.15	12.4
0.40	0.20	0.11	8.6
0.20	0.20	0.08	4.0
0.10	0.20	0.072	163.0
-0.50	0.20	0.084	175.0

X = 9.75"
(Continued)

Y (Inches)	C_p	$\frac{U}{V_1}$	α (Degrees)
-0.90	0.20	0.089	178.0
-1.70	0.20	0.088	178.0
-2.50	0.20	0.079	179.0
-3.30	0.20	0.065	181.0
-3.70	0.20	0.057	184.0
-4.10	0.20	0.052	187.0
-4.50	0.20	0.036	193.0
-4.90	0.20	0.028	193.0
-5.30	0.20	0.017	201.0
-5.70	0.20	0.017	29.0

Table 3 (Continued)
Pressure recovery coefficients and velocities inside TKD flow field

X = 11.75"

Y (Inches)	C_p	$\frac{U}{V_1}$	α (Degrees)
6.40	0.20	0.66	25.0
6.00	0.20	0.78	25.0
5.60	0.20	0.90	25.0
5.20	0.20	0.97	24.8
4.80	0.20	0.98	24.4
4.40	0.20	0.94	23.8
4.00	0.20	0.87	23.2
3.60	0.20	0.77	22.4
3.20	0.20	0.67	21.4
2.80	0.20	0.55	20.2
2.40	0.20	0.43	19.0
2.00	0.20	0.32	17.4
1.60	0.20	0.22	15.2
1.20	0.20	0.14	11.4
1.00	0.20	0.10	8.4
0.80	0.20	0.07	3.0
0.70	0.20	0.067	154.0
0.40	0.20	0.077	166.0
0.00	0.20	0.085	175.0
-0.40	0.20	0.093	178.0

X = 11.75"
(Continued)

Y (Inches)	C_p	$\frac{U}{V_1}$	α (Degrees)
-1.20	0.20	0.095	178.0
-2.10	0.20	0.089	178.0
-3.10	0.20	0.079	180.0
-4.10	0.20	0.061	183.0
-5.10	0.20	0.036	193.0
-5.60	0.20	0.029	209.0
-6.10	0.20	0.020	19.0
-6.60	0.20	0.029	-23.0

Table 4a
Boundary Layer parameters for REF flow field

S (Inch)	X (Inch)	Unstalled Wall δ* (Inch)	Unstalled Wall θ (Inch)	Unstalled Wall H	Stalled Wall δ* (Inch)	Stalled Wall θ (Inch)	Stalled Wall H
-6.00	-6.00	0.040	0.030	1.33	0.039	0.030	1.33
-5.00	-5.00	0.042	0.032	1.33	0.041	0.031	1.32
-4.00	-4.00	0.046	0.033	1.36	0.045	0.033	1.35
-2.50	-2.50	0.048	0.035	1.38	0.049	0.035	1.39
-1.50	-1.50	0.043	0.033	1.31	0.053	0.038	1.39
-0.50	-0.50	0.043	0.033	1.31	0.066	0.047	1.40
0.55	0.50	0.079	0.044	1.80	0.460	0.078	5.90
1.66	1.50	0.145	0.072	2.01			
3.00	2.72	0.182	0.101	1.80	Separation point is at		
4.00	3.62	0.205	0.114	1.80	X ≈ 0.0"		
5.00	4.53	0.218	0.125	1.74			
6.00	5.44	0.218	0.133	1.67			
8.00	7.25	0.221	0.148	1.49			
10.00	9.06	0.217	0.155	1.40			
12.00	10.89	0.215	0.156	1.38			
14.00	12.69	0.210	0.161	1.30			
16.00	14.50	0.205	0.158	1.29			
18.00	16.31	0.200	0.156	1.28			

Uncertainty is about 4% for all values

Table 4b
Boundary layer parameters for RC8 flow field

S (Inch)	X (Inch)	Unstalled Wall δ* (Inch)	Unstalled Wall θ (Inch)	Unstalled Wall H	Stalled Wall δ* (Inch)	Stalled Wall θ (Inch)	Stalled Wall H
-6.02	-6.0	0.040	0.030	1.33	0.039	0.030	1.30
-5.01	-5.0	0.041	0.031	1.33	0.042	0.032	1.31
-4.02	-4.0	0.043	0.032	1.34	0.045	0.035	1.29
-2.52	-2.5	0.045	0.034	1.31	0.048	0.037	1.30
-1.52	-1.5	0.043	0.033	1.30	0.052	0.040	1.30
-0.52	-0.5	0.042	0.032	1.31	0.118	0.066	1.79
0.52	0.5	0.058	0.043	1.35	0.365	0.092	3.96
1.52	1.5	0.077	0.052	1.48			
2.93	2.72	0.136	0.074	1.84			
3.93	3.62	0.158	0.082	1.93			
4.93	4.53	0.173	0.087	1.99			
5.93	5.44	0.185	0.097	1.91			
7.93	7.25	0.204	0.115	1.78			
9.93	9.06	0.200	0.115	1.73			
11.93	10.89	0.194	0.116	1.67			
13.93	12.69	0.186	0.120	1.55			
15.93	14.50	0.187	0.122	1.53			

Separation point is at X ≈ 0.25"

Uncertainty is about 4% for all values

Table 4c
Boundary layer parameters for TKD flow field

Unstalled Wall					Stalled Wall		
S (Inch)	X (Inch)	δ^* (Inch)	θ (Inch)	H	δ^* (Inch)	θ (Inch)	H
-6.00	-6.00	0.155	0.118	1.32	0.145	0.110	1.32
-4.00	-4.00	0.148	0.113	1.31	0.146	0.111	1.32
-2.50	-2.50	0.138	0.106	1.30	0.150	0.113	1.32
-1.50	-1.50	0.120	0.094	1.27	0.163	0.122	1.33
-0.50	-0.50				0.189	0.138	1.36
0.55	0.50	0.131	0.083	1.58	0.575	0.195	2.95
1.66	1.50	0.265	0.149	1.78			
3.00	2.72	0.361	0.187	1.93	Separation point is at		
4.00	3.62	0.378	0.204	1.86	X ≈ 0.25"		
5.00	4.53	0.384	0.213	1.80			
6.00	5.44	0.403	0.228	1.77			
8.00	7.25	0.401	0.236	1.70			
10.00	9.06	0.396	0.244	1.62			
12.00	10.89	0.390	0.248	1.57			

Uncertainty is about 4% for all values

APPENDIX A

CORRECTION OF FLOW DIRECTION DUE TO LOCAL VELOCITY GRADIENT

To measure the flow direction at a point in the flow field, a wedge-shaped, three-hole probe was rotated until the two side holes sensed equal pressure. Then the orientation of the probe was taken as the local flow direction. However, if the local velocity profile is non-uniform in the viscinity of the probe, the flow direction measured by this method needs correction.

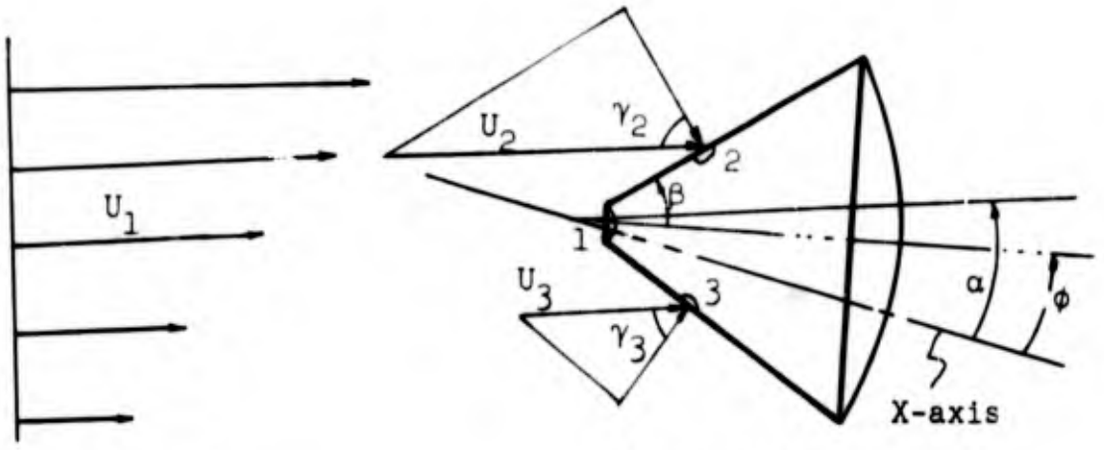

Non-uniform velocity profile

Three hole probe

ϕ = direction measured by nulling pressure sensed by hole 2 and hole 3

α = actual flow direction

X-axis = center line of flow channel

β = half angle of the three-hole probe, 30°

U_1, U_2, U_3 = velocities that would be sensed by holes 1, 2 and 3 respectively if flow were not deflected by the probe

γ_2, γ_3 = angles between normals of probe surface and U_2 , U_3 respectively

The sketch above shows the situation where local velocity profile is not uniform. ϕ is the orientation of the probe when pressure at hole 2 equals pressure at hole 3. Assuming that the pressure sensed by the side hole is related to the square of velocity component normal to the probe surface, the following equation is obtained.

$$v_2^2 \cos^2 \gamma_2 = U_3^2 \cos^2 \gamma_3 \qquad \text{(A-1)}$$

From geometry

$$\gamma_2 = (\tfrac{\pi}{2} - \beta) - (\phi - \alpha)$$

$$\gamma_3 = (\tfrac{\pi}{2} - \beta) + (\rho - \alpha)$$

Hence, Eq. (A-1) can be written as

$$\frac{U_2}{U_3} = \frac{\cos\,[(\frac{\pi}{2} - \beta) + (\phi - \alpha)]}{\cos\,[(\frac{\pi}{2} - \beta) - (\phi - \alpha)]} \qquad \text{(A-2)}$$

which is a transcendental equation with one unknown α, when U_1, U_2, and ϕ are obtained by measurement. This equation was used to calculate the actual flow direction at locations where velocity gradient is large, (e.g., in the free shear layer). The difference between corrected and original values can be as high as 6 degrees.

Actually the assumption used to derive Eq. (A-1) is physically incorrect because with the existence of the probe, local streamlines are deflected. As a matter of fact, the pressure sensed by hole 2 is nearly the local static pressure hence is not proportional to the square of the normal velocity component. However, results obtained by this correction method check quite well with the slope of the streamlines and are thus adopted as actual values.

APPENDIX B
PRESSURE DISTRIBUTION ON STALLED WALL BEYOND THE SEPARATION POINT

In fig. III-3, the pressure recovery coefficient appears to be constant beyond X = 1/2" on the stalled wall, but if the scale is magnified, one can see slight variation in its values in the stalled region. Fig. B-1 shows the distribution of pressure recovery coefficient along the stalled wall beyond the separation point for the REF flow field. The values are presented as differences from the room pressure on a greatly magnified scale.

In this scale for C_p, which is fifty times that in fig. III-3, variation of pressure recovery coefficient is clearly observable in the reverse flow region but nearly constant in the section where a second vortex appears (see fig. III-5).

Relatively speaking, the velocity in the second vortex is small compared to the reverse flow velocity; hence variation in pressure in this region should also be small compared to that in the reverse flow. By the same token, variation of C_p in the reverse flow region will be small when it is compared to the magnitudes in the main flow. Hence, the conclusion that C_p is essentially constant in the stalled flow region should not be taken in an absolute sense, but rather as a statement of the relative magnitude of flow quantities between the main and the stalled flow region.

Since the uncertainty in C_p measurement is about 0.01, all the values in this figure B-1 is within a range less than the uncertainty value. Hence it may not be reproducible in another experimental set-up. For the present investigation, however, similar trends are also observed for both the RC8 and the TKD flow fields.

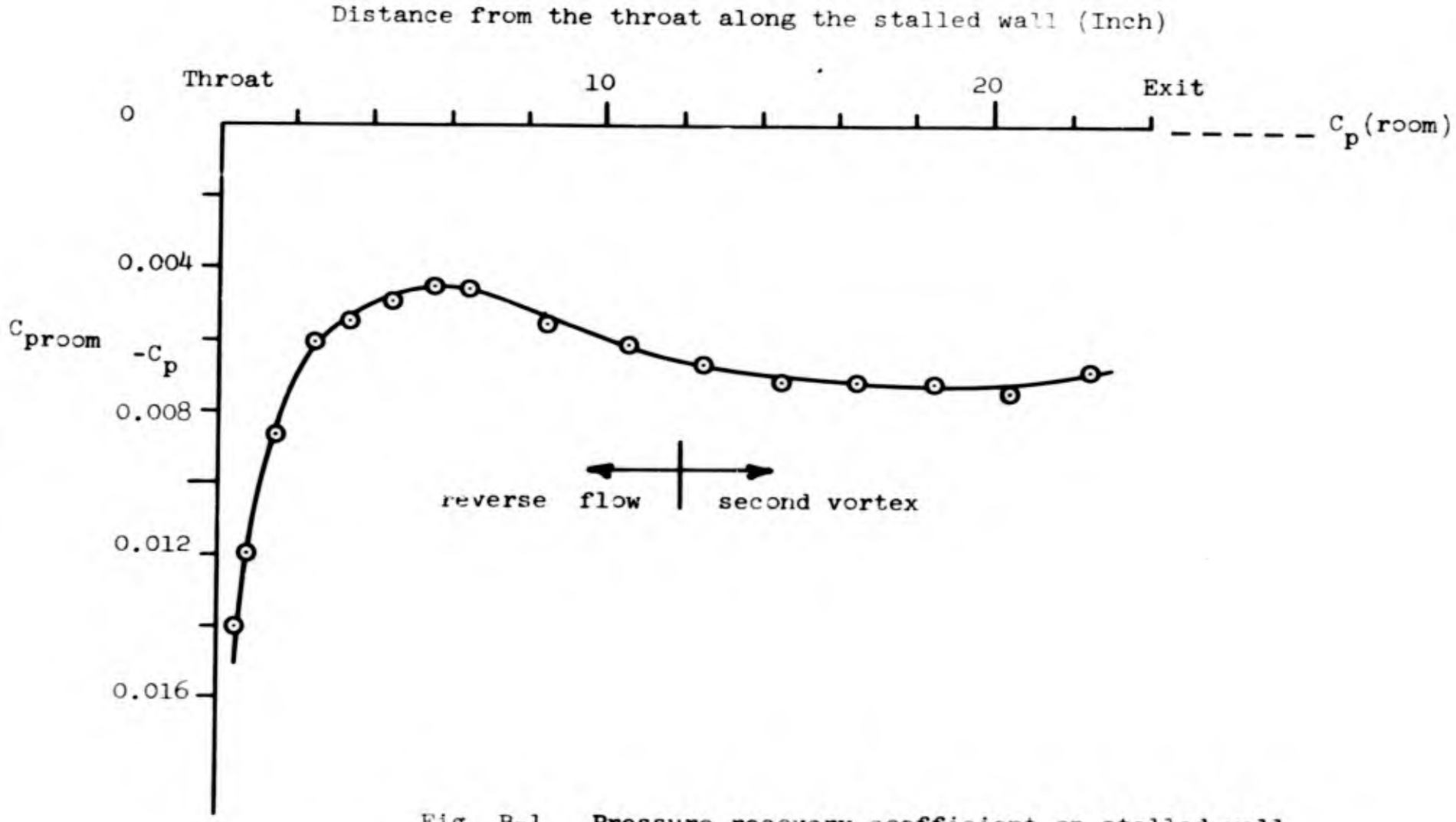

Fig. B-1 **Pressure recovery coefficient on stalled wall beyond the separation point for REF flow field**

APPENDIX C

MORE PRELIMINARY RESULTS ON TURBULENT MIXING

Before the results for turbulent mixing in Chapter IV were obtained some preliminary checks on the effects of mixing on final pressure recovery coefficient were made. Results can be summarized in the following table.

Case	Stalled Wall at Inlet		Unstalled Wall at Inlet		V_1 (fps)	C_{pe}	Separation Point X" from throat
	δ^* (Inch)	H	δ^* (Inch)	H			
†REF	0.039	1.33	0.040	1.33	157	0.22	0.00
‡REF with VG at X = -12"	0.019	1.38	0.019	1.38	166	0.23	0.25
†REF with thin wedge at X = -15"	0.106	1.25	0.112	1.27	159	0.25	0.50
REF with thick wedge at X = -15"	0.230	1.32	0.180	1.37	146	0.28	1.00‡
†RC8	0.039	1.30	0.040	1.33	160	0.34	0.25
RC8 with thick wedge at X = -15"	0.230	1.32	0.180	1.37	152	0.41	1.50‡
†TKD	0.145	1.32	0.155	1.32	157	0.20	0.25
TKD with VG at X = -11"	0.075	1.21	0.091	1.26	170	0.21	0.25‡

Note: VG = vortex generators shown in fig. IV-24
Arrangement of wedge attachment is shown on page 43
Thin wedge: a = 0.125" b = 0.75"
Thick wedge: a = 0.22" b = 1.00"

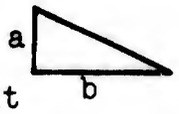

† These results have been presented in the main text

‡ These points are located by observation of tuft movements only. Uncertainty may be ± 0.5"

These results clearly indicate that turbulent mixing is an important factor that can move the separation point and thus widen the effective channel and increase the pressure recovery.

Attempts were made to correlate final pressure recovery coefficients with δ^*, θ, or H at the inlet but no meaningful correlations could be obtained. It is suspected that these final recovery values would be related to the inlet turbulent scale.

APPENDIX D

EQUATIONS FOR BOUNDARY LAYER CALCULATION MODELS†

Model VD&T

This is the method of Von Doenhoff and Tetervin [1943]. Unknowns to be calculated are θ, H and C_f, all of which are functions of the streamwise variable x. The following equations are used.

1. Von Karman's momentum equation

$$\frac{d\theta}{dx} = \frac{C_f}{2} - (H + 2)\frac{\theta}{U_\infty}\frac{dU_\infty}{dx} \qquad \text{(D-1)}$$

2. Empirical auxilliary equation

$$\theta \frac{dH}{dx} = e^{4.68(H - 2.975)}\left[-\frac{\theta}{q}\frac{dq}{dx}\frac{2}{C_f} - 2.035(H - 1.286)\right] \qquad \text{(D-2)}$$

3. Squire and Young friction relation

$$\frac{2}{C_f} = [5.89 \log_{10}(4.075\ Re_\theta)]^2 \qquad \text{(D-3)}$$

$$\text{where} \quad Re_\theta = \frac{\rho U_\infty \theta}{\mu}$$

Model M1N4

Dependent variables in this method are u_τ, δ and ω from which δ^*, θ and H can be evaluated with the aid of the velocity profile represented by Eq. (D-6) below. The three independent equations for this model are:

---

† The author wants to thank Mr. E. Hirst for compiling the equations for this section.

1. Equation (D-1)

2. Energy integral equation

$$\theta \frac{dH}{dx} = - H(H-1)(3H-1) \frac{\theta}{U_\infty} \frac{dU_\infty}{dx} + (3H-1) \left[H \frac{C_f}{2} \right.$$

$$\left. - \frac{(3H-1)}{2} \times \frac{1}{\rho U_\infty^3} \int_0^\delta \frac{\partial u}{\partial y} \tau \, dy \right] \qquad \text{(D-4)}$$

where τ is evaluated by

$$\tau = \epsilon \frac{\partial u}{\partial y} \qquad \epsilon = 0.018 \, \delta^* \, U_\infty \qquad \text{(D-5)}$$

3. Asymptotic matching of the following two laws for u_τ and velocity profile

(a) Law of the wall

$$u^+ = \frac{1}{K} \ell n \, y^+ + C \qquad \text{where} \quad K = 0.4, \; C = 5.06$$

(b) Law of the wake

$$\frac{U_\infty - u}{u_\tau} = \frac{1}{K} \ell n \frac{y}{\delta} + \frac{\omega}{K} \left[\cos\left(\frac{\pi y}{\delta}\right) + 1 \right]$$

where $K = 0.4$

(D-6)

Model M1N6

This method is similar to Model M1N4 except that instead of Eq. (D-5), Truckenbrodt's dissipation function is used for the last term in Eq. (D-4). Hence, the independent unknowns are u_τ, δ and ω; and the equations for calculating them are as follows.

1. Equation (D-1)

2. Equation (D-4) with Truckerbrodt's dissipation integral (see pp. 575, Schlichting [1960])

$$\frac{1}{\rho U_\infty^3}\int_0^\delta \frac{\partial u}{\partial y}\,\tau\,dy = \frac{0.0056}{Re_\theta^{1/6}} \qquad \text{(D-7)}$$

3. Equation (D-6)

Model M2N1

Independent unknowns to be evaluated in this method are u_τ, δ, ω, and g. The following four equations are used.

1. Equation (D-1)

2. Equation (D-6)

3. Entrainment equation

$$\frac{d}{dx}\int_0^\delta u\,dy = K\,g \qquad \text{(D-8)}$$

4. Turbulent kinetic energy model equation

$$\frac{d}{dx}\left[\frac{g^2}{2}\int_0^\delta u\,dy\right] = 0.14\,u_\tau g^2 \qquad \text{(D-9)}$$

where $g^2 = \frac{1}{\delta}\int_0^\delta (u'^2 + v'^2 + w'^2)\,dy$

u', v' and w' are rms turbulent velocity fluctuations in longitudinal, normal and transverse direction, respectively.

APPENDIX E

RECOMMENDATIONS FOR FURTHER WORK

1. Perform additional experiments with different radius of curvature at the throat to find correlation of final pressure recovery coefficient with geometry at the throat. Recommended sequence is 20", 12" and 4". If C_p distribution along the side walls changes appreciably, complete mapping of flow field data would be useful.

2. Change exit geometry to include long and short tailpipes and map out data in the flow fields to find out what happens when the main flow rediffuses to fill the tailpipe. Investigate the phenomenon of reattachment when the tailpipe is long enough.

3. Decrease the divergence angle and map for at least one set of flow field data in the same flow regime to find out whether the conclusions in the present investigation hold.

4. Increase the divergence angle to the jet flow region (see fig. I-2) and find the effective channel in that flow configuration to check if the basis for the analytical model proposed in Chapter V holds.

5. Perform turbulent scale measurements at the inlet with systematic change of mixing devices and map out flow fields to find out possible correlations.

6. Improve numerical solution to the Dirichlet problem. Investigate the possibility of combining analog computer with digital computer to yield quick and accurate distribution of pressure recovery coefficient as output once the boundary of the effective channel is traced on an oscilloscope that can send a signal as input to the analog computer.

7. Develop boundary layer calculation method that can work under abrupt pressure change and include the effect of normal pressure gradient.

8. Modify the analytical model of Chapter V to see if it can be simplified.

UNCLASSIFIED

Security Classification

DOCUMENT CONTROL DATA - R&D

(Security classification of title, body of abstract and indexing annotation must be entered when the overall report is classified)

1. ORIGINATING ACTIVITY (Corporate author)

Mechanical Engineering Department
Stanford University
Stanford, California 94305

2a. REPORT SECURITY CLASSIFICATION

Unclassified

2b. GROUP

3. REPORT TITLE

INVESTIGATION OF A TWO-DIMENSIONAL FULLY STALLED TURBULENT FLOW FIELD

4. DESCRIPTIVE NOTES (Type of report and inclusive dates)

5. AUTHOR(S) (Last name, first name, initial)

Chui, Granger and Kline, Stephen J.

6. REPORT DATE	7a. TOTAL NO. OF PAGES	7b. NO. OF REFS
August 1967	160	23

8a. CONTRACT OR GRANT NO.	9a. ORIGINATOR'S REPORT NUMBER(S)
AF 49(638)-1278	MD-19
b. PROJECT NO.	
c. 61445014	9b. OTHER REPORT NO(S) (Any other numbers that may be assigned this report)
d. 681307	AFOSR 67-2047

10. AVAILABILITY/LIMITATION NOTICES

11. SUPPLEMENTARY NOTES

TECH, OTHER

12. SPONSORING MILITARY ACTIVITY

AF Off. of Scientific Research(SREM)
1400 Wilson Blvd.
Arlington, Virginia 22209

13. ABSTRACT

The bistable, steady, turbulent separation phenomenon observed in a two-dimensional fully-stalled diffuser is studied. Detailed mean flow data including pressure, dissipation and velocity (both magnitude and direction) inside the flow field as well as development of boundary layers on both side walls are reported for cases with thin and thick boundary layers at inlet and with and without fairing curves at the throat.

For all cases, most important changes in flow data occur in a region within two inlet widths up and downstream of the throat. Pressure gradients in this region are so large that the boundary layer on the unstalled side changes shape abruptly while the layer on the stalled side separates in the viscinity of the throat.

Streamline patterns are obtained from the velocity distributions. The location of the dividing streamline is different for the different cases. Based on the dividing streamline, a displacement line is defined to extend the concept of displacement thickness to the free shear layer which is developed from the separated boundary layer. This displacement line together with the loci of boundary layer displacement thicknesses on the solid walls form an effective channel. The shape and area ratio of this effective channel explain the different trends of pressure distributions in the main flow.

DD FORM 1 JAN 64 1473

UNCLASSIFIED

Security Classification

14 KEY WORDS	LINK A		LINK B		LINK C	
	ROLE	WT	ROLE	WT	ROLE	WT
Separated flow						
Subsonic						
Bistable flow						
Experimental						
Wide-angle diffuser						